RF-Transport through Mesoscopic Hall Bar coupled to On-Chip Microwave Resonators

Paras Seth

université PARIS-SACLAY

RF-Transport through Mesoscopic Hall Bar coupled to On-Chip Microwave Resonators

Transport RF à travers une barre Hall mésoscopique couplée à des résonateurs micro-ondes sur puce

Thèse de doctorat de l'université Paris-Saclay

École doctorale n°564 Physique en Île-de-France (PIF)
Spécialité de doctorat: Physique
Graduate school: physique, Référent: Faculté des sciences d'Orsay

Thèse préparée dans l'unité de recherche **Service de Physique de l'État Condensé** (Université Paris-Saclay, CEA, CNRS), sous la direction de **Patrice ROCHE**, directeur de recherche, CEA Saclay, et le co-encadrement de **Carles ALTIMIRAS**, chargé de recherche, CEA Saclay

Thèse soutenue à Paris-Saclay, le 5 Mars 2024, par

Paras SETH

Composition du Jury

Membres du jury avec voix délibérative

Anne ANTHORE Professeur, Université Paris Saclay	Présidente
Fabian HASSLER Professeur, RWTH Aachen University	Rapporteur & Examinateur
Erwann BOCQUILLON Professeur, University of Cologne	Rapporteur & Examinateur
Benjamin PIOT Chargé de recherche, LNCMI, Université de Grenoble	Examinateur

Thèse de doctorat
NNT : 2024UPASP015

université PARIS-SACLAY | ÉCOLE DOCTORALE Physique en Île-de-France (PIF)

Titre: Transport RF à travers une barre Hall mésoscopique couplée à des résonateurs micro-ondes sur puce

Mots clés: transport mésoscopique, micro-ondes, effet Hall quantique, bruit de grenaille

Résumé: Dans cette thèse, nous rapportons des études expérimentales sur le transport radiofréquence dans un Hall Bar de taille mésoscopique en régime de Hall quantique. Le Hall Bar est un gaz d'électrons bidimensionnel formé dans une hétérostructure semiconductrice de GaAs/GaAlAs. La dynamique de ce Hall Bar est étudiée en modélisant des résonateurs sur puce qui y sont attachés et qui résonnent à 4,6 GHz. Ils fournissent une adaptation d'impédance avec Hall-Bar, nous permettant ainsi de sonder la physique en régime de réponse linéaire. Nous avons ainsi déterminé l'impédance du gaz électronique en régime de hall quantique. Le gaz électronique se comporte comme un transformateur d'impédance. Nous avons mesuré le bruit de tir à haute fréquence à travers l'appareil et déterminé les règles de composition d'impédance pour celui-ci dans diverses configurations de circuit. Enfin, nous avons tenté des expériences pour mesurer la rétro-action quantique de ces résonateurs sur le point de contact quantique à une fraction de remplissage de 2. Nous avons observé que ces effets ne sont pas canoniques comme dans les jonctions tunnel, mais sont affectés par la nature de la transformation d'impédance du gaz électronique.

Title: RF-Transport through mesoscopic Hall Bar coupled to microwave resonators

Keywords: mesoscopic transport, microwaves, Quantum Hall Effect, Shot noise

Abstract: In this thesis, we report experimental studies on radio frequency transport in mesoscopic size Hall Bar in quantum hall regime. The Hall Bar is a two-dimensional electron gas formed in semiconductor heterostructure of GaAs/GaAlAs. The dynamics of this Hall Bar are studied by patterning On-chip resonators attached to it which resonate at 4.6 GHz. They provide impedance matching with Hall-Bar, thereby, allowing us to probe the physics in linear response regime. With that we have determined the impedance of electron gas in quantum hall regime. Electron gas behaves as an impedance transformer.We have measured high-frequency shot noise through the device and determined the Impedance composition rules for it under various circuit setups. Lastly, we have attempted experiments to measure the quantum back-action of these resonators on the Quantum point contact at filling fraction of 2. We have observed that these effects are not canonical like in tunnel junctions, but are affected by impedance transformation nature of the electron gas.

Acknowledgements

I would like to thank my advisors Carles Altimiras and Patrice Roche for guiding me throughout my PhD journey. Especially, the discussions with Carles were quite intense but would always end up in getting a new way of approaching the solution to the problem. I learned a lot from him. Not only about my thesis subject, but pretty much any topic that we touched upon in discussions. Also, I would like to thank Yury Moukharsky, whom I would mention as my unofficial advisor. I learned all the small details of electronics (both low-frequency and high-frequency) and signal processing from him. Moreover, his "practical" way of approach to solutions to experimental measurements was always refreshing to witness. Sometimes, that was what we needed to proceed ahead.

I would like to thank Jury Members: Anne Anthore, Erwann Bocquillon, Fabian Hassler and Benjamin Piot for accepting to be the jury for my thesis defense.

I would also like to thank all my PhD, Post-docs, and other senior researchers in Nanoelectronics group and from other groups in SPEC. Over the years, we have developed a good bond of friendship among each other. You guys were essentially my "social club" here in Saclay. I have cherished all the talks with all of you.

And lastly, I would like to thank my family members for supporting me and believing in me all these years.

Contents

Chapter 1

Summary

In this thesis, dynamics of mesoscopic circuits in Quantum Hall regime have been studied. We have a mesoscopic size electron gas that is galvanically attached to on-chip microwave resonators. These resonators provide impedance matching and thus has allowed us to explore the physics of our device at high frequencies in linear response regime.

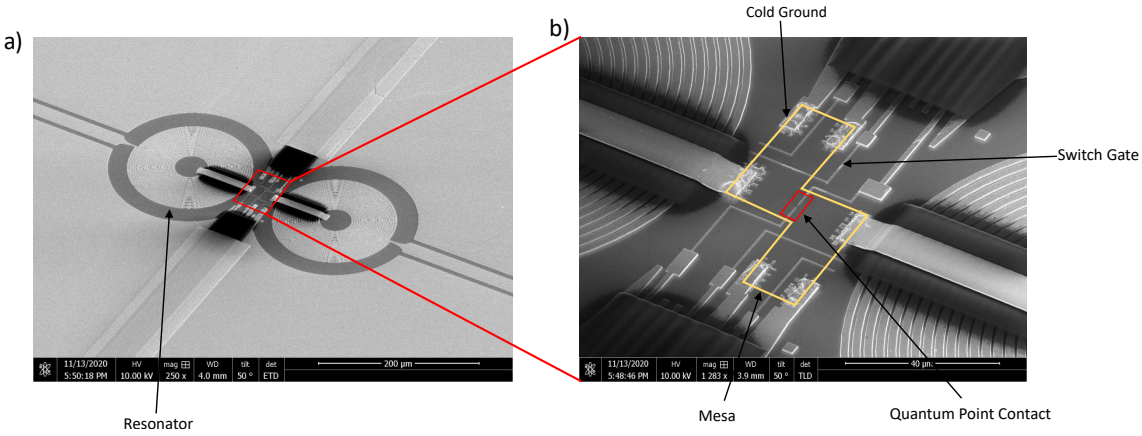

Figure 1.1: Electron micro-graph of the device. a) Zoom-out picture showing two resonators having two-dimensional electron gas in between. All around is a continuous metallic ground plane. b) Zoom-in picture in between resonators. The yellow polygon there marks the boundary of electron gas buried 100 nm below the surface. On top of it, at the centre, is the Quantum Point Contact (shown in red). There are also switch-gates, 2 on each side, allowing to have different circuit configurations. And there is an ohmic contact on opposite edges of mesa which connects it to metallic ground plane (termed as cold grounds).

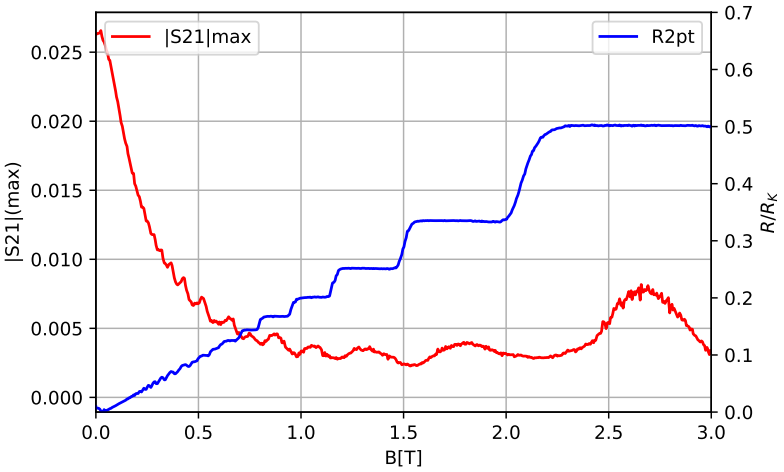

Figure 1.2: RF transmission (S21 max) (shown in red) along with two-probe resistance (in blue). There is a smooth variation of RF transmission with shubnikov-deHaas type oscillations as filling fraction is decreased with increase of the magnetic field

1.1 RF Transmission in Quantum Hall Regime

We have measured the high-frequency impedance of this mesoscopic circuit in the Quantum Hall Regime by measuring the RF transmission through the sample using vector network analyser. The observations have shown that in the range of 4-8 GHz frequencies, the chiral system (electron gas) behaves like an impedance transformer, with its specific rules dictated by the chirality due to Quantum Hall Effect. In particular, the transport through the edge states can be described as the one through a uni-directional transmission line. For magnetic fields where filling fraction is an integer ranging from 10 to 2, the collective excitations (Edge-magnetoplasmons) have linear dispersion relation and thus propagate with velocity which is linear with hall conductance. The current and voltage waves acquire a simple propagation phase when going through the device. When exploring within $\nu = 2$ plateau, we have explained the data by assuming an ohmic dissipation and then by assuming a RC coupling to the bulk localised states. When a scattering center like Quantum Point Contact is used, then things are slightly complicated, but basically by following the general scattering theory rules and incorporating the phase propagation of plas-

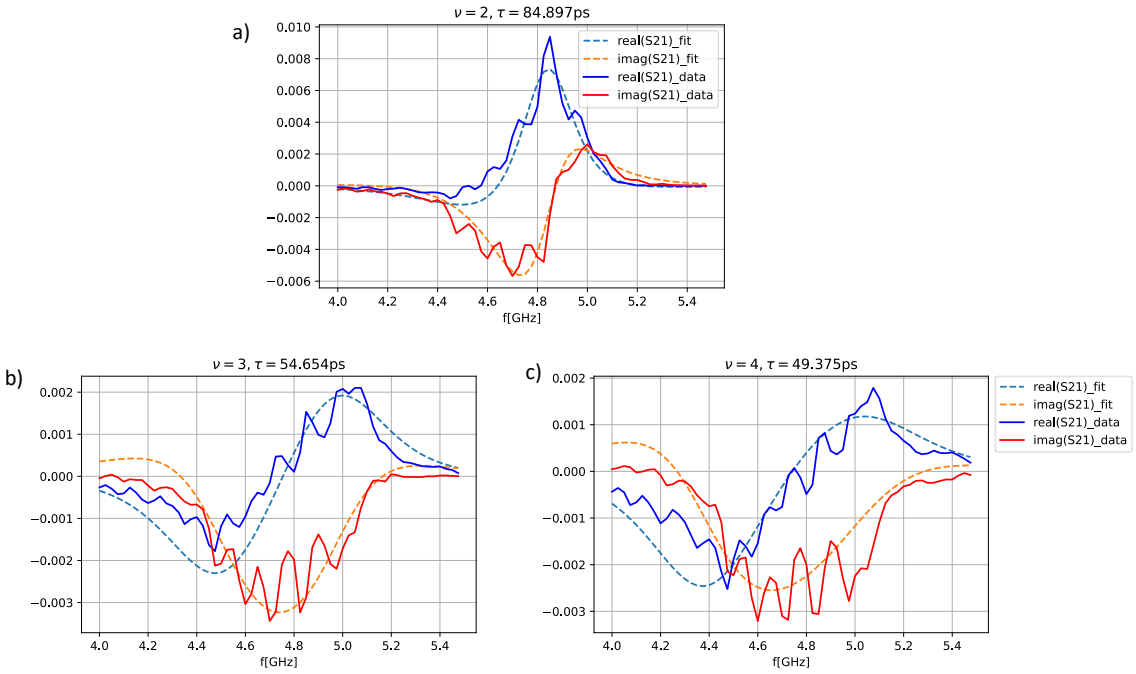

Figure 1.3: S21 curves for $\nu = 2, 3$ and 4 along with fits. The obtained τ are 84.9 ps, 54.65 ps and 49.375 ps respectively.

mons, it can be explained. From the zero field measurement, we have been able to characterize our resonators' internal resistance and determine the gain of the full RF chain in order to make the above mentioned claims quantitative.

1.2 Noise Measurements at $\nu = 2$ Plateau

We have then studied the high-frequency Shot noise emitted by DC biasing the Quantum Point Contact in different sample configurations. This has resulted in understanding the microwave coupling of the noise emitted from the QPC to detection chain. Thanks to the high-impedance nature of these on-chip resonators, the coupling is better than having just 50 ohm line, thereby, increasing S.N.R and reducing greatly the measurement time. Our findings show here that for 3-point setup configuration, the coupling of the noise is independent of the phase acquired by the noise signal when traversing from the QPC to the resonators. This is because there is no feedback of the current fluctuations that gets injected back to the system, due

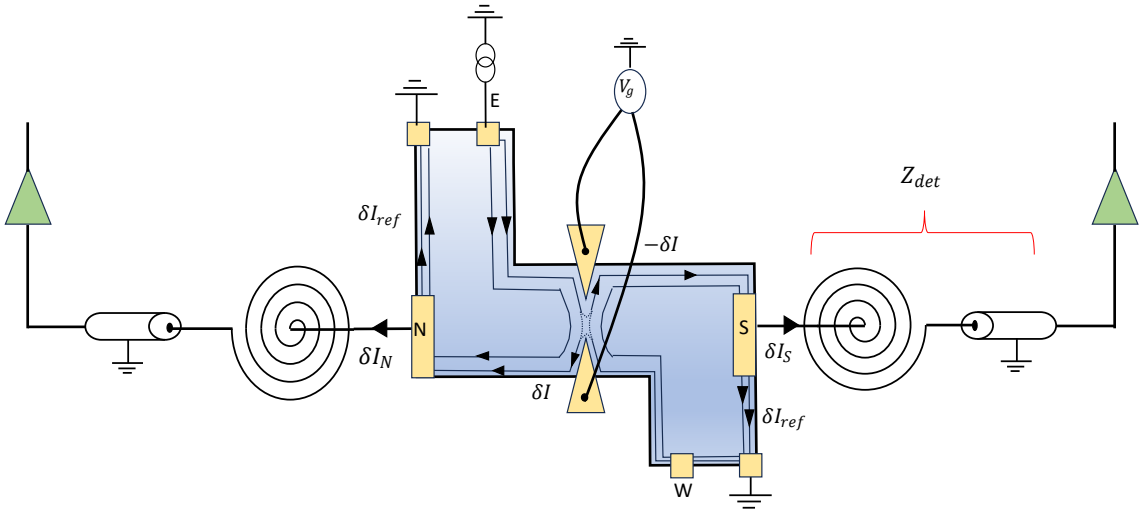

Figure 1.4: Circuit schematic for 3-point configuration. Inner-edge channel is fully reflected by the QPC while outer-edge is transmitted with probability τ. The Shot noise from the QPC gets injected into the outer edge channel on both sides of it which then reaches the resonator. The power received into the detection lines is proportional to δI_n and δI_s which are some fraction of δI, the bare Shot noise emitted from the QPC, owing to the current division.

to on-chip grounds. The detected power spectral density in 3-point setup for large DC bias ($eV >> hf_o$) is given as:

$$\frac{\delta P}{P_{off}} = \frac{1}{k_B T_N} \frac{(eV - hf)\tau(1-\tau)}{R_K} \frac{Re(Z_{det})}{|1 + 2G_K Z_{det}|^2} \tag{1.1}$$

This allows us to quantify RF gain of the detection chain. The noise temperature of the Cryo-Amplifiers as seen from the sample comes out to be 9.3K

In 2-point setup, however, there is no on-chip ground. This leads to classical feedback of the fluctuations onto the QPC, making the propagative phase an important quantity. The detected power spectral density in this configuration is given as:

$$\frac{\delta P}{P_{off}} = \frac{1}{k_B T_N} \frac{\langle \delta I^2_{bare} \rangle Re(Z_{det})}{|1 + (2 - (1-2\tau)e^{-i2\phi_o}) \frac{Z_{det}}{R_K}|^2} \tag{1.2}$$

By making basic fits with experimental data we have been able to extract the value of the acquired phase ϕ_o (see figure 1.7)

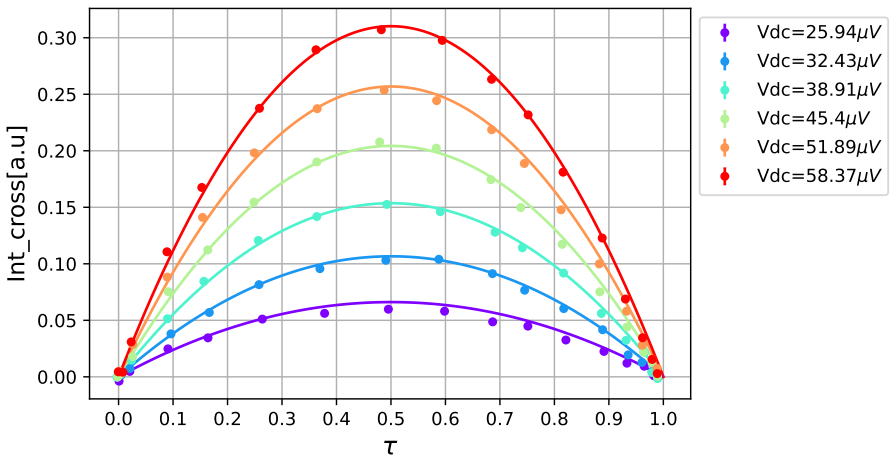

Figure 1.5: Transmission dependence of the Integrated noise power for outer -edge channel in 3-point setup. It follows canonical $\tau(1-\tau)$ dependence. The continuous lines is obtained by summing the formula 1.1 over frequency, where T_N is input as 9.3K

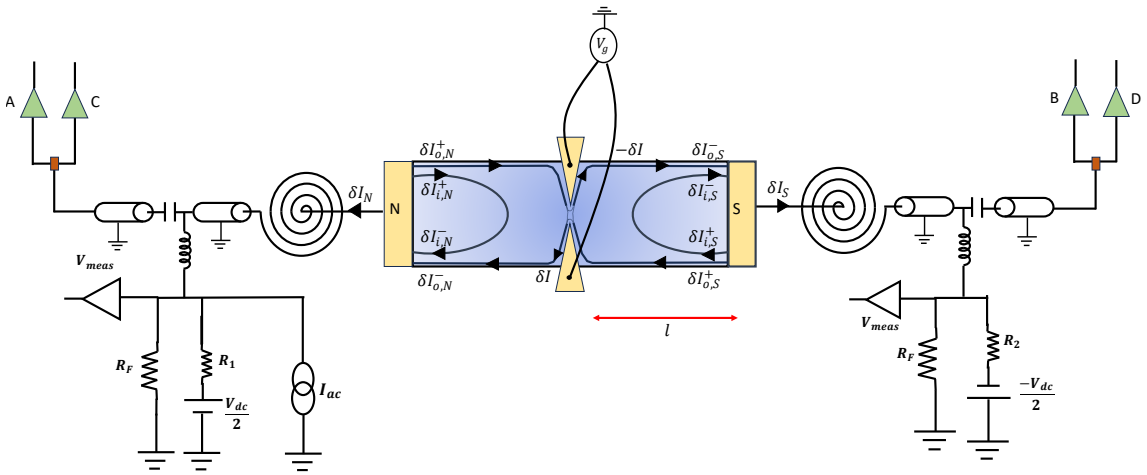

Figure 1.6: 2-point noise circuit: We do differential biasing across Quantum Point Contact. On the north side of the sample, a small current bias I_{ac} is applied via lock-in amplifier and voltage is measured. The resistors R_F to ground on each side are 12 kΩ. They help us to have a voltage bias. On RF side, we have two cryo-amps on each detection lines allowing us to measure the auto-correlation accurately. The splitting of emitted signal from sample into two lines is done by -3dB hybrid coupler (shown as brown square). Unfortunately, line C was disconnected during the run.

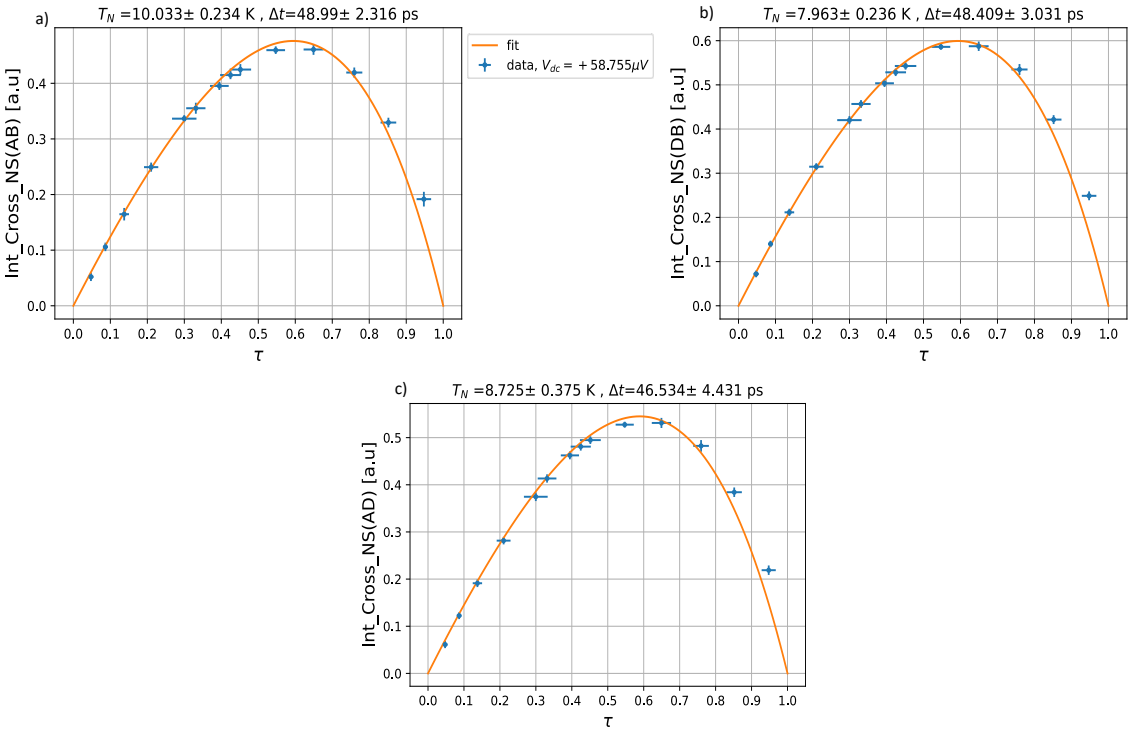

Figure 1.7: Integrated noise power along with fits with $V_{dc} = 58.7\mu V$ for three cross-correlations which are named here as 'AB', 'AD' and 'DB' respectively in 2-point setup.

1.3 Quantum-Back Action of Resonators

In a third set of experiments, we have explored the Quantum Back-action of the resonators onto the QPC, owing to the fact that feedback by zero-point fluctuations on QPC is always there, and that these fluctuations are sizeable due to the large characteristic impedance of the resonators. The observed reduction of differential conductance is a bit surprising. For one thing, the effects are seen at bias values which are equivalent to the energy quantum of the resonator and that these observed effects are not as strong as one would expect from the nature of the electromagnetic environment (value of characteristic impedance). We suspect that due to finite size of the electron gas between QPC and the resonators, there is an impedance transformation of the LC oscillator, thereby, changing the impedance nature of the environment. Currently, we do not have an understanding of this effect.

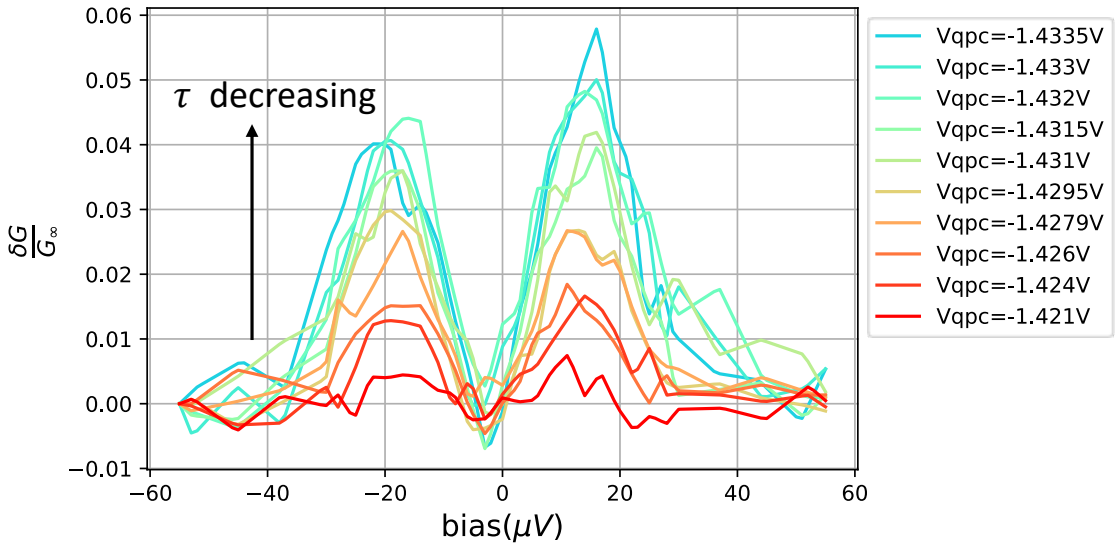

Figure 1.8: $\delta G/G_\infty$ plot as a function of bias applied. We see a reduction of the conductance at two bias values ($\pm 20\mu V$) ($20\mu V \sim hf_o$), symmetric about zero bias. The relative reduction with respect to large bias increases more with decreasing transmission.

1.4 Conclusion

In Conclusion, we can say that this mesoscopic circuit containing on-chip microwave resonators coupled to an electron gas in Quantum Hall regime is a good way to explore the dynamics of the electron gas, uncovering its high-frequency properties and also conveying information about how to compose the impedance of this chiral system with a circuit (resonator) having an impedance comparable to it. Also, with this knowledge, we could quantify the microwave coupling of the noise being emitted from quantum conductor to the detection circuit and study the quantum back-action of the resonators on quantum conductors. For these dynamical coulomb bockade effects, perhaps a smaller size of electron gas might be useful, since it will have less propagation effects, thus, weaker impedance transformation properties.

Chapter 2

Résumé en Français

Dans cette thèse, nous avons étudié la dynamique des circuits mésoscopiques en l'effet hall quantique. Nous disposons d'un gaz électronique de taille mésoscopique qui est connecté galvaniquement aux résonateurs micro-ondes défini on chip. Ces résonateurs une impedance de detection élevé et nous ont ainsi permis d'explorer la physique de notre dispositif à hautes fréquences en régime de réponse linéaire.

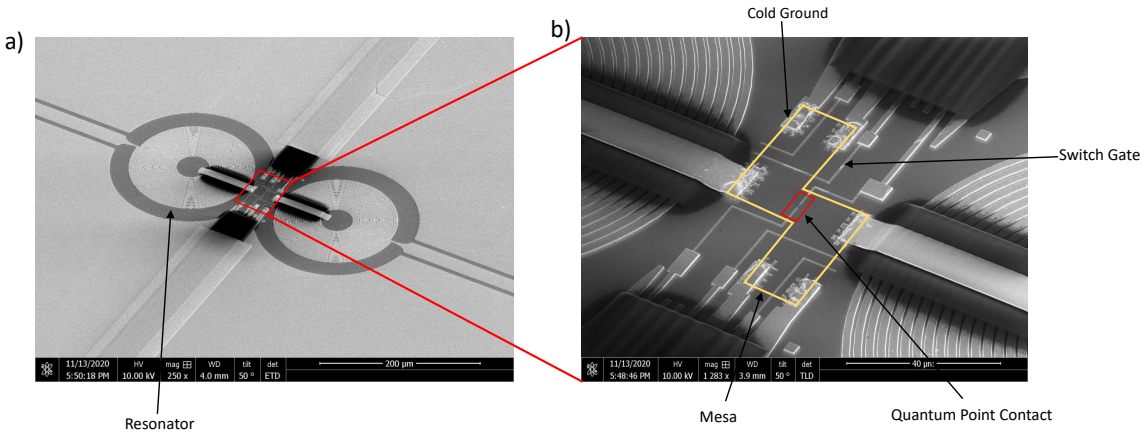

Figure 2.1: Micrographie électronique de l'appareil. a) Image zoom arrière montrant deux résonateurs ayant un gaz d'électrons bidimensionnel entre les deux. Tout autour se trouve un plan de masse métallique continu. b) Image zoomée entre les résonateurs. Le polygone jaune marque la limite du gaz électronique enfoui à 100 nm sous la surface. Au-dessus, au centre, se trouve le Quantum Point Contact (représenté en rouge). Il existe également des interrupteurs, 2 de chaque côté, permettant d'avoir différentes configurations de circuits. Et il y a un contact ohmique sur les bords opposés du mesa qui le relie au plan de masse métallique (appelé masse froide).

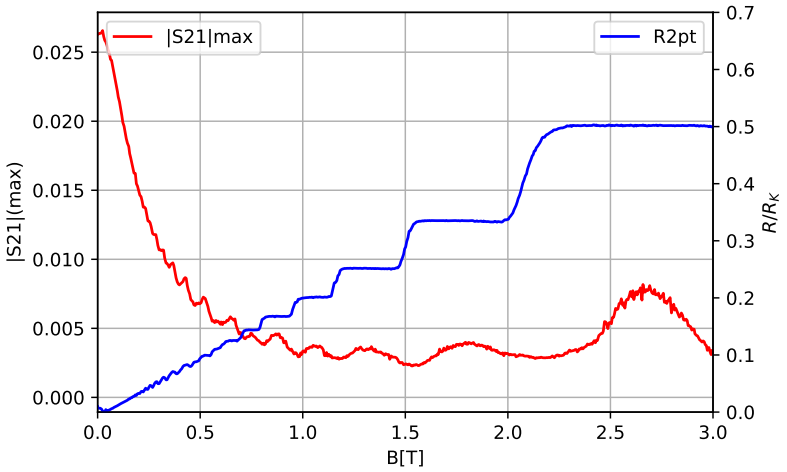

Figure 2.2: Transmission RF (S21 max) (représentée en rouge) avec résistance à deux sondes (en bleu). Il existe une variation douce de la transmission RF avec les oscillations de type Shubnikov-deHaas, car la fraction de remplissage diminue avec l'augmentation du champ magnétique.

2.1 Transmission RF dans le régime Quantum Hall

Nous avons mesuré l'impédance haute fréquence de ce circuit mésoscopique dans le régime Quantum Hall en mesurant la transmission RF à travers l'échantillon à l'aide d'un analyseur de réseau vectoriel. Nos resultats ont montré qu'aux fréquences de 4 à 8 GHz, le système chiral (électron gazeux) se comporte comme un transformateur d'impédance, avec ses règles spécifiques dictées par la chiralité due à l'effet Hall quantique. En particulier, le transport à travers les états de bord peut être décrit comme celui passant par une ligne de transmission unidirectionnelle et chirale. Pour les champs magnétiques où le facteur de remplissage est un nombre entier allant de 10 à 2, les excitations collectives (Edge-magnétoplasmons) ont une relation de dispersion linéaire et se propagent ainsi avec une vitesse linéaire avec la conductance de Hall. Les ondes de courant et de tension acquièrent une phase de propagation simple lorsqu'elles traversent l'appareil. Lors de l'exploration du plateau $\nu = 2$, nous avons expliqué les données en supposant un modèle de dissipation ohmique, où la conductance par unité de longueur varie en fonction du champ magnétique à travers le plateau. Lorsqu'un centre de diffusion tel que Contact Ponctuel Quantique

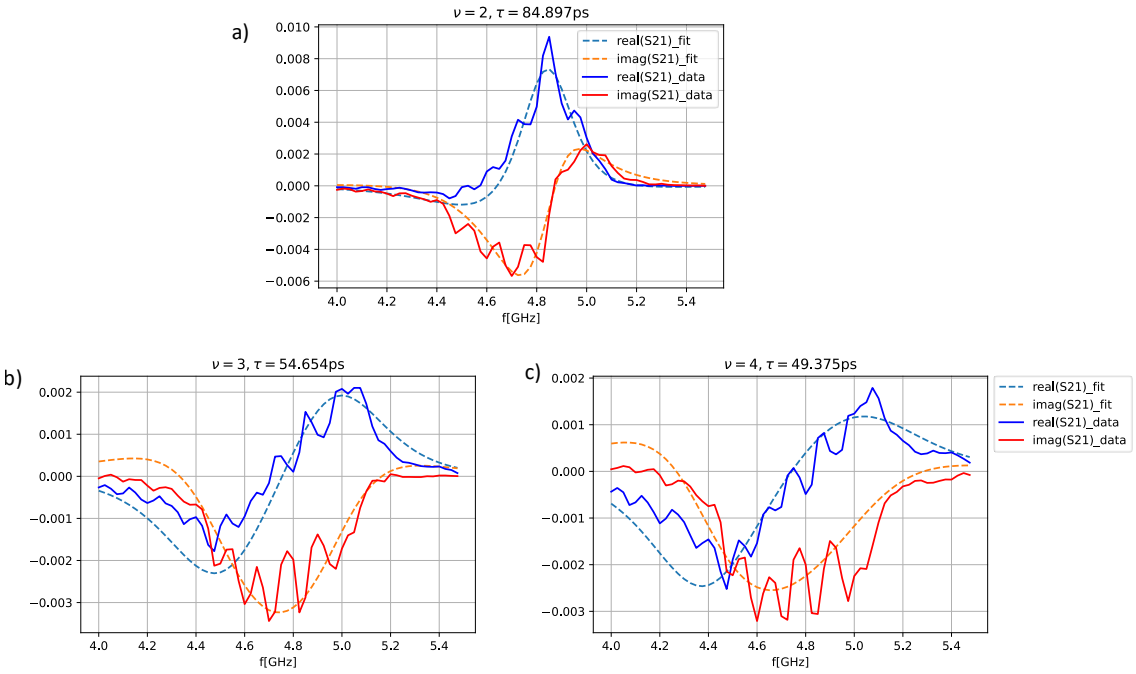

Figure 2.3: Courbes S21 pour $\nu = 2, 3$ et 4 avec ajustements. Les τ obtenus sont respectivement de 84,9 ps, 54,65 ps et 49,375 ps

est utilisé, les choses sont alors légèrement compliquées, mais fondamentalement, en suivant les règles générales de la théorie de la diffusion et en incorporant la propagation de phase des plasmons, cela peut être expliqué. A partir de la mesure du champ nul, nous avons pu caractériser la résistance interne de nos résonateurs et déterminer le gain de la chaine RF complète.

2.2 Mesures de bruit au plateau $\nu = 2$

Nous avons ensuite étudié le bruit haute fréquence émis par le Contact Ponctuel Quantique dans la chaine de détection dans différentes configurations d'échantillons. Cela a permis de comprendre le couplage micro-onde du bruit émis par le QPC à la chaine de détection. Grâce à la haute impédance de ces résonateurs, le couplage est meilleur qu'une ligne de 50 ohms, augmentant ainsi le S.N.R et réduisant le temps de mesure. Nos résultats montrent ici que pour une configuration à 3 points, le couplage du bruit est indépendant de la phase acquise par le signal de bruit lors du

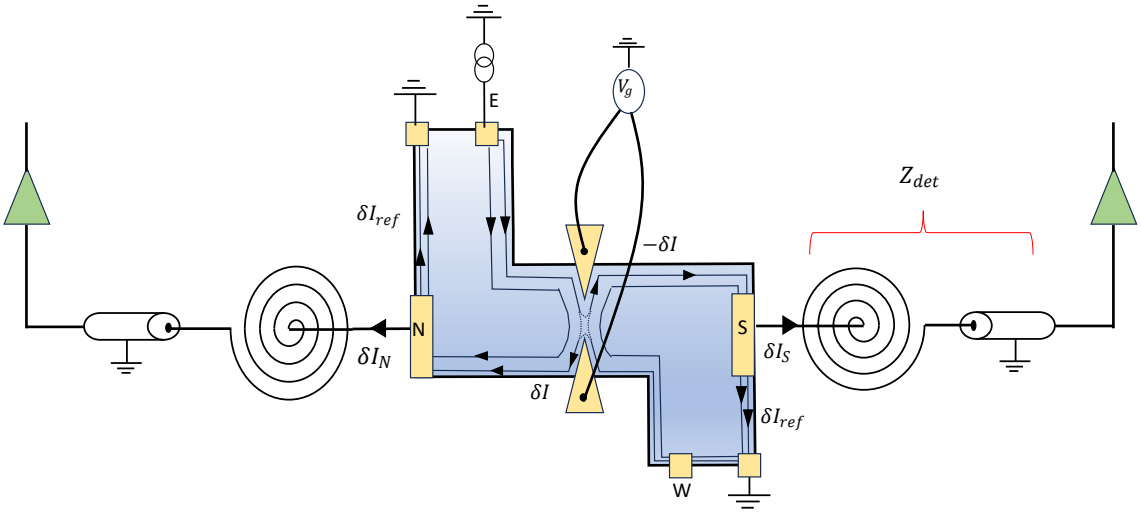

Figure 2.4: Schéma de circuit pour configuration 3 points. Le canal de bord intérieur est entièrement reflété par le QPC tandis que le bord extérieur est transmis avec une probabilité τ. Le bruit de tir du QPC est injecté dans le canal de bord extérieur des deux côtés de celui-ci, qui atteint ensuite le résonateur. La puissance reçue dans les lignes de détection est proportionnelle à δI_n et δI_s qui représentent une fraction de δI, le bruit de tir nu émis par le QPC, en raison du division actuelle.

passage du QPC aux résonateurs. En effet, il n'y a pas de retour des fluctuations de courant qui sont réinjectées dans le système, en raison des masses sur la puce. La densité spectrale de puissance détectée dans une configuration à 3 points est donnée par :

$$\frac{\delta P}{P_{off}} = \frac{1}{k_B T_N} \frac{(eV - hf)\tau(1-\tau)}{R_K} \frac{Re(Z_{det})}{|1 + 2G_K Z_{det}|^2} \tag{2.1}$$

Cela nous permet de quantifier le gain RF de la chaine de détection. La température de bruit des cryo-amplificateurs, telle que vue sur l'échantillon, est de 9,3K.

Dans une configuration à 2 points, cependant, il n'y a pas de masse sur puce. Cela conduit à un retour classique des fluctuations sur le QPC, faisant de la phase de propagation une grandeur importante. La densité spectrale de puissance détectée dans cette configuration est donnée par :

$$\frac{\delta P}{P_{off}} = \frac{1}{k_B T_N} \frac{\langle \delta I^2_{bare} \rangle Re(Z_{det})}{|1 + (2 - (1-2\tau)e^{-i2\phi_o}) \frac{Z_{det}}{R_K}|^2} \tag{2.2}$$

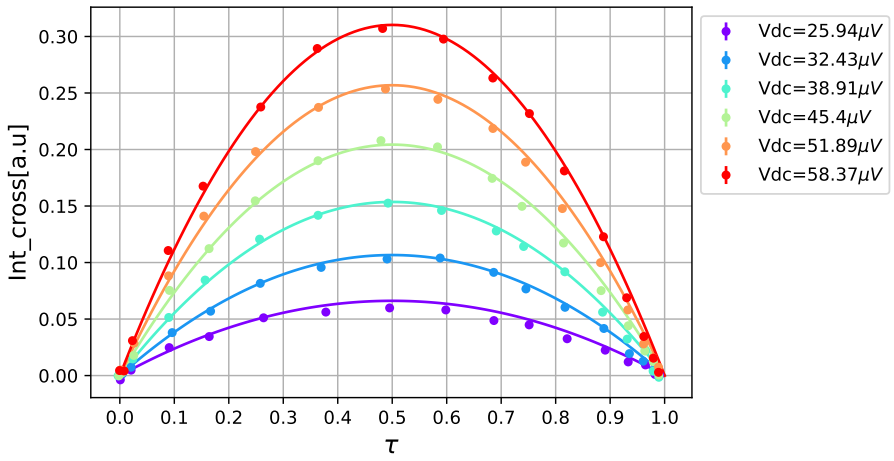

Figure 2.5: Dépendance de transmission de la puissance de bruit intégrée pour le canal de bord externe dans une configuration à 3 points. Il suit la dépendance canonique $\tau(1-\tau)$. Les lignes continues sont obtenues en additionnant la formule 1.1 sur la fréquence, où T_N est saisi sous la forme 9,3K

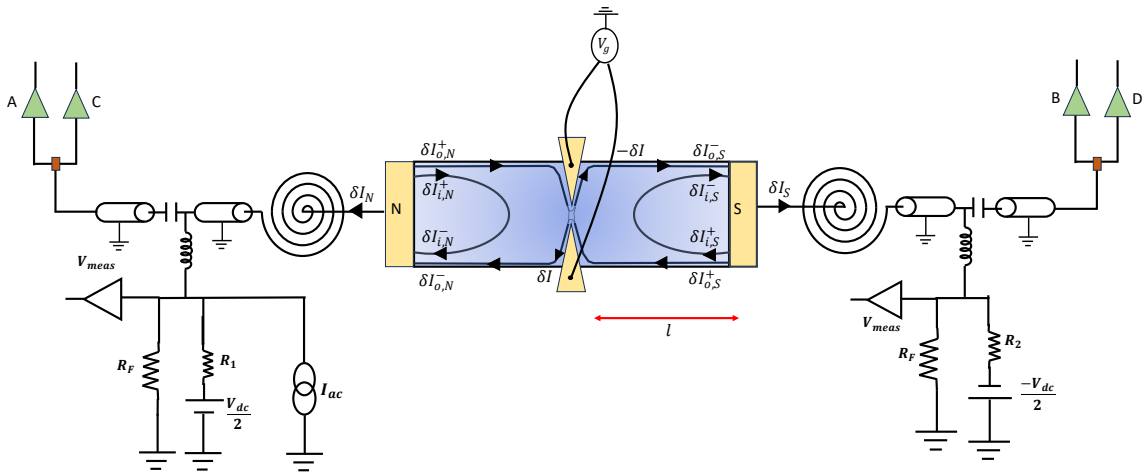

Figure 2.6: Circuit de bruit à 2 points : nous effectuons une polarisation différentielle à travers Quantum Point Contact. Sur le côté nord de l'échantillon, une petite polarisation de courant I_{ac} est appliquée via un amplificateur verrouillable et la tension est mesurée. Les résistances R_F à la terre de chaque côté sont de 12 kΩ. Ils nous aident à avoir une polarisation en tension. Côté RF, nous disposons de deux cryo-ampères sur chaque ligne de détection nous permettant de mesurer l'auto-corrélation avec précision. La division du signal émis par l'échantillon en deux lignes est effectuée par un coupleur hybride de -3 dB (représenté par un carré marron). Malheureusement, la ligne C a été déconnectée pendant la course.

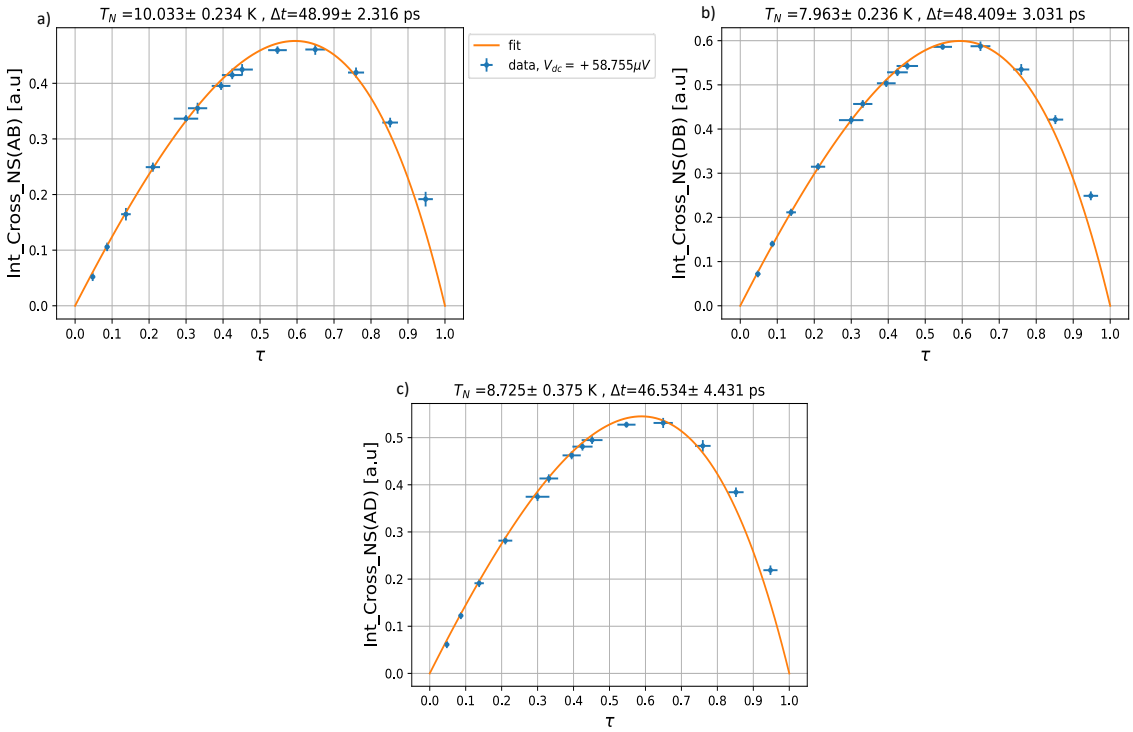

Figure 2.7: La puissance de bruit intégrée s'adapte à $V_{dc} = 58,7\mu V$ pour trois corrélations croisées nommées ici respectivement 'AB', 'AD' et 'DB' dans une configuration à 2 points.

En effectuant des ajustements de base avec les données expérimentales, nous avons pu extraire la valeur de la phase acquise ϕ_o (figure 2.7)

2.3 Quantum-Back Action of Resonators

Dans une troisième série d'expériences, nous avons exploré la rétro-action quantique des résonateurs sur le QPC, du fait que la rétroaction par les fluctuations du point zéro sur le QPC est toujours présente et que ces fluctuations sont importantes en raison de la grande impédance caractéristique de les résonateurs. La réduction observée de la conductance différentielle est un peu surprenante. D'une part, les effets sont observés à des valeurs de biais équivalentes au quantum d'énergie du résonateur mais ces effets observés ne sont pas aussi forts que ce que l'on pourrait attendre de la nature de l'environnement électromagnétique (valeur de l'impédance caractéristique). Nous soupçonnons qu'en raison de la taille finie du gaz d'électrons entre QPC et

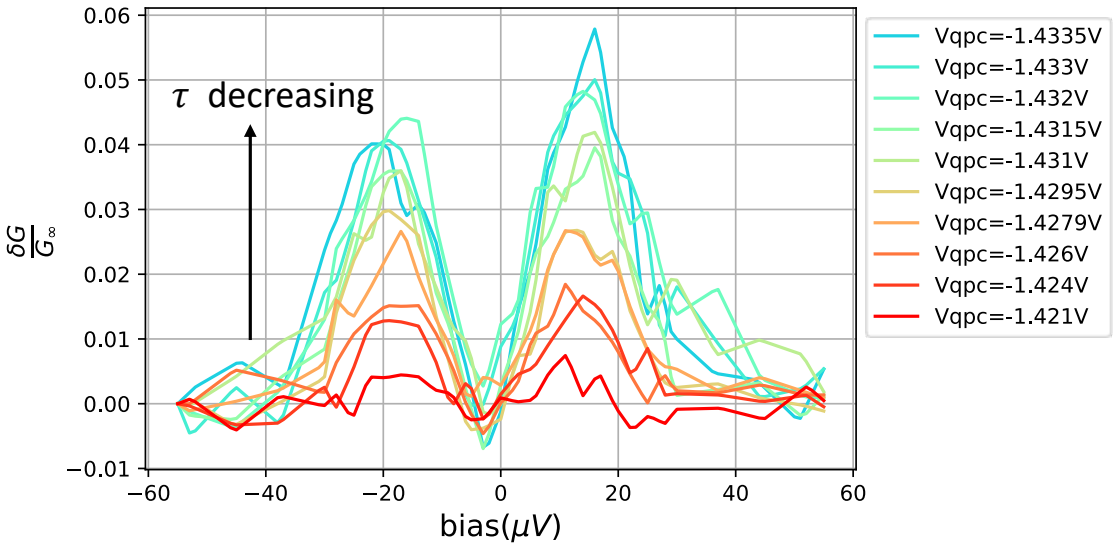

Figure 2.8: tracé $\delta G/G_\infty$ en fonction du biais appliqué. Nous constatons une réduction de la conductance à deux valeurs de biais ($\pm 20\mu V$) ($20\mu V \sim hf_o$), symétriques par rapport au biais nul. La réduction relative par rapport aux biais importants augmente davantage avec la diminution de la transmission.

les résonateurs, il se produit une transformation d'impédance de l'oscillateur LC, modifiant ainsi la nature de l'impédance de l'environnement. Nous ne comprenons toujours pas ce phénomène

2.4 Conclusion

En conclusion, nous pouvons dire que ce circuit mésoscopique contenant des résonateurs micro-ondes sur puce avec du gaz d'électrons en régime l'effet hall quantique est un bon moyen d'explorer la dynamique du gaz d'électrons, en découvrant ses propriétés d'impédance à haute fréquence et en transmettant également des informations sur la façon dont composer l'impédance de ce système chiral avec un circuit (résonateur) ayant une impédance comparable à celui-ci. De plus, grâce à ces connaissances, nous avons quantifier le couplage micro-onde du bruit émis par le conducteur quantique vers le circuit de détection et étudier la rétroaction quantique des résonateurs sur les conducteurs quantiques. Pour ces effets de blocage dynamique de Coulomb, peut-être qu'une taille plus petite de gaz électronique pourrait être utile, car elle aura

moins d'effets de propagation, donc des propriétés de transformation d'impédance plus faibles.

Chapter 3

General Introduction

The experimental work in this thesis lies in the field of Mesoscopic quantum transport. The systems studied here are electrical circuits that can be patterned by using standard techniques of Nano-Lithography. The conductors patterned are of the order of few fermi-wavelength of the charge carriers. These charge carriers, thus, maintain their quantum behavior while traversing through these conductors. And this quantum nature of carriers is manifested in the measured physical quantities such as current through the device. In order to observe this quantum behavior, though, these conductors need to kept at low temperatures. For that purpose, cryogenic refrigerators are used (see figure 3.1).

The conductors act as bottlenecks or scattering centre for the charge carriers. Due to this, motion of carriers through these conductors under the application of applied bias is probabilistic. Hence, the current through these devices always has inherent fluctuations in time (figure 3.2). In general, these conductors are embedded in some external circuit. This external circuit can be a transmission line (co-axial cable) for carrying signals from the device at cold temperature to the room temperature, LC oscillator for studying the response in a given bandwidth etc. Now, since the current fluctuates, it acts as source of electromagnetic radiation. This radiation, which one can think of as photons, interacts with this external circuit which are de-

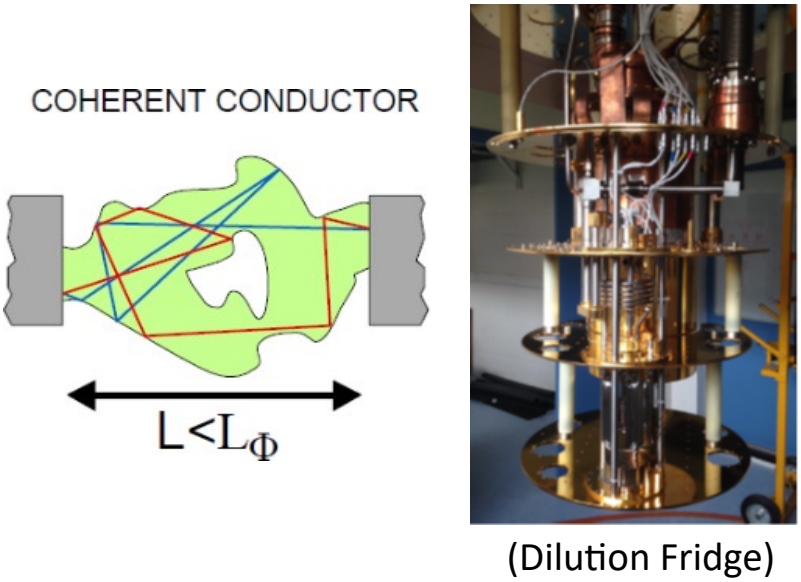

Figure 3.1: Mesoscopic size conductor. Electrons maintain their phase coherence while getting scattered through it. The size of this conductor is smaller than phase coherence length L_ϕ, so that phase coherence of carriers is maintained. This phenomenon is observed at low temperatures, that's why dilution refrigerators are needed. The picture shows Dry dilution refrigerator from Cryo-Concept used in our lab.

scribed by an impedance $Z(\omega)$. We would like to study this interaction of radiation with the external circuit. Our mesoscopic conductor is kept at about 20 mK. The frequency of photons which are thermally populated at this temperature is about 400 MHz. So, the radiation (photons) at these frequencies would already be present in the system in additon with the one radiated due to transfer of carriers through the conductors. That's why, we want to measure the dynamics of interactions at large frequencies, focusing only on the photons generated due to transport through

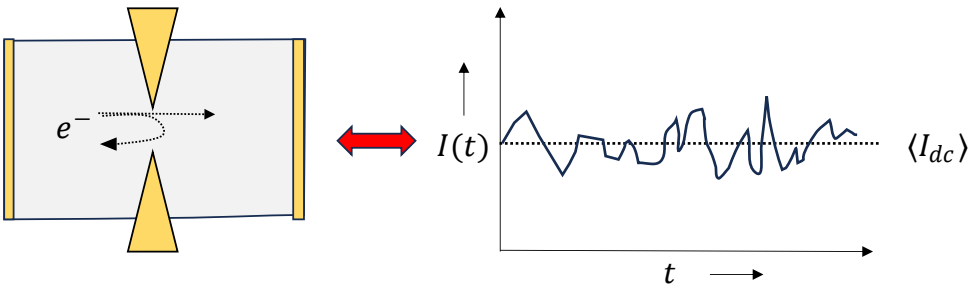

Figure 3.2: Passage of electrons through mesoscopic conductor leads to inherent fluctuations of current through device.

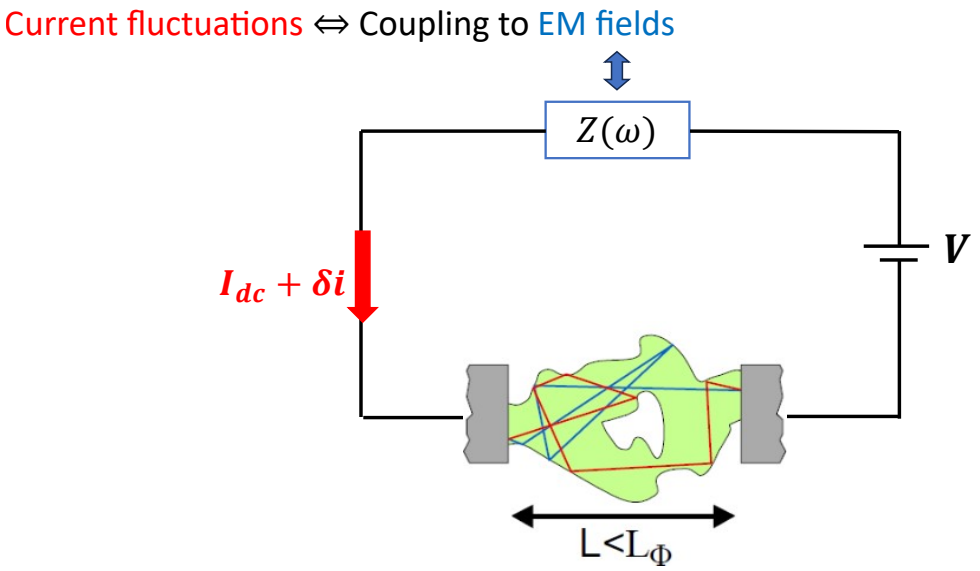

Figure 3.3: Full circuit containing mesoscopic conductor with external impedance.

mesoscopic conductor. For this reason, we have chosen to study in C-band of microwaves spectrum, in 4-8 GHz regime (figure 3.3).

One main question that would like to address is the nature of emitted photons due to electronic transport. Consider that external circuit is a transmission line that carries this signal from the sample at cold temperature to room temperature. Now, an interesting question that has been theoretically asked is, can these photons have same statistics as electrons? The answer to this question is yes and has been provided in (9),(8) (figure 3.4). For that we need a single channel of electrons where each transmitting electron emit a single photon. Now, the impedance of conductors having a single channel of electrons is about 26 kΩ while the impedance of standard transmission lines is 50Ω. This would produce a huge impedance mismatch, thereby, reducing the amount of power delivered to transmission line. To circumvent this issue, one can put an impedance transformer, which would increase the detected power and hence, signal to noise ratio.

So, to study these physics of photon emission through single channel, we first need a system that can provide us with single electron channels and where the mesoscopic conductor is patterned to produce radiation. For this reason, we have chosen GaAs semiconductor hetero structure based two-dimensional electron gas. The electron

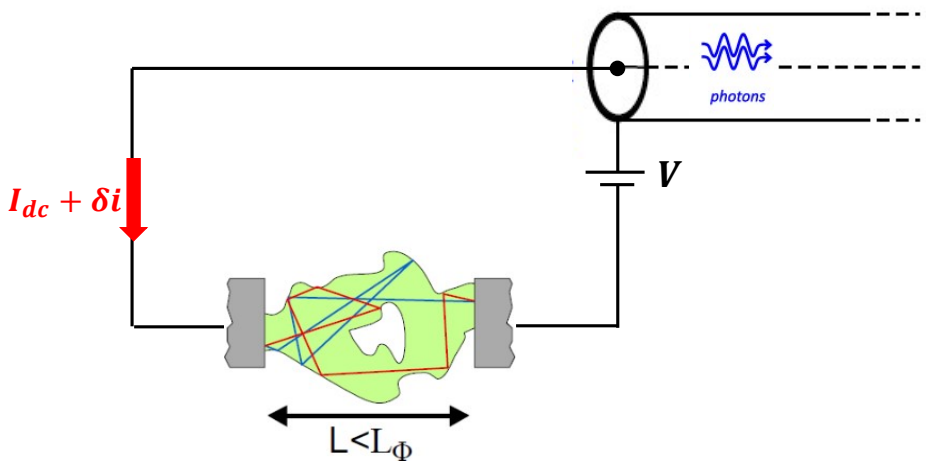

Figure 3.4: Circuit setup for measuring the statistics of emitted photons into transmission line (external circuit) due to transfer of electrons through mesoscopic conductor

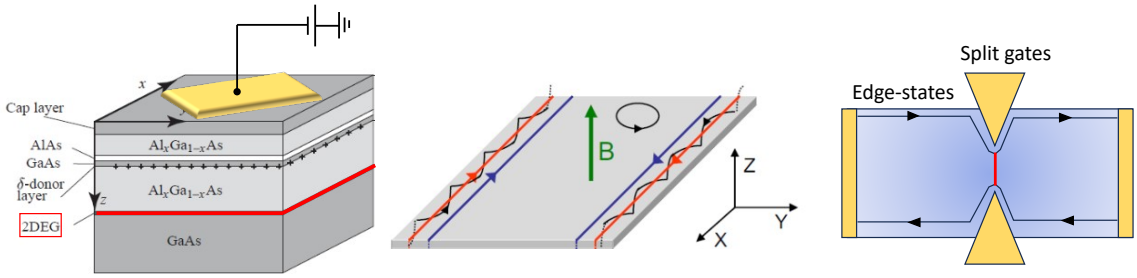

Figure 3.5: The platform for performing photon statistics experiments in single electron channel limit.

gas is formed at the interface of GaAs and GaAlAs (more in the next section) and has high mobility (in the sample that we use, it is about 560,000 cm^2/Vs). By depositing a metallic gate on top of this hetero structure and biasing it, we can have a field effect and thereby, tune the density of electron gas. Now in order to have electron channels, we work in quantum hall regime. Here our electron gas is placed in a perpendicular magnetic field. Due to this, cyclotron motion of electrons gets quantized and energy spectrum develops a gap in the bulk of the sample. There is no transport through the bulk of the sample. However, along the edges, states do exist that can carry the current through the device, but along a given direction. These chiral states, known as edge states, provide us with spin resolved channels at

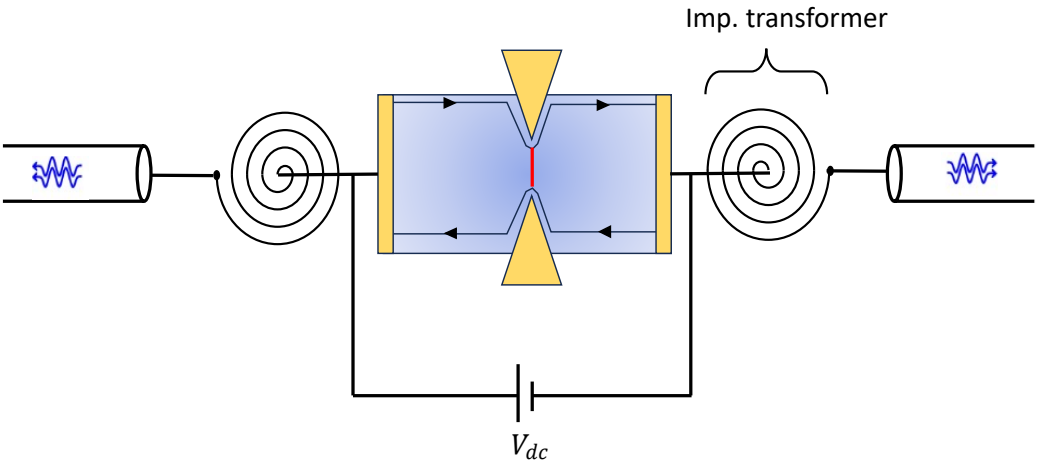

Figure 3.6: Schematic circuit for measuring photon statistics experiment

sufficiently high magnetic fields for electronic transport where motion of electrons through these states is ballistic. Now, with the deposition of specific geometry of metallic gates on top of the hetero-structure, known as split gates, these electronic channels can be selectively tuned, thereby, providing us with a full platform for studying the transport at high-frequencies and determining the nature of emitted photons.

In this thesis, in particular, two major experiments have been performed. First, the impedance of the sample (electron gas) is determined at high magnetic fields by radio-frequency transmission measurements. The nature of the impedance is important to know as it determines the amount of power that gets deposited into external(detection) circuit. Moreover, these results have revealed rich behavior of the physics of the electron gas at these high frequencies in the quantum hall regime, where transport is dominated by collective excitations. In the second set of experiments, Shot noise measurements are performed in two different circuit setups of the device which has allowed us to calibrate the noise measurement circuitry and also determine output impedance of our quantum conductor. These experiments provide full characterisation of the system at high magnetic fields and at high frequencies. The knowledge and insights gained here will be useful in performing photon statistics experiments that we originally aimed for.

In the coming sections, we explain the basic building blocks of our platform.

3.1 Two-Dimensional Electron Gas

In this thesis, the system on which experiments are performed is an electron gas confined in two dimensions. This gas of electrons is formed at the interface of semiconducting heterostructure. In our case, we use GaAs/AlGaAs heterostructure 2DEG. These are grown by Molecular Beam epitaxy technique and are provided to us by Antonella Cavanna and Ulf Gennser from C2N, Palaiseau, France.

In this technique crystal is grown layer by layer and during this course it is possible

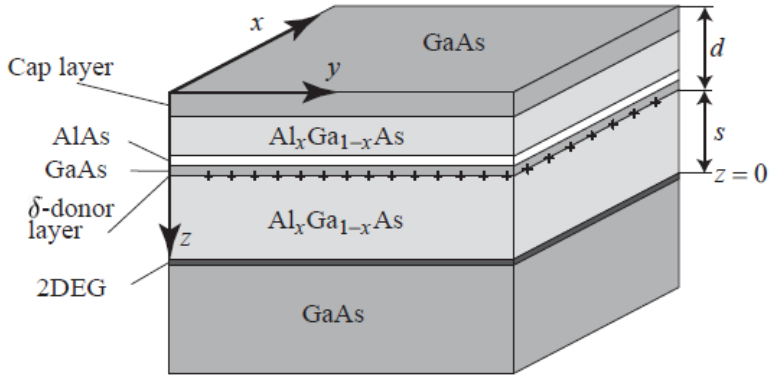

Figure 3.7: Layer sequence in MBE grown GaAs/GaAlAs heterostructure. 2-DEG can be seen in a thin confinement between GaAs substrate and $Al_xGa_{1-x}As$. (43)

to change the composition of GaAs such that it changes to $Al_xGa_{1-x}As$ suddenly at a crystal plane, which leads to the change in energy band structure.

One can engineer the bands not only by changing the composition of the material constituent during crystal growth but also by introducing atoms in relatively small concentrations at different lattice sites. This process is referred to as doping. Dopants that can release electrons into the conduction band through thermal activation (e.g., Si on a Ga lattice site in a GaAs crystal) are called **Donors**. Others which release holes in the valence band are called as **Acceptors**.

In GaAs, Si donors form bound states close the bottom of the conduction band. By

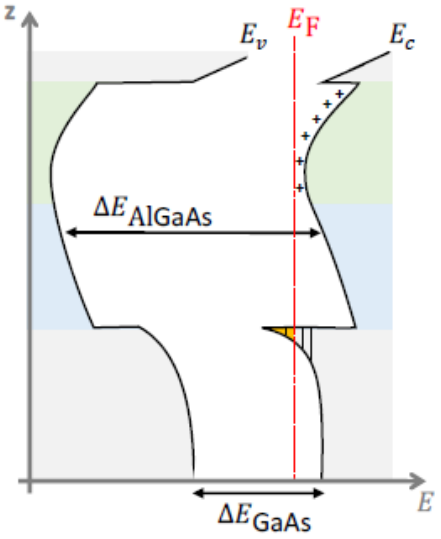

Figure 3.8: The band bending diagram of the heterostructure: As a result of charge equilibration the conduction band energy along the z direction forms a triangular quantum well, where the electrons are trapped, located approximately 100 nm below the surface.

using a special doping technique, known as δ-doping and putting in a spacer layer, one can reduce the electrostatic interaction between the 2D electron gas and these dopants, leading to high mobility.

The electrons in 2DEG are confined by a triangular potential well that results from the band bending at the interface of GaAs/GaAlAs. The confinement potential is a combination of the repulsive barrier due to the conduction band offset between the two semiconductors and the attractive potential due to the positively charged ionized donors left on the GaAlAs side.

The confinement of the electrons results in the quantization of the motion along the direction perpendicular to the interface, generating 2-dimensional subbands. Electrons are free to move in the plane of the interface but the transverse kinetic energy Ez takes only discrete values. In GaAs a typical energy separation between subbands is of the order of 10-40 meV. This means that at low temperature, typically below 100K, and low electrons density only the first subband is occupied and the system behaves as an effective 2-dimensional conductor.

3.1.1 Quantum Point Contact

Metallic Gates can be deposited on the heterostructure of GaAs/GaAlAs. Owing to the Schottky gap between the metal and GaAs,the gate does not couple galvancally. When a negative voltage is applied to these gates the carrier density of electron gas below can be tuned as a result of field effect. This is one of the reason why GaAs based 2DEG's are used as **High Electron Mobility Transistors (HEMT)** and are main components for cryogenic amplifiers. These amplifiers have very low input noise and thus are widely used in cryogenic condensed matter physics experiments, where one measures extremely low amplitude signals.

There exist a special arrangement of metallic gates which is very useful in mesoscopic transport experiments. This is called as **Split Gate** arrangement. The gates deposited have a gap between each other that is at max half a micro meter ($\sim 500nm$) large. By applying a negative gate voltage to this pair of split gates, one not only depletes the carrier density beneath them, but also forms a potential barrier in the gap region whose height depends on applied gate voltage. This potential barrier thus formed, is a constriction for the incoming electrons and acts as a scattering centre for them. These Split Gates are known as **Quantum Point Contacts**.

For high quality 2DEG's, the two-point conductance through the Quantum Point Contacts as a function of gate volage is quantised (77). The quantum of resistance here is half of Von-klitzing constant ($R_K \simeq 25812.8\Omega$) for zero magnetic field owing to the spin degeneracy.

To understand the Conductance through the Quantum Point Contact, let's first have a basic picture of Quantum Transport . The Two-dimensional electron gas is confined transversely to the direction of propagation of electrons. Since, the motion along longitudinal (along x) and transverse (along y) direction is independent, the wave function of the electron can be represented as : $\psi(x, y) = e^{ik_x x}\chi(y)$, where $\chi(y)$ represents the eigenstates due to confinement along y-direction. These states are also known as electronic modes. The energy of the charge carrier with a wave-vector

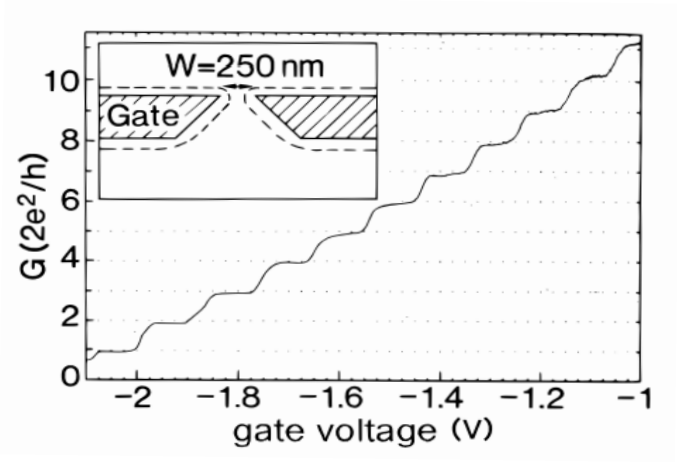

Figure 3.9: Quantized Steps of Conductance in Quantum Point Contact (7),(77). Inset shows Quantum Point Contact formed by Split gates.

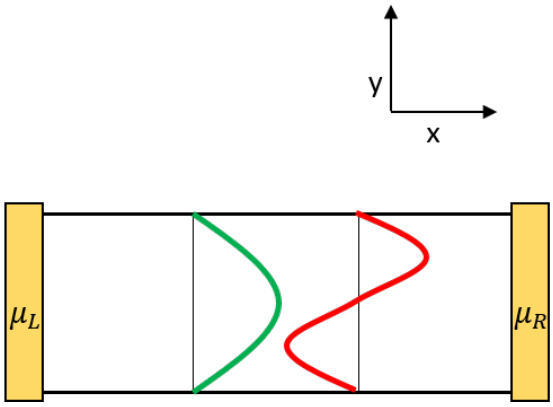

Figure 3.10: Illustration of transport in a 2DEG: The two eigenmodes for transport of electrons are shown schematically. Left contact has chemical potential μ_L larger than μ_R, but both are at same temperature **T**. The transport direction is along x-axis.

k_x and in the mode (or channel) **n** is given as:

$$E_{k,n} = E_n + \frac{\hbar^2 k^2}{2m} \tag{3.1}$$

The current contribution for a given mode in an infinitesimal energy interval dE is:

$$dI_n = \pm 2ev(E)dn(E)f_{\pm}(E) \tag{3.2}$$

Where $dn(E)$ is the number density of carriers per unit length, $f(E)$ is fermi-

distribution, telling us about probability of the state being filled at energy E. Factor 2 is spin-degeneracy. The signs tells us direction of current. The Density of states : dn/dE in 1-D is simply given as $\frac{1}{hv}$. Substituting this in above equation, we get the current in terms of energy differential

$$dI_n = \pm\frac{2e}{h} f_{\pm}(E)dE \tag{3.3}$$

The net current is given by taking the difference of + and- terms (or left and right terms). Here $\mu_L - \mu_R = eV_{dc}$. Integrating equation 3.3 with taking difference gives us:

$$I_n = \frac{2e}{h}\int (f_L(E) - f_R(E))dE \tag{3.4}$$

Since this current is independent of the mode, the total current is just sum of it.

$$I_{tot} = \frac{2e}{h}\sum_{n=1}^{N}\int (f_L(E) - f_R(E))dE \tag{3.5}$$

Now, the bias V_{dc} applied is negligible compared to fermi energy E_F [1]. One can approximate the difference $(f_L(E) - f_R(E)) \sim -\frac{\partial f_L(E)}{\partial E} eV_{dc}$. Substituting this expression into 3.5 and dividing by the voltage V_{dc}, we get

$$G = \frac{2e^2}{h}\sum_{n=1}^{N} f_L(E_n) \tag{3.6}$$

At zero temperature, this simply reads as ,

$$G = \frac{2e^2}{h}N \tag{3.7}$$

So, each channel contributes a conductance $G_o = \frac{2e^2}{h}$. The above situation describes what is called as ballistic transport. Here, even though there is no scattering in the

[1] It is typically in few micro electron volt whereas fermi energy is in meV

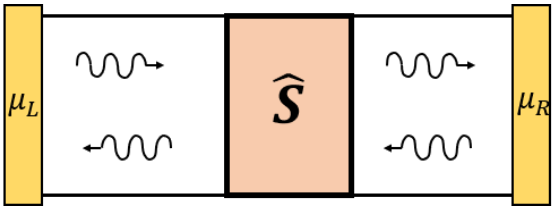

Figure 3.11: Scattering centre in a two-point geometry. The incoming electrons from left/right contacts are reflected or transmitted with some finite probability to the other side.

sample, but still the each channel has a resistance of $\frac{h}{2e^2}$. This resistance arises due to the dissipation that happens at the contacts.

Now, since we have the basic picture of origin of quantised conductance, we can proceed further to include a scattering centre in our device and see how the transport is modified. The approach followed here is that of scattering theory, which is commonly referred in this field as **Landauer-Buttiker Formalism**. It relates the transport properties of the sample (like current, noise, etc..) to the scattering properties that are assumed to be known from quantum mechanical calculations.

To pictorially represent the situation, consider the figure 3.11,which has a scattering centre. It is described by a Scattering Matrix **S**. The electronic states are described by the creation and annihilation operators which are defined for each lead connecting reservoir to the scattering centre. They obey the following anti-commutation rules:

$$\{a^+_{Ln}(E), a_{Ln'}(E')\} = \delta_{n,n'}\delta(E - E') \tag{3.8}$$

The scattering field operators $b^+(E)$ and $b(E')$ are related to $a^+(E)$ and $a(E)$ by

the following form:

$$\begin{bmatrix} b_{L1} \\ b_{L2} \\ \dots \\ b_{Ln} \\ b_{R1} \\ b_{R2} \\ \dots \\ b_{Rn} \end{bmatrix} = \hat{S} \begin{bmatrix} a_{L1} \\ a_{L2} \\ \dots \\ a_{Ln} \\ a_{R1} \\ a_{R2} \\ \dots \\ a_{Rn} \end{bmatrix} \tag{3.9}$$

The current in a given lead is expressed as an operator and is given as:

$$\hat{I_L}(t) = \frac{2e}{h} \sum_n \int dE dE' e^{i(E-E')t/h} [a^+_{L,n}(E) a_{L,n}(E') - b^+_{L,n}(E) b_{L,n}(E')] \tag{3.10}$$

Now,the quantum statistical average of the product of creation and annihilation operators is given as:

$$\langle a^+_{L,n}(E) a_{L,n}(E') \rangle = \delta(E - E') f_L(E) \tag{3.11}$$

Utilizing this in equation 3.10, we obtain the average current.

$$\langle \hat{I} \rangle = \frac{2e^2}{h} \sum_n \int dE T_n(E) (f_L(E) - f_R(E)) \tag{3.12}$$

By using the same approximation regarding fermi function used in equation 3.6, we obtain conductance as:

$$G = \frac{2e^2}{h} \sum_n \int dE T_n(E) \left(-\frac{\partial f_L(E)}{\partial E} \right) \tag{3.13}$$

To interpret the above conductance we need to have a reasonable concrete model

for the potential provided by the scattering centre to the incoming electrons. This will allow us to know how transmission $T(E)$ changes as we tune potential profile of scattering centre. In our case, this scattering centre is Quantum Point Contact and by applying gate voltage we can change the potential profile and hence, transmission for a given energy. The most used model for Quantum Point Contact is the **Saddle Point Model** developed by Buttiker (14).

Here the potential felt by incoming electrons is of the following form:

$$V(x,y) = -\frac{1}{2}m\omega_x^2 x^2 + \frac{1}{2}m\omega_y^2 y^2 + V_o \tag{3.14}$$

The confinement along the y-axis (transverse direction) is harmonic-type potential, which give us with subband energies as : $E_n = \hbar\omega_y(n + \frac{1}{2})$ .The transmission probability $T_n(E)$ of the nth mode can be expressed analytically as :

$$T_n(E) = \frac{1}{1 + e^{-2\pi\epsilon_n}} \tag{3.15}$$

where the energy parameter, ϵ_n is given as:

$$\epsilon_n = \frac{E - \hbar\omega_y(n + 1/2) - V_o}{\hbar\omega_x} \tag{3.16}$$

If for given n , $E << \hbar\omega_y(n+\frac{1}{2})+V_o$, then transmission is suppressed exponentially, whereas for $E >> \hbar\omega_y(n+\frac{1}{2})+V_o$ it is close to 1. It is half at $E = \hbar\omega_y(n+\frac{1}{2})+V_o$.

So, we see how the conductance quantisation happens for transport through a Quantum Point Contact. The above basic picture was given for a ballistic conductor, where scattering events only happens at the quantum point contact. In realistic devices, one can have static impurities which leads to scattering of electrons at those impurity sites, in addition to the scattering at QPC. So the net transmission is the sum of amplitudes from all the paths (impurity + QPC) and leads to smearing and even disappearance of the conductance plateaus even though the entire system

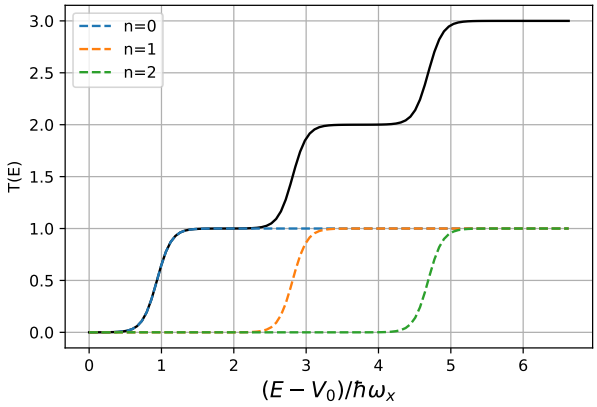

Figure 3.12: Transmission for n= 0,1,2 subbands for Saddle Point Model. Black curve represents the total transmission $\sum_n T_n$

is at very low temperature (20mK). One can get rid of this back-scattering due to the impurities pretty much by studying the transport in High perpendicular magnetic field. This is the field of **Quantum Hall Effect** and is the regime where we have done most of our studies of RF transport. Following few pages will give an introduction to Quantum Hall Effect.

3.2 Quantum Hall Effect

Hall Effect was first seen in semiconductors in 1890's by Edwin Hall (38). When a perpendicular magnetic field is applied to the semiconductor (fig 3.13) which is biased, let's say, in the y-direction, a current develops in the transverse direction which is proportional to the applied perpendicular field B. The resistance along this transverse direction follows a straight line with B and is known as Hall Resistance **Rh**.

Almost 100 years later, in the year 1980, Von Klitzing (48), while studying the electron gas in inversion layer of silicon **MOSFET** under high magnetic field in NEEL institute Grenoble observed that hall resistance becomes quantised in units containing only fundamental constants , h and e. This unit of resistance is called as R_K, the Klitzing constant and has metrological importance . It's measured value is

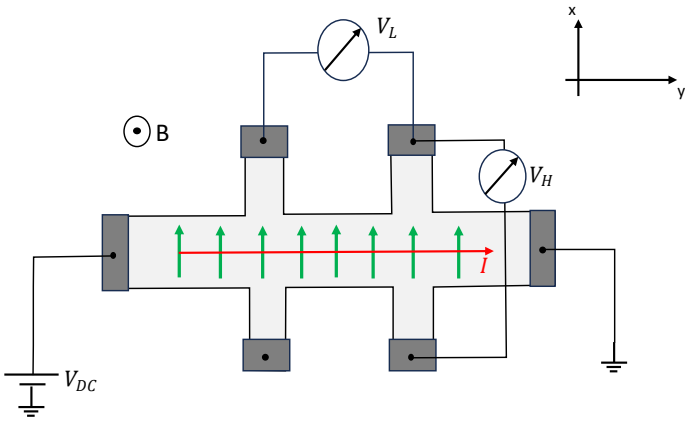

Figure 3.13: 2-D Hall Bar Geometry: In a steady-state situation when a current I(shown in red) is flowing through the bar, at a constant magnetic field B a Hall voltage develops transverse to the current flow (field lines shown in green).This voltage increases linearly with B.

:

$$R_K = 25812.80745...\Omega \tag{3.17}$$

The inversion layer MOSFET did not had a good mobility but still the exact quantisation of Hall resistance was observed and was surprising. It was the first universal result seen in semiconductor physics and this value is now used to ascertain the fine-structure constant. Prior to that the fine-structure constant was only determined in atomic physics experiments.

3.2.1 Landau Quantisation

We derive here the Landau level energy spectrum of a an electron under a strong perpendicular magnetic field **B** . For more details, one can refer to (81).

The electrons, being in 2DEG are confined in x-y direction, magnetic field is along z- axis. We use Landau gauge i.e $A = (0, Bx, 0)$. The Hamiltonian of an electron is given as :

$$\mathbf{H} = \frac{1}{2m}(p + eA)^2 \tag{3.18}$$

expanding the above hamiltonian, we get :

$$\mathbf{H} = \frac{1}{2m}[p_x + (p_y + (eA))]^2 \tag{3.19}$$

Since, the Hamiltonian is translationally invariant along the y-direction, the wave function $\Psi(x, y)$ can be decomposed as a product of a function dependent on x and a plane wave moving along y-axis.

$$\Psi(x, y) = \chi(x)e^{iky} \tag{3.20}$$

Schrodinger's Equation for the function $\chi(x)$ then becomes,

$$[\frac{1}{2}p_x^2 + \frac{1}{2}m\omega_c^2(kl_B^2 + x^2)]\chi(x) = E\chi(x) \tag{3.21}$$

Here, $\omega_c = eB/m$ is the cyclotron frequency and $l_B = \sqrt{\frac{\hbar}{eB}}$ is the magnetic length. The above equation is similar to that of the one-dimensional harmonic oscillator whose minimum is shifted to $-kl_B^2$. Depending upon the value of $\mathbf{k}$, the electron wave-function along x-axis has different central position. The eigenvalues of the energy are that of the harmonic oscillator, parametrized by this $\mathbf{k}$ value.

$$E_{n,k} = \hbar\omega_c\left(n + \frac{1}{2}\right) \tag{3.22}$$

Clearly, if we know how many $\mathbf{k}$ values are allowed in our finite sized two -dimensional electron system, we can calculate the number of the states with the same energy E_n. For that , we assume periodic boundary conditions along y-axis. This means that :

$$k_y = \frac{2\pi}{L_y}n \tag{3.23}$$

is quantized and takes only discrete values. Since the x- values are dependent on $\mathbf{k}$, the spacing between the consecutive centres of the wave-functions with same energy is : $\Delta x = \Delta k_y l_B^2$. Dividing the length along the x-axis i.e L_x by the spacing

gives the degeneracy of Landau levels with Energy E_n.

$$N = \frac{L_x}{\Delta x} = \frac{L_x L_y B}{h/e} \tag{3.24}$$

The term $L_x L_y B$ is the total flux Φ and the ratio $\frac{h}{e}$ is the flux quantum Φ_o.

$$N = \frac{\Phi}{\Phi o} \tag{3.25}$$

Thus, the degeneracy is equal to the number of flux quanta threading the sample.

3.3 Motion Under Electric field

In the presence of the Electric field $\vec{E} = (E, 0, 0)$, the potential term $V = -eEx$ adds to the Hamiltonian in equation 3.19. This potential translates the landau wave-function to new position

$$x_k = -kl_B^2 - \frac{mE}{eB^2}$$

and modifies the eigen-energy as follows:

$$E_{n,k} = \hbar\omega_c \left(n + \frac{1}{2}\right) - eEx_k + \frac{1}{2}mv_D^2 \tag{3.26}$$

Here $v_D = \frac{E}{B}$ is the drift velocity with which electrons drift. This electric field is usually developed when a voltage is applied across the y-direction. This leads to the current density $j_y = nev_D$, such that Hall conductivity $\sigma_{xy} = \frac{n_e e}{B}$ and the longitudinal conductivity $\sigma_{xx} = 0$. Now, if n number of Landau Levels are fully filled, it means that the total number of electrons are occupying all the degenerate states of these landau levels. The number of degenerate states per unit area for a given landau level is given in equation 3.25. Total degeneracy per unit area is n

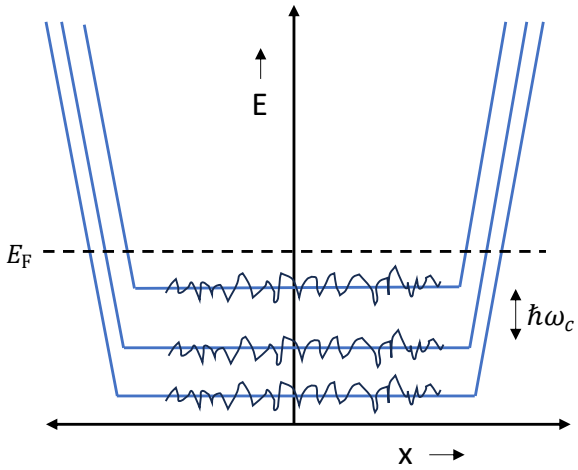

Figure 3.14: Landau Levels. We show here three of them below Fermi Energy. The confining potential at the edges makes the levels rise in energy as we go closer to the edge. The disorder potential in the bulk of sample is drawn here as random variation of Energy in the bulk as a function of position x.

times this number, which is equal to electron density in the sample.

$$n_e = \frac{n}{2\pi l_B^2} \tag{3.27}$$

If we substitute this expression for electron density n_e in Hall conductivity, the 2D conductivity is given as:

$$\sigma_{xy} = \frac{ne^2}{h} \tag{3.28}$$

The number n is known as filling fraction.

3.3.1 Edge States

Since, the sample has finite size, the edges provide the confining potential $U(x)$ to the electrons. This potential leads to a modification of the landau levels along the edges. It's eigen-energies will be modified from equation 3.22. They are pictorially depicted in figure 3.14. One can think of this potential as providing electric field at the edges to the electrons. In order to see this, we assume that this confinement potential varies smoothly over the magnetic length l_B. Then, the eigen-energies can

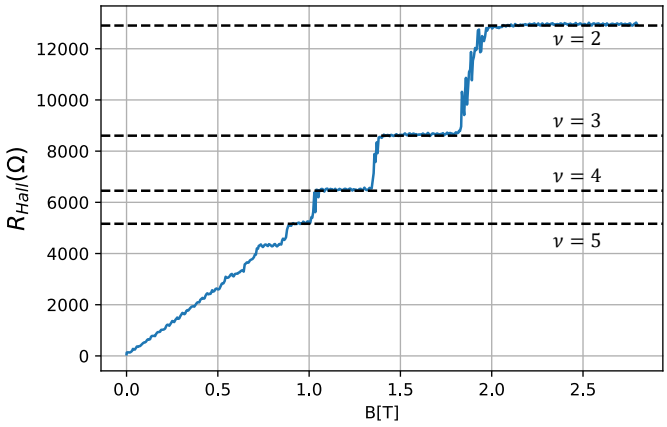

Figure 3.15: Hall resistance as a function of magnetic field. It is quantised in integer fractions of Von-Klitzing constant R_K.

be written as:

$$E_{n,k} = \hbar\omega_c \left(n + \frac{1}{2}\right) + U(x_k) \tag{3.29}$$

From the above equation, the velocity along the edge comes out to be:

$$v = \frac{1}{eB}\frac{\partial U(x_k)}{\partial x_k} \tag{3.30}$$

In the above expression $\frac{\partial U(x_k)}{e\partial x_k}$ plays the role of electric field. So, the electrons drift along the edges of the sample. When the Fermi level lies in between the landau-levels, then the current is solely carried along the edge of the sample.

3.3.2 Role of Disorder

The explanations given above tells that indeed we do observe Hall resistance which is $\frac{h}{ne^2}$ (from 3.28), but that it is only for a very small range in the value of the Magnetic field where the edge channel exist. Whereas experimentally, one observes the 'plateaus' in the Hall resistance curve vs magnetic field (figure 3.15). This effect is explained by disorder in the system.

We assume that disorder potential is smooth, its amplitude is smaller than both cyclotron and zeeman gap and its gradient is smaller than $\frac{\hbar\omega_C}{l_B}$ and $\frac{\Delta_Z}{l_B}$ where Δ_Z

is the zeeman energy which matters when magnetic field is sufficiently strong and leads to spin-polarized landau levels. When these constraints for disorder are met, then it cannot mix-up spin split landau levels and can only be added adiabatically to their energy (see figure 3.14). This creates hills and valleys of potentials in the bulk region. When the Fermi Level crosses this hill or valley, it also leads to states with a velocity just like edge states. But, these states just encircle these hills and valleys rather than providing any contribution to the current.

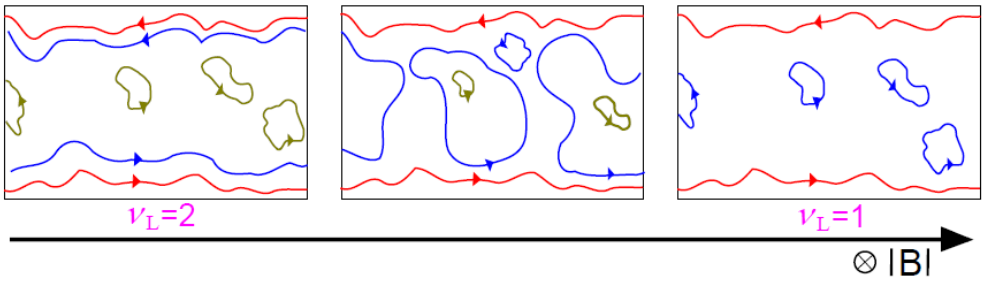

Figure 3.16: Localized and extended states in a dirty sample. Drifting states crossing the Fermi energy in a dirty sample originating from the lowest (red), 1st (blue) and 2nd (yellow) Landau levels. Edge channels are perfectly transmitted along the sample. Drifting states arising from disorder are localized within the bulk. The transition between two situations having a well defined number of edge channels is driven by the percolation of the innermost (here, the blue) edge-channel.

3.3.3 Percolation

For macroscopic samples, the drifting bulk states furnish a reservoir of localized states (see figure 3.16). At a fixed density, sweeping the magnetic field will change the size of the localized orbits.Therefore, even if they do not contribute to transport, they pin the Fermi energy between two Landau levels for wider ranges of magnetic field. Following this picture, the transition between two situations having a distinct number of well defined edge channels is driven by the percolation of the innermost edge channel.

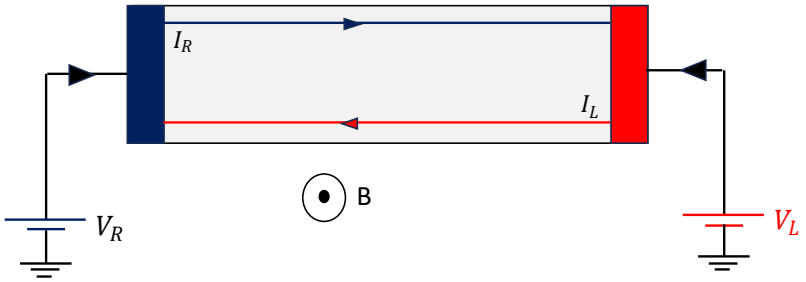

Figure 3.17: Two port conductor having one edge state ($\nu = 1$) on both edges. They carry the potential of the contact from where they origin (here it is displayed as the color of these edge states). We assume that $V_R > V_L$.

3.3.4 Buttiker's Picture for Edge transport

We have seen that when biased, the current in the Integer Quantum Hall regime is carried solely by the edge states. When on the Hall plateau there is no backscattering since the measured longitudinal resistance is zero. Hence, these edge channels become pathways for the ballistic transport. By noting these properties of the edge states, Buttiker(13) put forward his theory of transport in Quantum Hall regime via edge channels. As discussed in the previous section on scattering formalism, we observe that these edge channels can be seen as modes where the current propagates from one contact to the other. One can thus use all the tools of the scattering formalism to calculate current, conductance etc from it in Quantum Hall regime. We will illustrate it by calculating the two probe resistance of a Hall bar having only one edge state flowing between two contacts. Because of the chirality, these edge states carry the potential of the contact from where they origin. This leads to the current expressions as follows:

$$I_L = e \int v_D \nu(E) f_L(E - eV_L) dE$$
$$I_R = e \int v_D \nu(E) f_R(E - eV_R) dE$$

where v_D is the drift velocity along the specific edge, $\nu(E)$ is the density of states and f_L, f_R are the fermi-functions of the contacts, respectively. Now, since this

transport along edge states can be thought of as in 1-D, density of states are inversely proportional to velocity. Substituting this information in the above current expressions, and noting that net current is $I_R - I_L$, we obtain:

$$I_{net} = \frac{e^2}{h}(V_R - V_L)$$

The two-point resistance is thus, $R_{2pt} = \frac{h}{e^2}$ (see figure 3.17). For samples that have elastic scattering at high magnetic fields, as long as cyclotron radius is smaller than the elastic mean free path length, this scattering is always suppressed. More generally, Buttiker explained how Hall measurements of resistance be affected if one has disordered contact, what happens when inelastic scattering occurs and why is Hall effect is quantized for larger samples. These investigations help established the nature of edge states and the dispersion curve depicted in figure 3.14.

3.3.5 C.S.G picture of Edge States

All the previous considerations are based on the idea of single electron picture. Since electrons are charged, they will have interactions among other electrons. These interaction effects should in principle modify the Energy band structure (here it means changing the confining potential in a self-consistent way) and also should affect the distribution of electron density in the two-dimensional electron gas. The modifications of landau levels that happens by considering these interactions is done by studying how electrostatic energy changes across the sample (16),(4).

It shows that landau level energy does not rise continuously as one approach to the edge. But, rather rises in a step like fashion. In general, the filling factor $\nu = n_o 2\pi l_B^2$ is not an integer, here n_o is electron density of the gas in the bulk at zero magnetic field. Then as the field is swept up, that integer Landau-level will get depleted. After it has fully depleted, the fermi level has to go to Lower landau-level. But to

do so, it requires to change energy by exactly $\hbar\omega_C$. Hence, the electrostatic potential changes by this amount till fermi-level gets aligned with landau level. During this process, there is no state available for the electrons to go, so there density remains constant. This process leads to the formation of incompressible and compressible strips. The magnetic field leads to formation of these strips.

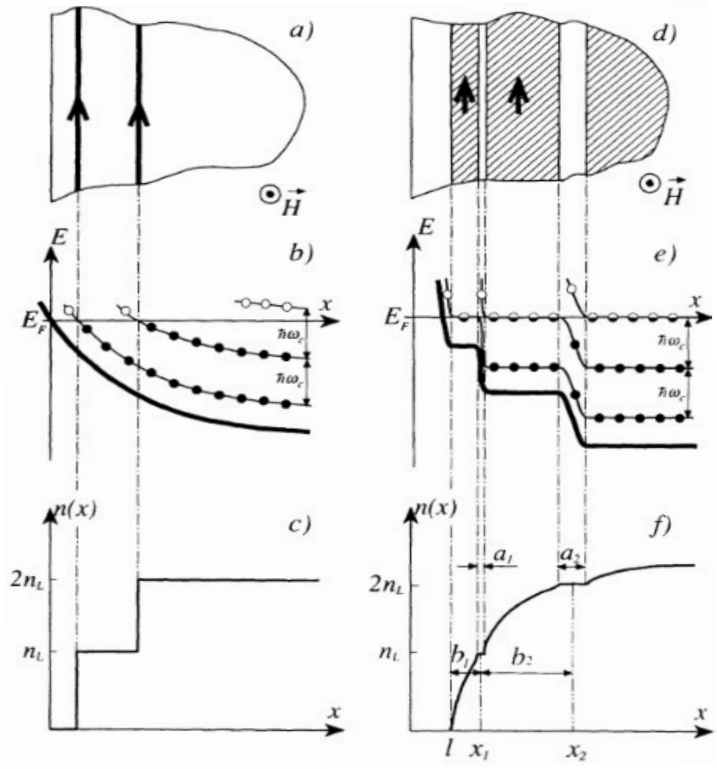

Figure 3.18: From (16). (a), (b), (c) depicts the Buttiker picture of edge-states based on non-interacting electrons. There the density changes abruptly at the edge as one less fully filled landau level cuts the Fermi-level. The confinement potential is considered as smoothly varying. Whereas in (d), (e), (f) Confinement Potential changes owing to the screening done by electrons in 2DEG. The step like fashion change is due to in-compressible and compressible stripes. Since there are no states in in-compressible strip, it does not changes the density, while compressible strip has non-zero density of states, density there follows the dependence like that of zero field 2DEG acted upon by side-gates.

3.4 Magneto-Plasmons

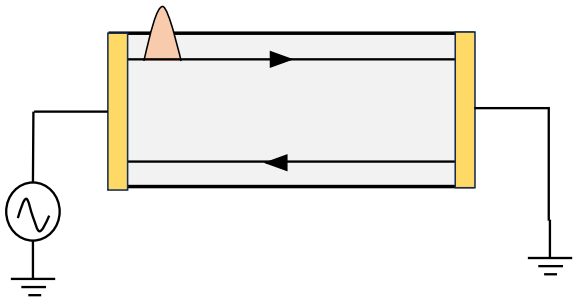

Figure 3.19: Schematic illustration of charge disturbance created by an ac-drive that travels along the edge states.

We have presented in the previous sections the theory and formalism of DC-Transport in the Hall-bars. The notion of Edge-states as ballistic channels for electrons neatly explains the transport measurements done in DC in Integer Quantum Hall Regime. With Scattering centre such as Quantum Point Contact, one can use them as beam-splitter to probe the phase-coherence length of electrons (72), do energy spectroscopy measurements for inner and outer edge channel, where dissipation mechanisms are probed (3), and much more. In this thesis, we probe the physics of our two-dimensional electron gas with or without scattering centre in radio-frequency regime.

More generally, the RF transport under perpendicular magnetic field is described by collective excitations that carry the signal. From pioneering experiments in mid 1980's done in non-degenerate two-dimensional electron gases (34),(58), it is shown that spectrum of collective excitation have two-branches: The one whose frequency increases with magnetic field, called as Bulk-magnetoplasmons, whereas the other whose frequency decreases with magnetic field, called as Edge-magnetoplasmons.

In the quantum Hall regime, where transport happens along the edges, these edge-magnetoplasmons are sole carriers of the AC signal. Classically, one can think of them like a disturbance in the electron density which propagates from one contact to other. In the regime of relatively low magnetic field, where longitudinal and Hall resistance are both finite and the edges of the sample are sharply defined, Volkov

and Mikhailov (78) gave the expression for the dispersion relation for these edge-magnetoplasmons.

$$\omega(k) = \frac{\sigma_{xy} k}{2\pi\epsilon_0\epsilon}\left(ln\left(\frac{2}{kL}\right) + 1\right) \tag{3.31}$$

where L, given as:

$$L = i\frac{\sigma_{xx}}{2\omega\epsilon_0\epsilon} \tag{3.32}$$

describes the transversal spatial extent of the edge-plasmons. There have been many experiments done to learn more and more about these edge excitations. These include in particular, time-domain measurements where a voltage pulse of definite width and magnitude is sent through the device and the resulting outgoing pulse is measured, which reveals information about dispersion relation, velocity and dissipation of the edge excitation (5),(49),(46),(84),(37). When at integer Quantum Hall regime , having integer filling fraction (let's say $\nu = 2$), $\sigma_{xx} \to 0$, then these measurements reveal that spatial width of edge-excitations is that of compressible edge stripes and not given by 3.32. In Fujisawa's group (46),(49), they measured

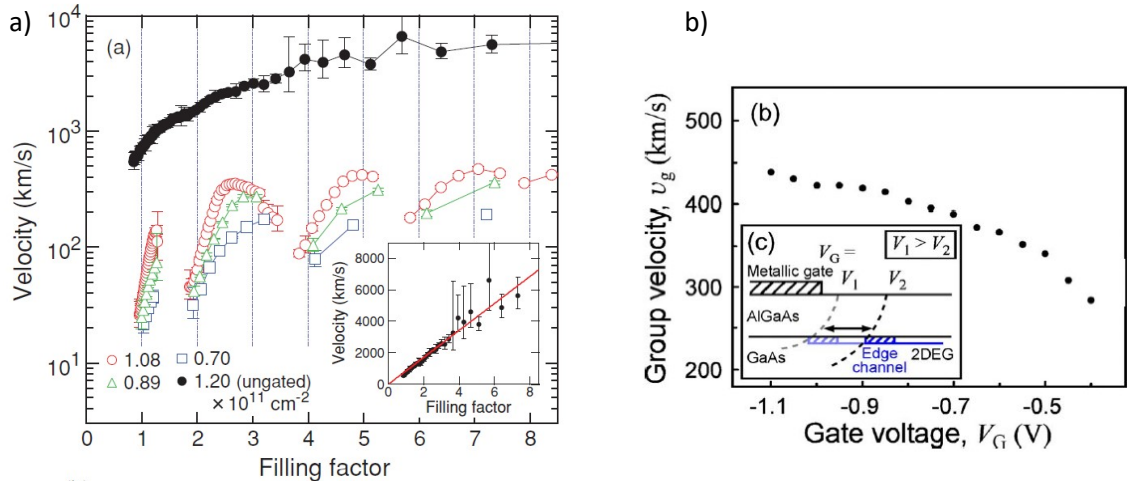

Figure 3.20: a) Velocity dependence for gated and ungated sample as a function of filling factor (49). The velocity for EMP is larger for the ungated sample than that for gated sample due to screening provided by the gates. b) The velocity vs gate-voltage curve at a fix filling factor. Velocity increases as the gate-voltage becomes more negative (46)

the velocity dependence vs filling factor and found that for a given edge-profile, the

edge-magnetoplasmon velocity is proportional to Quantum Hall Conductivity. And also when the edges of the sample are gate-defined, then at a fixed filling factor, the velocity increases with more negative voltage (see figure 3.20b). This implies that velocity depends inversely upon the capacitance C_H to ground.

$$v_{emp} = \frac{\sigma_{xy}}{C_H} \tag{3.33}$$

All these measurements had large amplitude of voltage pulse (few milli-volts) and were performed at relatively large temperatures (typically about 1.5K or above). Also, the sample size were bigger ($\sim 1000\mu m$) as well.

In this thesis, we will present frequency resolved experiments. These measurements carry the information about the admittance of Quantum Hall device. Probing the finite frequency impedance of the Hall-bar in the sub-GHz or above regime has been done by various groups (28),(29). In these pioneering works the AC response is measured at a given frequency, which is then studied for various magnetic field. In the reference (28), the finite-frequency admittance of Hall Bar with Quantum Point contact was determined. The results were explained by the theory provided in (18),(17) which develops admittance of the Hall bar to the lowest order in frequency. However, the transport measurement done there were at frequencies lower than ours (which is in 4-8 GHz regime).

In another set of remarkable experiments presented in (11), with the usage of RF transport techniques in novel ways at $\nu = 2$, they were able to measure the charge and neutral modes separation from the single collective excitation injected in the outer-edge channel initially. This single collective excitation splits into separate charge and neutral mode owing to the strong coulomb interactions among the co-propagating edge-channels. Here S21 measurements were done ranging from 0.7 to 11 GHz. There sample was also of similar dimension than ours.

Also, in the work of Hashisaka et.al (40),(41), it was shown that since coulomb

screening in the 2D systems is weaker than in 3D, so depending upon the electrostatic environment around the edge channels (metallic gates etc.) there can be a RF coupling between edge channels lying on the opposite sides of the sample. They did the similar kind of RF transport measurements as done in (28), upto frequency of 3 GHz in a sample which was $500\mu m$ long and $100\mu m$ wide. When the QPC was pinched, the obtained S21 was modelled as coupled edge-channels across QPC, talking to each other capacitively described by a capacitance per unit length, c_X.

In all the experiments described above, the detection impedance is 50Ω. When going to lower integer filling fractions (let's say $\nu = 2$), the sample impedance increases. This results in large reflection coefficient, thereby, decreasing signal to noise ratio. So, to circumvent this problem of impedance mismatch, we fabricate on-chip microwave resonators directly connected to our electron gas. They self-resonate at about 5.5 GHz and have characteristic impedance of $1k\Omega$. An upshot of these resonators is good signal to noise ratio at large sample impedance, thereby, allowing us to do frequency resolved measurements in linear-response regime. However, this impedance matching is effective in a finite bandwidth of about 500 MHz about the resonance frequency. Hence, our measurements will be limited to this given bandwidth about the resonance. Also, we will need to calibrate the gain of RF chain and as we will see in the coming chapter, need to account for the capacitance of electron gas as well. Our sample is in mesoscopic scale with length of about $30\mu m$ and width $10\mu m$. The mixing chamber temperature at which sample lies is 15 mK and the excitation drive amplitude is in few micro-volts on chip.

We describe the RF-transport here at fixed filling factors and model the S21 based on the theory provided in Hashisaka et.al (41) and modify it catering to the need of our device. It essentially is called as plasmon scattering approach. Under this approach, plasmons generated at one contact, when going to another contact along edge channels, experience interaction. This interaction can be presented in terms of scattering of three types:

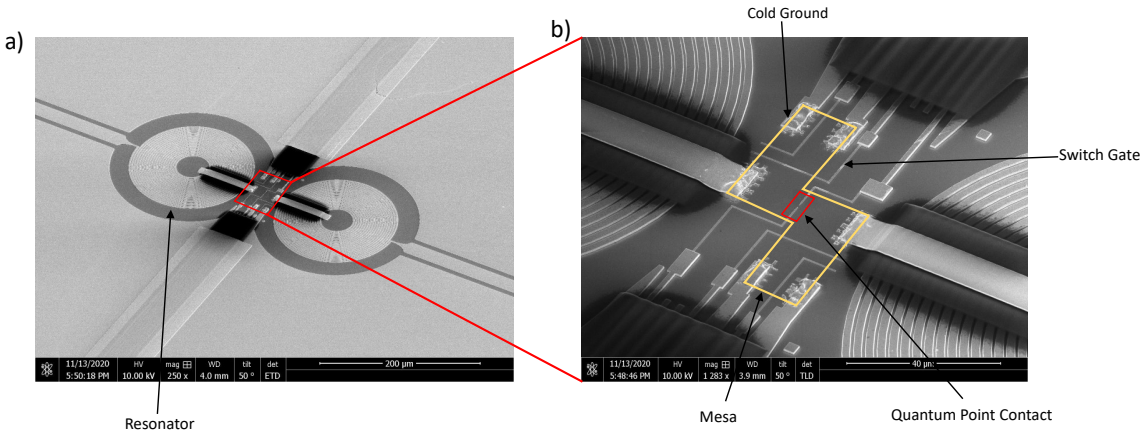

Figure 3.21: Electron Micro-graph of the device. a) Zoom-out picture showing two resonators having two-dimensional electron gas in between. All around is a continuous metallic ground plane. b) Zoom-in picture in between resonators. The yellow polygon there marks the boundary of electron gas buried 100 nm below the surface. On top of it, at the centre, is the Quantum Point Contact (shown in red). There are also switch-gates, 2 on each side, allowing to have different circuit configurations. And there is an ohmic contact on opposite edges of mesa which connects it to metallic ground plane (termed as cold grounds).

- A propagation phase acquired by travelling between two contacts
- Capacitive coupling among edge channels on opposite sides of sample due to weak coulomb screening
- When a Scattering centre is present (Like QPC), it can be additional scattering on top of the other two.

Since we have on-chip resonators attached directly to the sample, the impedance to ground, which for these resonators at resonance is about 10kΩ, is way larger than 50Ω. This mean in particular that current getting out of the sample will not be same as current getting in. For the frequency resolved experiments described above, as the samples there had 50Ω to ground, the RF transmission measurements directly yielded non-local admittance $G_{\alpha\beta}(\omega)$ of the device. In our case, we will see that Hall-Bar becomes a chiral impedance transformer and in general, we will need the knowledge of two-probe impedance, in addition to outgoing current in order to explain our measurements.

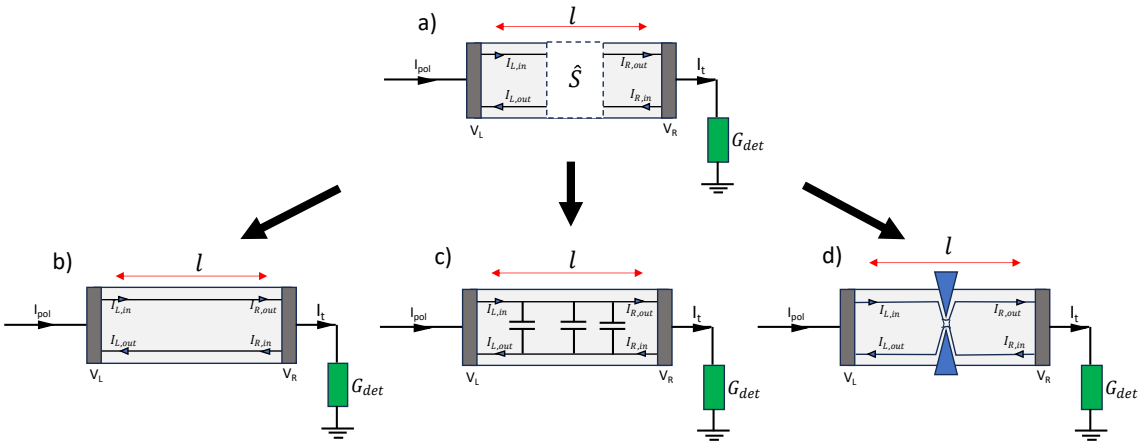

Figure 3.22: Circuit illustration for a 2DEG in Quantum Hall regime having in series with it a detection circuit with an Admittance of G_{det} which is comparable to the Hall resistance of the 2DEG. The current incident to the 2DEG at the left contact I_{pol} and the current leaving it I_t are in general not equal. a) Moreover, the plasmon interaction can be formulated in terms of a scattering matrix. b) ,c), d) describe three different cases which can be handled with scattering approach. In b) the scattering is just a phase. In c) scattering happens due to capacitive interactions among opposite edge channels and in d) QPC action can also be taken into account.

Chapter 4

AC Transport in Quantum Hall regime

4.1 Introduction

We present here RF transmission measurements of a two-dimensional electron gas which is connected on-chip microwave resonators. We send broadband frequency voltage drive (4 to 8 GHz) and measure its response. The amplitude of this ac voltage drive is about $2\mu V$, making our experimental conditions to be in linear-response regime. We will analyse this RF transmission at zero magnetic field and at finite magnetic field with or without the presence of quantum point contact.

4.1.1 Working Principle

In Microwave engineering, the components are usually characterized by scattering measurements. These measurements tell you what is the nature of the component in terms of its impedance $Z(\omega)$, insertion loss and also the directivity of signal transfer. In commercial usage, the cables used for the measurements have a definite standard impedance $Z_c = 50\Omega$. If the signal travelling through these cables encounter a device with impedance different from 50 Ω, then some of the power will be reflected back.

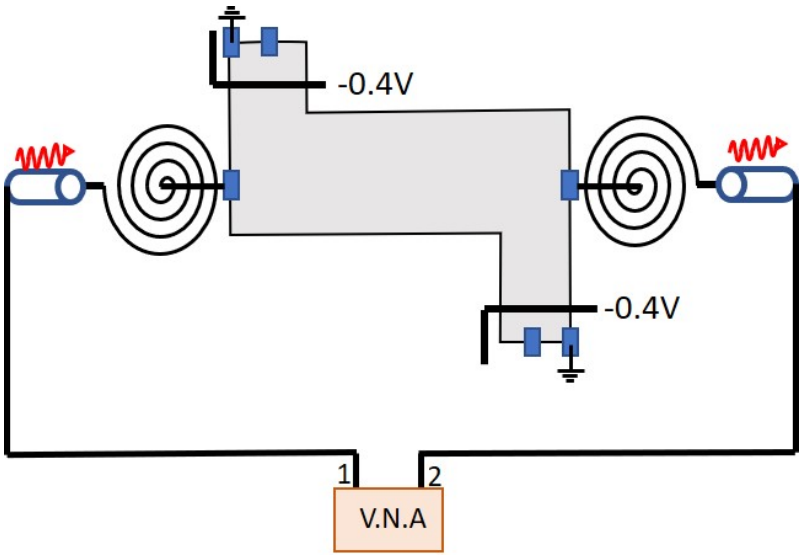

Figure 4.1: Experimental setup: Switch gates (shown in black) are biased at -0.4V to disconnect mesa from the cold grounds, making a two point configuration setup. Signal is sent from the V.N.A through port 1 and output is received at port 2, measuring S21 through the sample.

The quantity quantifying this reflected power is reflection coefficient , Γ. It is given as:

$$\Gamma(\omega) = \frac{Z_{sample}(\omega) - Z_c}{Z_{sample}(\omega) + Z_c} \tag{4.1}$$

So, some of the power is reflected and remaining gets transmitted through the device. The scattering parameter that display the information of transmitted power by measuring its ratio w.r.t input power is the **S21 parameter** (66). Formally written as:

$$S21 = \frac{P_{out}}{P_{in}} \tag{4.2}$$

A Vector Network Analyzer gives out this measurement (sketched in figure 4.1). Similar to the Reflection coefficient, it is a complex quantity with a magnitude and phase.

$$S21 = |S21|(f)e^{-i\phi(f)} \tag{4.3}$$

The curve in figure 4.4 is a measured S21 showing the behavior of the sample containing resonators in series with it.

In principle, any change made to the sample, let's say, by changing physical pa-

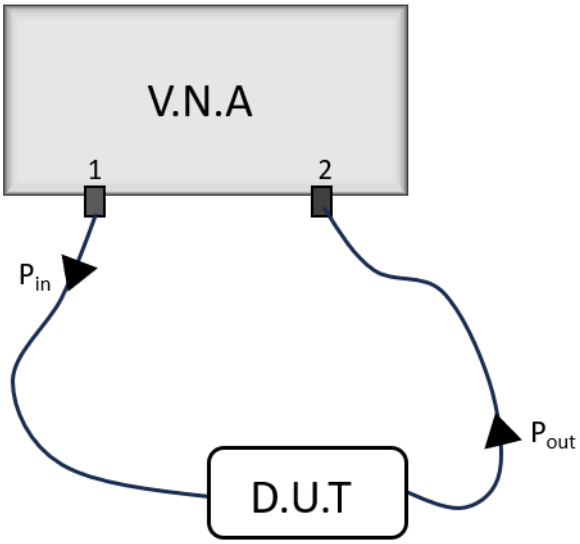

Figure 4.2: Schematic setup for S21 measurement with a **Vector Network Analyser**.

rameters (for eg, Gate voltage, Magnetic field, cold grounds etc..) will affect its ac properties (Impedance in this case), which in turn, will be visible in S21 line-shape. We, hence, perform these measurements at different physical conditions and characterize the device. Our main goal being here to know what is the Impedance $Z(\omega)$ of the Electron gas.

4.1.2 Phase Calibration

From the figure 4.2 showing the schematic setup for a S21 measurement and figure 4.3 displaying the full setup, we see that cables connecting the Vector Network Analyzer have different microwave components. These components add some phase to the S21 measurement. In the end, the total phase measured is :

$$\Phi(f) = \phi_{cable}(f) + \phi_{sample}(f) + \phi_{components}(f) \tag{4.4}$$

In order to know the device phase, we need to get rid of the phase of the connecting co-axial cables and that of the microwave components. We try to get rid of the phase due to cable length by adjusting the delay time directly on VNA. Also we

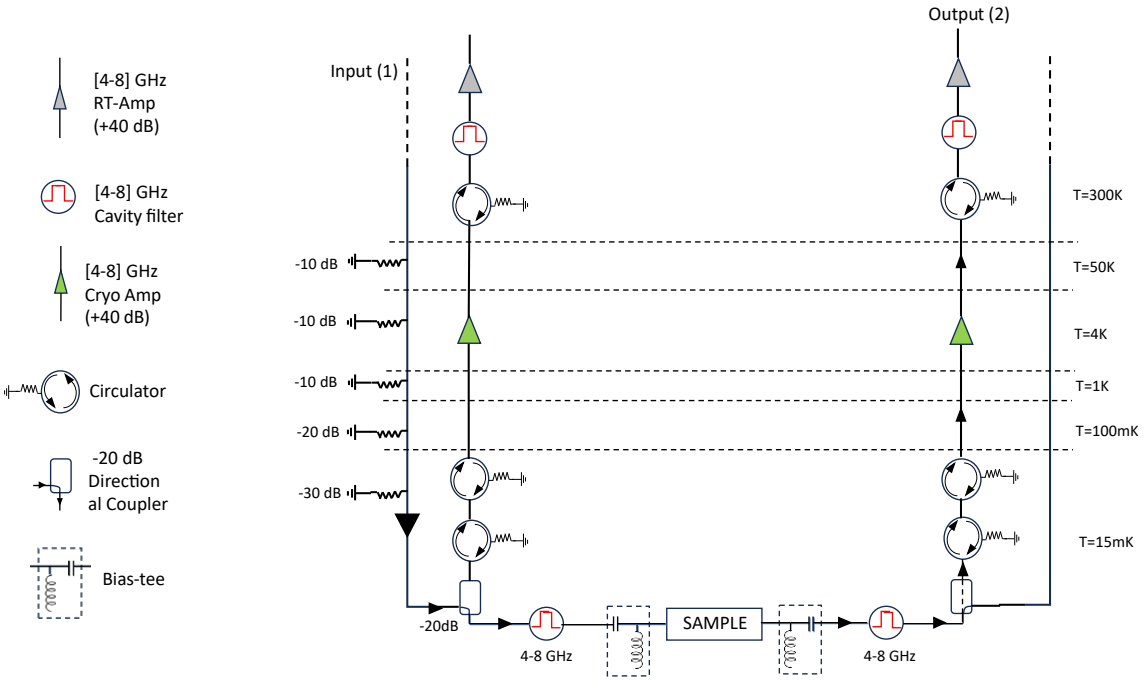

Figure 4.3: Microwave setup for the S21 measurements. Different elements are labeled accordingly. In this setup, we have two inputs (via directional couplers) and two output ports(via amplification line) for measuring S21 in different direction. In this figure, only one set is labeled.

subtract the phase of the 3 cavity filters in the detection chain. The subtraction is done by measuring the phase of the filter at room temperature and assuming that the phase changes very slightly at low temperature, so this measured phase closely resembles to that at low temperature. (See Appendix for more details)

After correction, the phase will only be that from the sample. This allows us to have the real and imaginary part of the transmission which will let us know about the impedance of sample. In figure 4.4, both amplitude and phase of S21(f) are plotted after phase calibration. In order to know about RF behavior of electron gas, we first study the RF transmission through it at zero field. As we will see below, it will help us calibrate the resonators, the overall gain of the chain and the parasitic capacitances.

4.2 Zero field Characteristics

The two-dimensional electron gas that we use has an electron density $n_e = 1.27 \times 10^{15} m^{-2}$. We give here the values of mean-free path, relaxation time from basic assumptions of the free-electron gas. Knowing the electron density, the Fermi wave-vector k_F can be found from the standard formula:

$$k_F = \sqrt{2\pi n_e} \tag{4.5}$$

Using this, we can obtain Fermi-velocity, v_F

$$v_F = \frac{\hbar k_F}{m} \tag{4.6}$$

It's value is $10^6 m s^{-1}$. The resistance of the gas R_{dc} at zero field is 300Ω. Using the standard expression for conductivity in Drude theory (61), we obtain the relaxation time as:

$$\tau_{sc} = \frac{m}{ne^2 R_{dc}} \tag{4.7}$$

It is 3 pico-seconds. Knowing the scattering time and fermi-velocity, we obtain the mean-free path $l_m = 3\mu m$. The mesa is $30\mu m$ long and $10\mu m$ wide. Comparing these dimensions with the mean free path we see that we are in between diffusive and ballistic regime. At zero magnetic field, when QPC is not active, we can write the impedance of electron gas as (12):

$$Z(\omega) = R_{dc} + i\omega L_K \tag{4.8}$$

Where, L_K is the kinetic inductance and arises due to inertial out of phase response of the charge carriers to the ac drive. For a 2D system of length L and width W, it is given as:

$$L_K = \frac{m}{n_s e^2} \frac{L}{W} \tag{4.9}$$

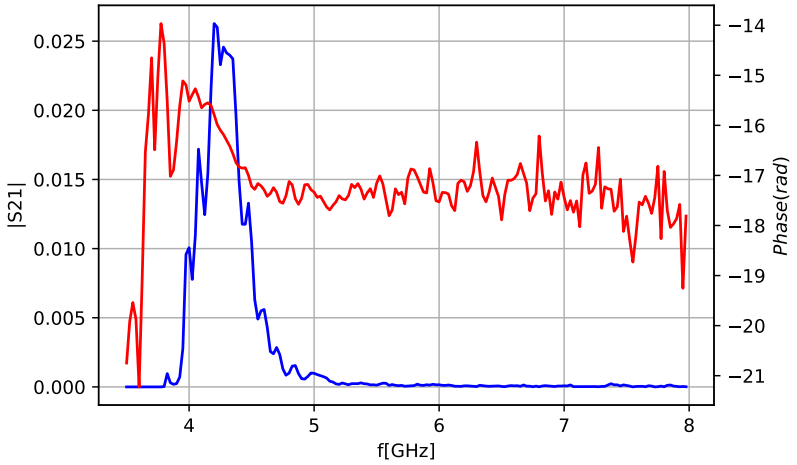

Figure 4.4: S21 resonance curve at zero magnetic field with amplitude (shown in blue) and phase (shown in red) .The shift of the curve is attributed to the additional capacitance provided by the electron gas.

This formula gives the value of kinetic inductance to be 5.7 nH.

4.2.1 Basic Features

In the figure 4.4, measurement of S21 curve is presented as a function of frequency. We see that resonance of the curve is about 4.3 GHz which is quite low as compared to self-resonance of the coil ($\simeq$ 5.5 GHz) that was simulated in SONNET software (60). We attribute this large frequency shift due to parallel addition of the mesa capacitance to the parasitic capacitance of the coil, which effectively decreases the resonance frequency f_o.

If the resonance frequency of the resonators is given as:

$$f_o = \frac{1}{2\pi\sqrt{LC}} \tag{4.10}$$

Where L and C are the bare Inductance and capacitance of each coil respectively. The addition of mesa capacitance C_m[1] modifies it as:

$$f_o^{'} = \frac{1}{2\pi\sqrt{L(C + C_m)}} \tag{4.11}$$

By knowing the resonance frequency from S21 measurement, one can extract the capacitance of electron gas to ground from the formula above. This mesa capacitance to ground along with impedance mentioned in the previous section will be useful in making minimal circuit model for electron gas in the section below.

Since, amplitude of S21 curve has some finite width, it can be used to characterise internal resistance r_{coil} of the coil that tells the loaded Q-factor of the resonator. For the case when the 2-point resistance of electron gas is low as compared to the output impedance of detection circuit (which is the case for B=0T), the Q-factor of the S21 :

$$Q_{S21} = \frac{f_o}{\Delta f_{FWHM}} \tag{4.12}$$

is the same as that of the external Q-factor of the resonator, which, in the lumped element approximation of resonator as an LCR circuit, is given as:

$$Q_{res} = \frac{Zc}{r_{coil} + 50} \tag{4.13}$$

Both resonance frequency f_o and the bandwidth Δf can be extracted from the S21 amplitude curve.

The characteristic Impedance Z_c of the resonator is given as:

$$Z_c = \sqrt{\frac{L}{C}} \tag{4.14}$$

[1]The capacitance C_m is added for one coil. Since there are two coils, this capacitance is added to each of them, thereby making the total capacitance to ground to be $2C_m$.

It is 1kΩ for the bare coil as simulated in the SONNET simulation by our group's previous PhD student Jonas Mueller (60). But, since there is an added capacitance of the mesa to the coil capacitance, this changes the characteristic impedance Z_c. By using equations 4.11 and 4.14, one arrives at a simple expression:

$$Z_c^{'} = Z_c \frac{f_o^{'}}{f_o} \tag{4.15}$$

Here $f_o = 5.5$ GHz is bare resonance frequency. Now, using:

$$Q_{S21} = Q_{res} \tag{4.16}$$

and substituting $Z_c^{'}$ from equation 4.15, we get internal resistance r_{coil} of the coils. It comes out to be 13Ω. This is in good agreement with DC resistance measurement done at room-temperature on the sample having two coils connected to each other, with R.R.R (residual resistivity ratio) of 10 measured for gold deposited similarly.

4.2.2 Lumped Element Model for S21

We can model the S21 through our device by assuming it is a Lumped element circuit. This assumption holds because at zero field, ac transport is carried by 2D-plasmons, which propagate very fast ($\sim 10^8 ms^{-1}$). It implies that propagating signal does not acquire any significant phase as it traverses the device length (which is about 30 microns in our case). The two-terminal Impedance $Z(\omega)$ of electron

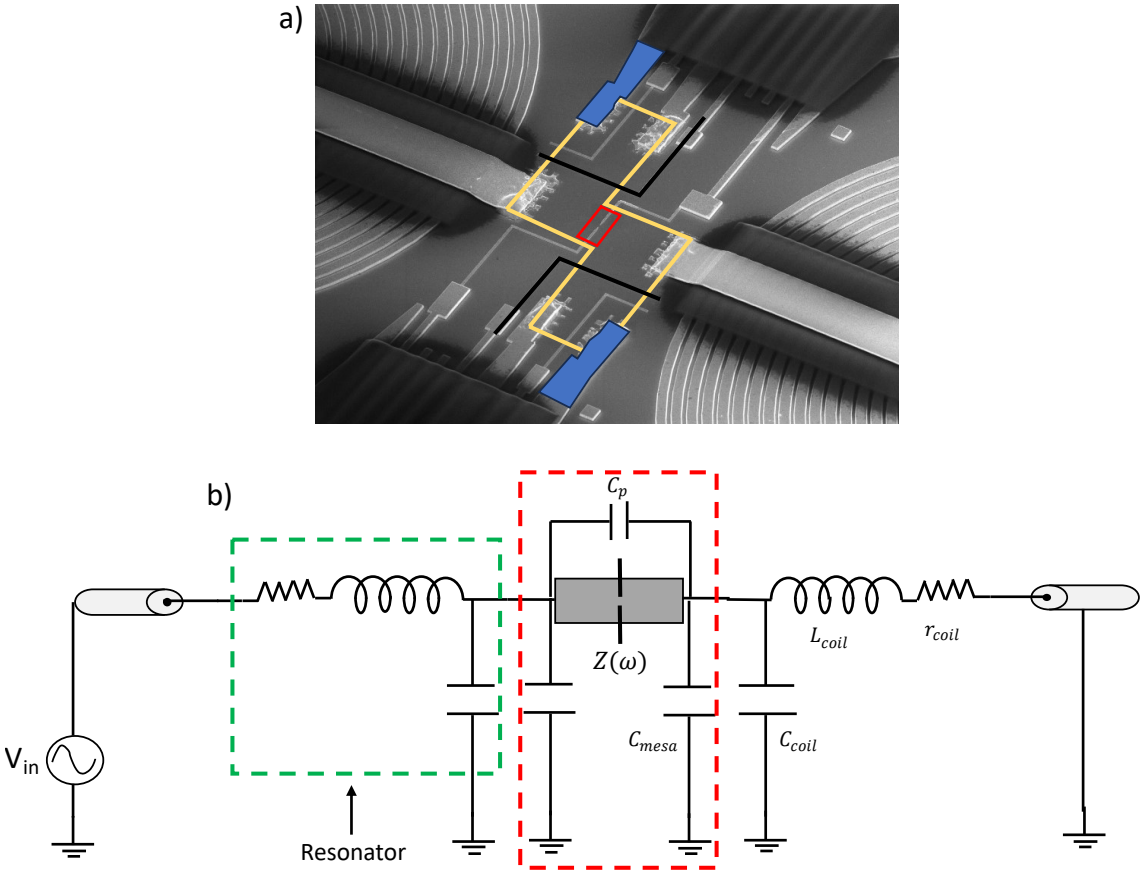

Figure 4.5: a) Electron microscope picture of the mesa in between resonators. Yellow polygon gives the boundary of electron gas beneath the surface. For the RF transmission, switch gates (shown in black) are put to use to cut the connection of electron gas to the cold grounds (shown in blue) and have a two-terminal configuration. b) Equivalent lumped element circuit model. The electron gas is modelled as a π network. There is a parasitic coupling capacitance C_p in between resonators.

gas (represented as a grey rectangle in figure 4.5) when Quantum Point contact is active can be very well approximated as that of a resistor. It is because the impedance due to kinetic inductance (L_K) at the frequencies where resonance lies

($\simeq 4.3GHz$) is very small compared to the two-terminal resistance of the Quantum Point Contact. This resistance is measured with standard lock-in techniques (it is done via inductive port of Bias-tee as drawn in the figure 4.3). Also, the electron gas has some capacitance to ground, which we name here as C_{mesa}. This adds to the resonator coil capacitance and modifies the resonant frequency.

The RF transmission here is just the ratio $\frac{V_{out}}{V_{in}}$. The amplitude of S21 will be absolute square of this ratio [2]

Let us build this S21 from the impedance of the full circuit. We explain in pieces the different impedance. Consider below the detection impedance. As seen from the

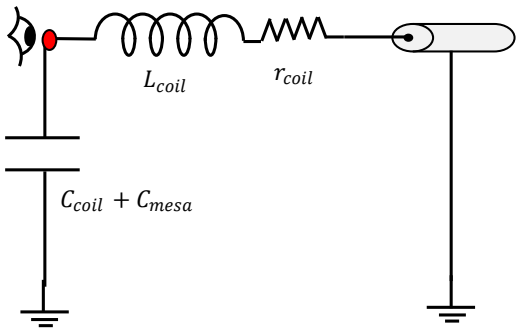

Figure 4.6: Resonator impedance as seen from the red dot to ground.

red node to the ground (figure 4.6), it is the impedance to ground as seen from the output node of the sample. It is given as:

$$Z_{det}(\omega) = \left(i\omega(C_{coil} + C_{mesa}) + \frac{1}{r_{coil} + 50 + i\omega L_{coil}} \right)^{-1} \tag{4.17}$$

To this we add two-terminal impedance of the sample , which we call as $Z(\omega)$ here in parallel with parasitic capacitance C_P. The new impedance is thus,

$$Z_1(\omega) = Z_{det}(\omega) + \frac{\frac{1}{i\omega C_P} Z(\omega)}{\frac{1}{i\omega C_P} + Z(\omega)} \tag{4.18}$$

Now, if we add remaining resonator circuit to $Z_1(\omega)$, here, capacitance gets added

[2] $|S21| = |V_{out}/V_{in}|^2$, since it is expressed as the ratio of output power obtained from device over input power applied by the source.

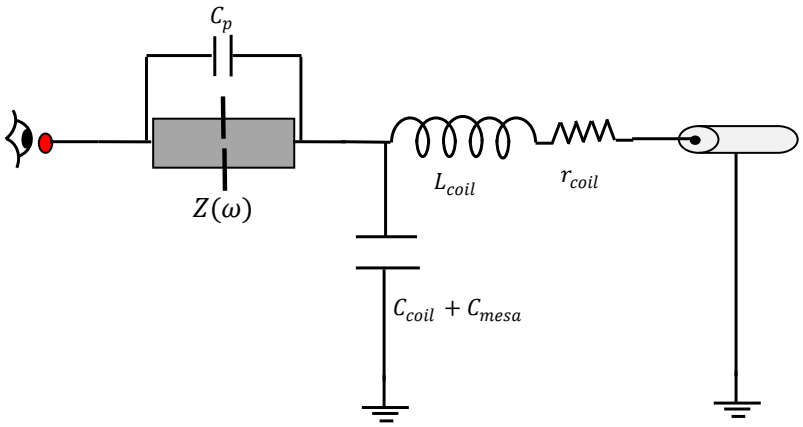

Figure 4.7: Total impedance $Z_1(\omega)$ as from the red node to the ground. $Z(\omega)$ is the two-probe resistance. C_P is the parasitic capacitive coupling

to $Z_1(\omega)$ in parallel and r_{coil} and L_{coil}, the resistance and inductor are added in series addition. The total impedance is then given as:

$$Z_{tot}(\omega) = \left(i\omega(C_{coil} + C_{mesa}) + \frac{1}{Z_1(\omega)} \right)^{-1} + r_{coil} + i\omega L_{coil} \tag{4.19}$$

As can be seen from the figure 4.8, we introduce reflection coefficient Γ at the node connecting 50 ohm line coming from the source to the total impedance $Z_{tot}(\omega)$ as seen from that node to ground. This is so because of the mismatch between these two impedances (66). Thanks to the impedance $Z_{det}(\omega)$, $Z_1(\omega)$ and $Z_{tot}(\omega)$, we can:

- deduce the voltage at the input port $V_1 = (1 + \Gamma)V_{in}$
- deduce from the successive voltage dividers the output voltage V_{out} from V_{in}

This gives us the transfer function $\frac{V_{out}}{V_{in}}$:

$$\frac{V_{out}}{V_{in}} = \frac{50 Z_{det}(\omega)(1 + \Gamma(\omega))}{(i\omega L_{coil} + r_{coil} + 50) Z_1(\omega) Z_{tot}(\omega)} \left(i\omega(C_{coil} + C_{mesa}) + \frac{1}{Z_1(\omega)} \right)^{-1} \tag{4.20}$$

We now use the formula 4.20 and study the RF-transport at zero field. The resistance of the sample is changed by the action of Quantum Point Contact. From the RF simulations of the device, the bare value of the inductance of coil is L_{coil} =29nH and that of capacitance is C_{coil} =29fF. The coils are assumed to be identical in

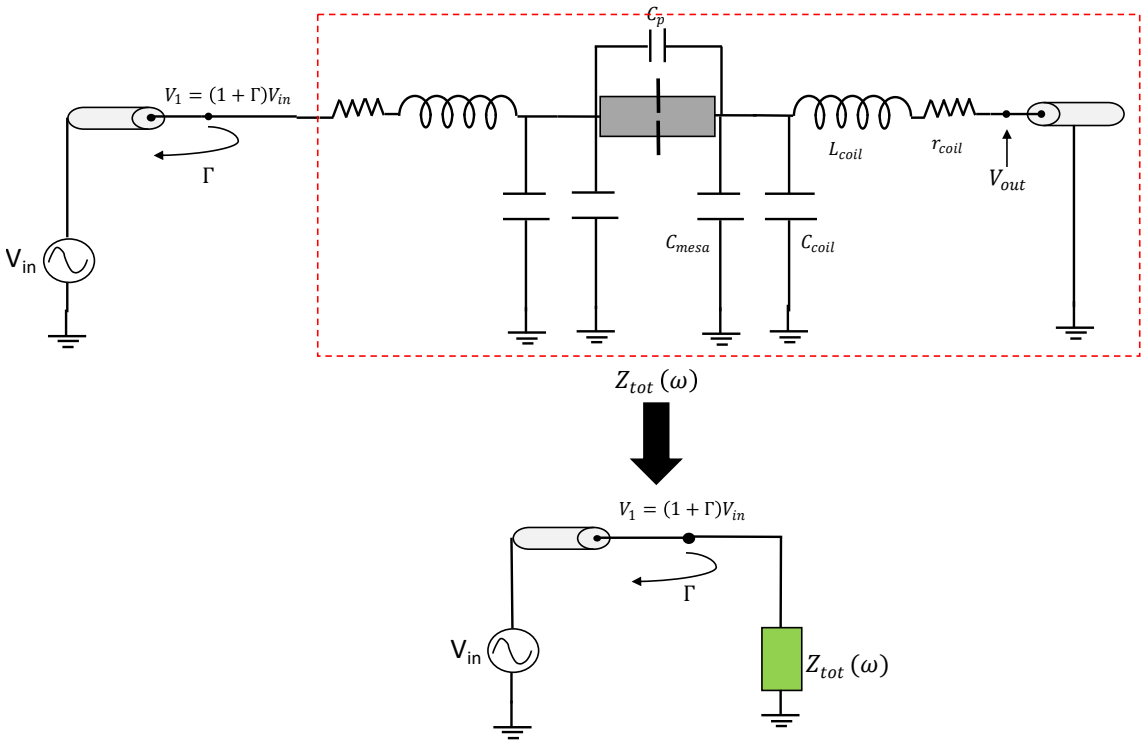

Figure 4.8: The Full circuit with total impedance $Z_{tot}(\omega)$ presented in the red-square. The equivalent circuit below which identifies the circuit with standard circuit in microwave engineering where, transmission line is shunted by an impedance (66)

the sense that they have same resonance frequency and Q-factor. As is already mentioned in the previous section, when the resistance of the electron gas is not very large (which is the case when Voltage on quantum point contact is zero), the S21 curve's full-width at half maxima is equal to that of $Re(Z_{det})$ and we can obtain the internal resistance of the coil. Also, as mentioned in the previous section, the observed resonance of S21 curve is not at simulated value, but lies far below it ($\sim$ 4.3 GHz). This is due to extra capacitance C_{mesa} of electron gas. We will use it as a fit parameter to explain the change of resonance frequency of transmission curves as a function of voltage on QPC. We now present both our DC and RF measurements where the RF measurements are fitted with the above model.

First, we present the DC two-probe conductance data in the figure 4.9. As the gate voltage on qpc gets more negative, the electron gas starts to deplete more and more (see figure 4.10). For Vqpc= -1.5V there is no DC connection, thereby, two-probe conductance drops to zero within our experimental accuracy. For each value of the

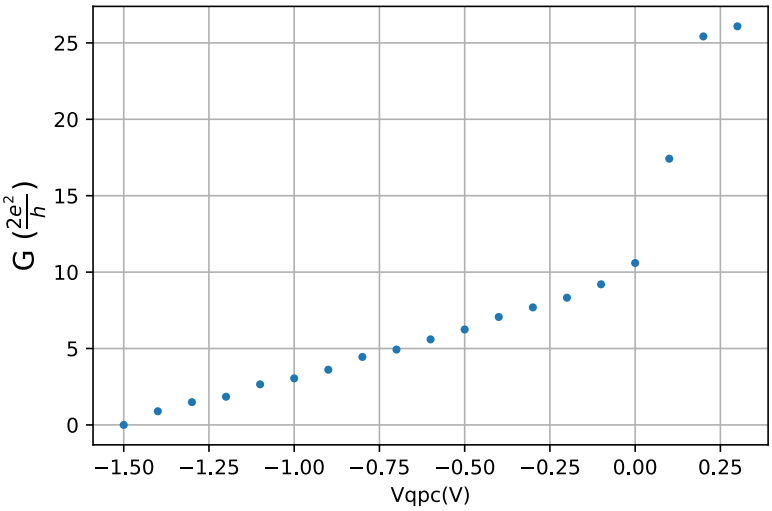

Figure 4.9: Two-probe conductance of the electron gas. The region where $0V < Vqpc < +0.3V$ is the positive offset. We do it to reduce the pinch-off gate voltage value (where there is no DC transport) so as to avoid leakage currents from gates to electron gas. In this measurement, the pinch-off voltage = -1.5 V

DC conductance, we have measured S21 trace. As we change the qpc gate voltage, changes are recorded on the S21 trace. We fit this S21 data with formula 4.20 where impedance of electron gas is two-probe DC resistance. Using that, we fit the S21 curve at +0.3 V of qpc voltage with amplitude and capacitance to ground (C_{mesa}) as two fit parameters. The amplitude obtained is equivalent to the gain of the chain and has a value of about -11.4 dB. The gain of RF chain is not changing much in the frequency interval where our S21 resonant curve lies (see appendix). After that, we extract the shunting capacitance C_P ~1.2fF from S21 fit for qpc gate voltage having no DC transport (Vqpc=-1.5V). We then fix these values in all the rest of the S21 fittings, change two-probe resistance depending upon the qpc gate voltage values (as measured in figure 4.9) and make mesa capacitance (C_{mesa}) as the single fit parameter.

4.2.3 Results and Discussion

In the figure 4.11, the curves at different qpc gate voltage values along with fits using equation 4.20 are presented. The variation of mesa capacitance with gate

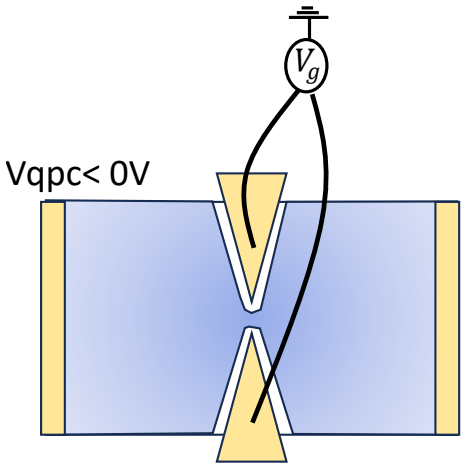

Figure 4.10: Schematic illustration of depletion of electron gas beneath qpc gates as voltage on the gates gets more and more negative. Light blue region represents 2D electron gas. White regions close to QPC gates represents the depleted region. This depletion of electron gas leads to reduction of its capacitance to ground.

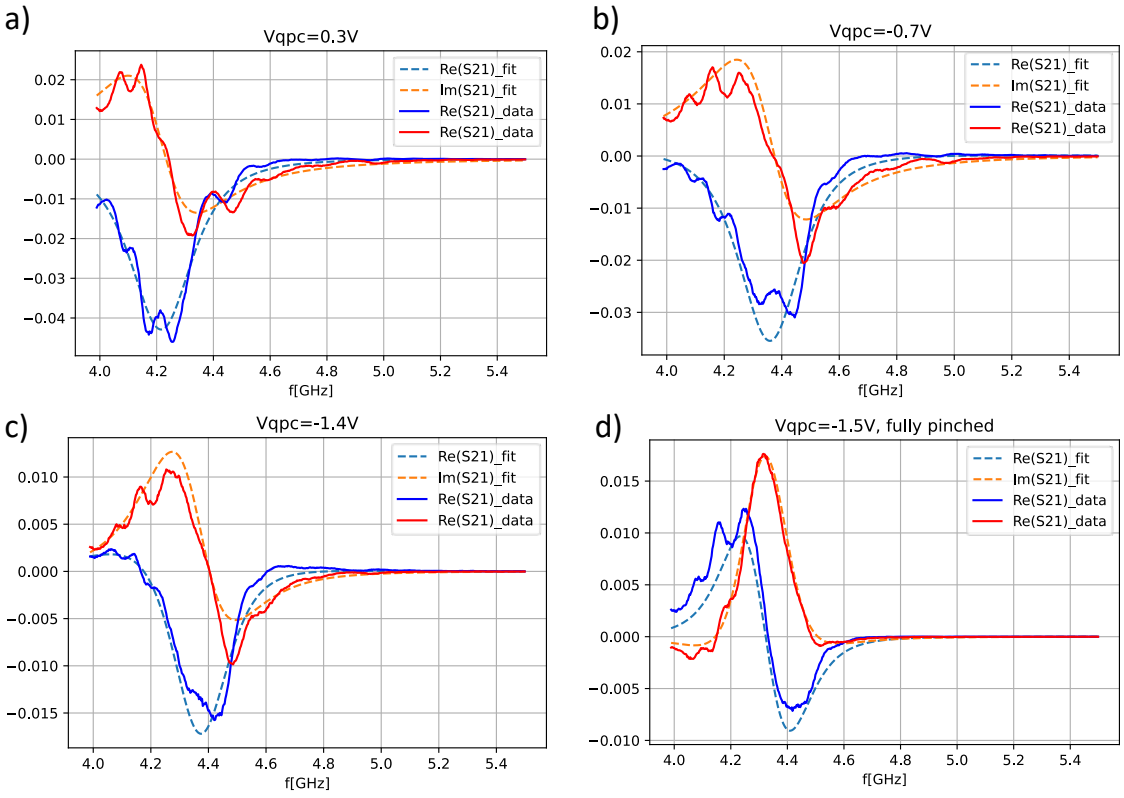

Figure 4.11: S21 curves along with fits. a), b) and c) are curves for some values of Vqpc other than pinch-off, while d) is the S21 curve at pinch-off ($G2pt \sim 0$). Note that the RF- transmission at pinch off retains the shape of the self resonance implying that it is capacitive coupling from one ohmic-contact of the mesa to the other which connect resonators with electron gas.

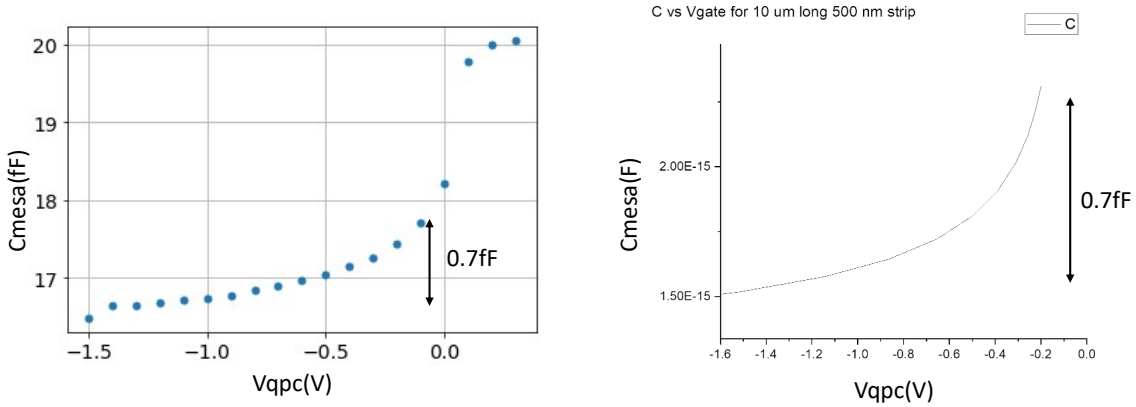

Figure 4.12: Mesa capacitance obtained from S21 fits (on the left) and from electrostatic simulation (on the right). The variation of capacitance when QPC is in action is indeed well captured, but there is a big overall offset in the capacitance obtained from fit.

voltage is presented in the figure (4.12). More Physically, this capacitance change happens as the electron gas beneath qpc gate gets depleted. This variation can be modelled by electrostatic considerations. To first approximation, one can consider a single metallic gate of length $10\mu m$ (width of our mesa) and 500 nm across, mimicking our QPC on top of electron gas. Then by numerically solving Laplace's equation one can obtain the spatial variation of electron density beneath the gates. With that, geometric capacitance to ground can be estimated as a function of gate voltage. What we find is that when qpc is in action (Vqpc $<$ 0 V), the change in the capacitance to ground as obtained from the fits is similar to the electrostatic numerical analysis. Both show decrease of capacitance of about 0.7fF. However, the capacitance to ground obtained from fits has a big offset. Now, this capacitance gets added to the resonator's capacitance and with it, we obtain the S21 line shape at proper resonance frequency. Its value being big probably means that perhaps the actual capacitance of the resonator (which we took it to 29fF) is not the simulated value. We will return to this point again while studying RF transmission for finite magnetic fields.

4.3 S21 for Finite Magnetic Field

In the previous section we showed S21 measurements at zero magnetic field and explained them using a lumped element model for the impedance of two-dimensional electron gas.

Here we present S21 measurements at each point of magnetic field as it is swept up. The sample is in two-probe setup (figure 4.13), where the ground (as seen on inductive port of bias-tee) is the body of the dilution fridge at room temperature (cold ground is not active here). Along with S21 curves, we measure the DC two-probe resistance simultaneously. Figure 4.14 presents the amplitude of S21 for few different magnetic fields.

4.3.1 2-probe setup

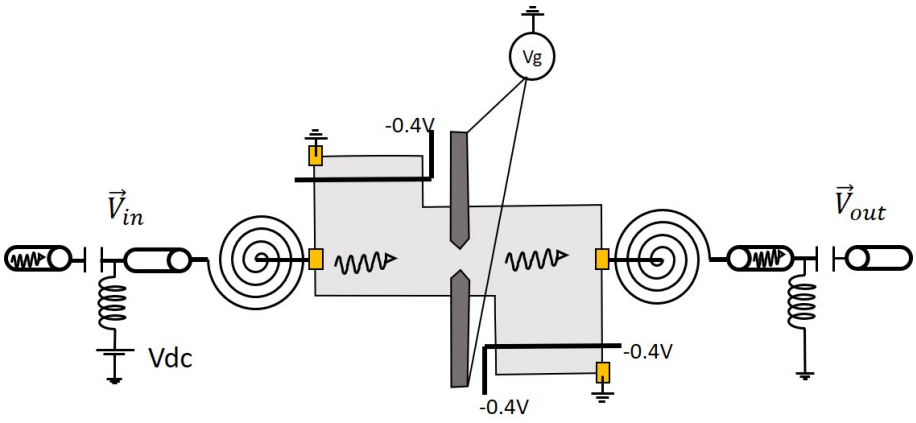

Figure 4.13: General Schematic setup for 2 point configuration vs B field. The V_{dc} is a small lock-in excitation at very low frequency that measures two point resistance vs B. Here Gate voltage Vg on Quantum Point Contact is zero. The edges of the mesa are defined partly by the switch gates and partly by chemical etching.

To analyse the S21 data vs magnetic field, we extract their resonance frequency, maximum amplitude and full width at half maxima respectively and see how they change as a function of magnetic field. These quantities are extracted by fitting a Lorentzian to the S21 amplitude curve (figure 4.15). We observe some interesting trends which can be discussed qualitatively. The maximum amplitude of S21

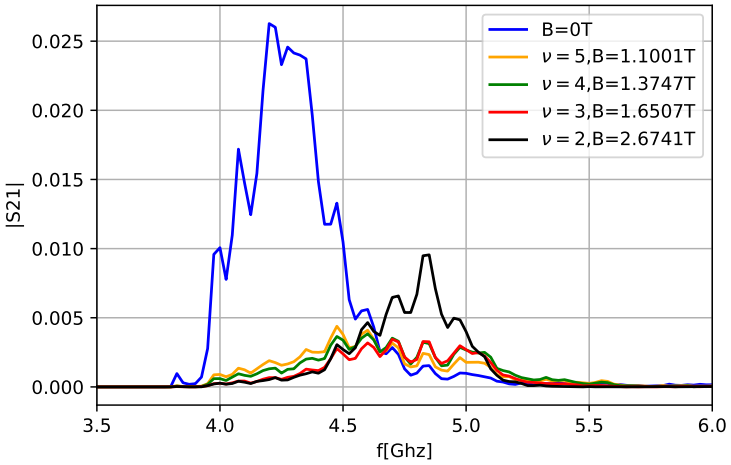

Figure 4.14: S21 vs B. Decrease in amplitude vs B and shift of resonance frequency is evident for different filling fractions. Note that the amplitude is higher for $\nu = 2$.

decreases sharply and starts to exhibit oscillations as a function of magnetic field for fields larger than 250 mT. These amplitudes are maximum at approximately the middle of Hall plateaus for all the filling fractions that are observable in D.C upto $\nu = 2$. They are not constant along the hall plateau where two-probe resistance is constant (equal to hall resistance). So, we observe no quantisation for RF transmission. The resonance frequency starts to shift larger values, hitting the maximum at filling fraction $\nu = 2$. The width also increases upto the field for which at D.C we are in filling fraction $\nu = 4$ and then it decreases. Both frequency and width show smooth oscillations as well. All these changes are due to change in the impedance of the electron gas. We will try to explain these features of RF transmission at integer filling fraction with the plasmon scattering approach introduced in the first chapter.

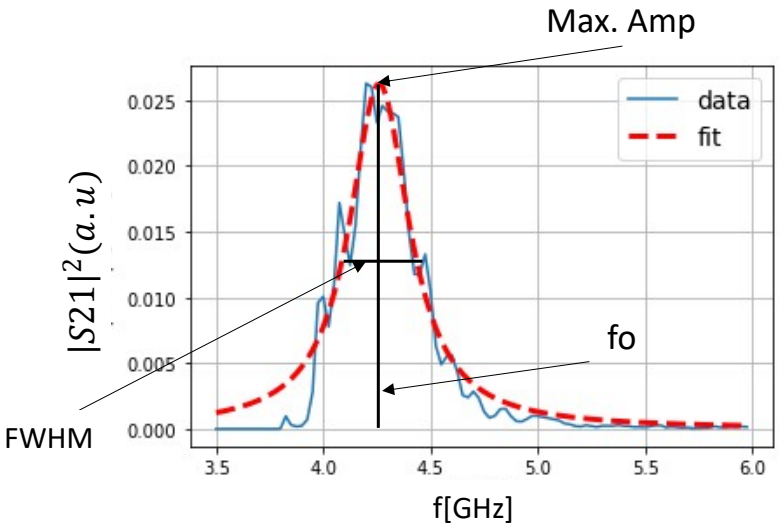

Figure 4.15: Lorentzian fit to S21 curve to extract maximum amplitude, resonance frequency and width

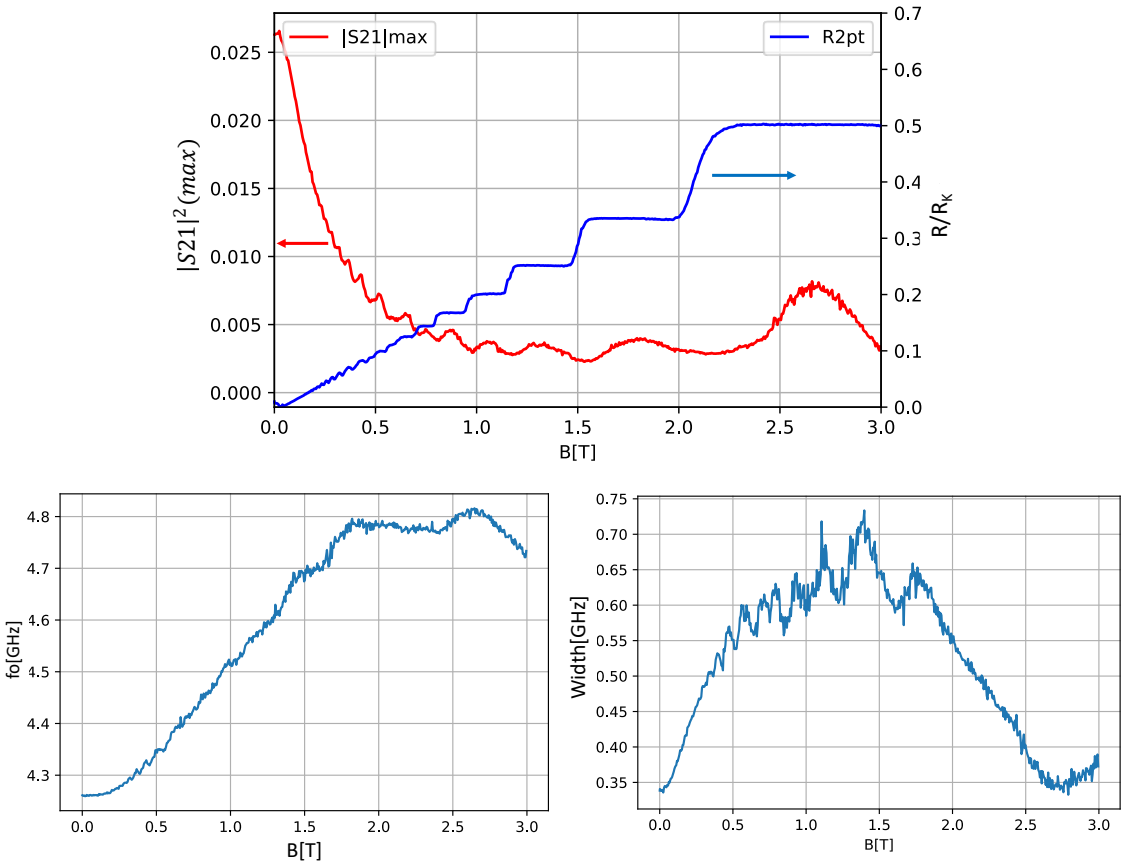

Figure 4.16: Magnitude, resonance frequency and width of S21 as a function of Magnetic field B. The trends are given till $\nu = 2$

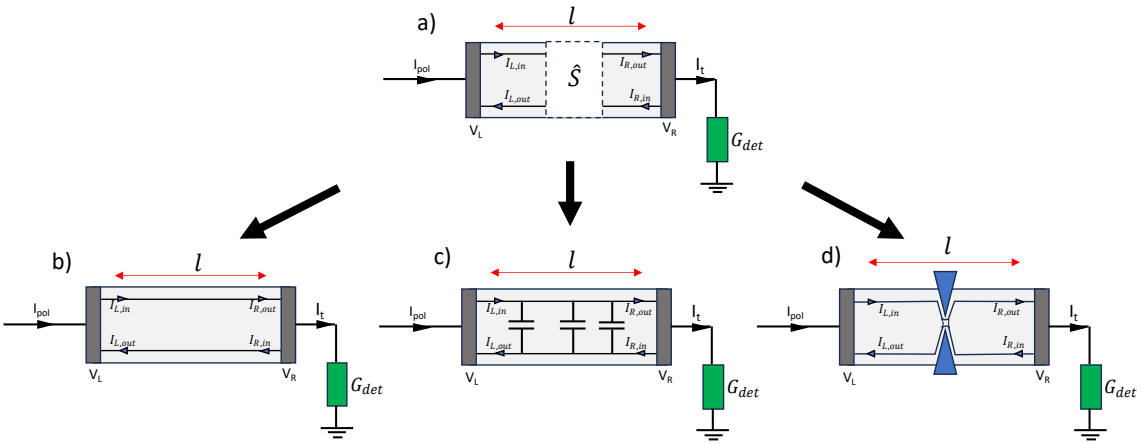

Figure 4.17: Circuit illustration for a 2DEG in Quantum Hall regime having in series with it a detection circuit with an Admittance of G_{det} which is comparable to the Hall resistance of the 2DEG. The current incident to the 2DEG at the left contact I_{pol} and the current leaving it I_t are in general not equal. a) Moreover, the plasmon interaction can be formulated in terms of a scattering matrix. b) ,c), d) describe three different cases which can be handled with scattering approach. In b) the scattering is just a phase. In c) scattering happens due to capacitive interactions among opposite edge channels and in d) QPC action can also be taken into account.

Consider the circuit in figure (4.17a). We consider the sample to be in integer quantum hall plateau. The sample is injected with a current I_{pol}. This is an AC current that excites the edge-plasmons in the sample which then travels from the left contact to the right one. We follow the approach mentioned in (40) and model an edge-channel as a unidirectional transmission line. The excess charge distribution $\rho(x,t)$ that happens after the application of ac-drive is related to the voltage $V(x,t)$ at position x on the edge-channel by the relation:

$$\rho(x,t) = C_H V(x,t) \tag{4.21}$$

where C_H is the channel capacitance, representing effective electrochemical capacitance (17) between the channel and the ground. The current $I(x,t)$ is related with the excess density via the continuity equation as:

$$\frac{\partial I}{\partial x} = -\frac{\partial \rho}{\partial t} \tag{4.22}$$

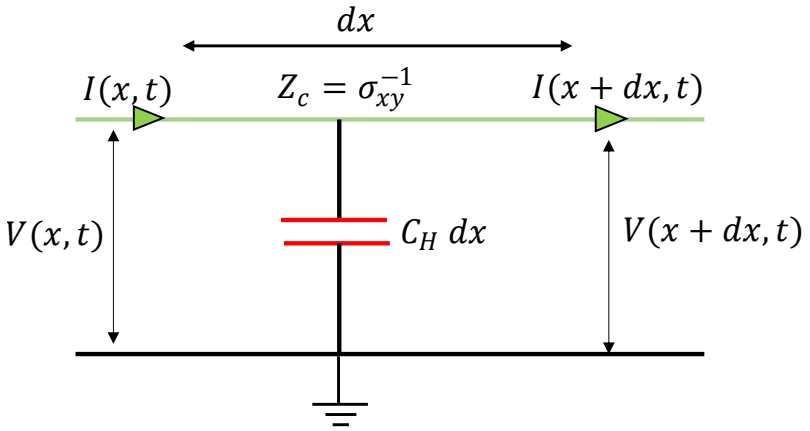

Figure 4.18: A Uni-directional transmission line model for Edge-magnetoplasmons in Edge-channels in integer filling fraction. The edge channel are characterised with a characteristic impedance as Hall resistance and capacitance per unit length to ground as an electrochemical capacitance C_H

we assume that $I(x,t)$ and $V(x,t)$ satisfy the constitutive relation as:

$$I(x,t) = \sigma_{xy} V(x,t) \tag{4.23}$$

This implies that one can think of edge channel as a chiral transmission line with characteristic impedance as $Z = V/I = 1/\sigma_{xy}$. From the above relations, we obtain the wave-equation for edge magnetoplasmons as:

$$\frac{\partial I(x,t)}{\partial t} = -\frac{\sigma_{xy}}{C_H}\frac{\partial I(x,t)}{\partial x} \tag{4.24}$$

This first-order P.D.E has a general solution of the form $I(x - v_{emp}t)$, where plasmon velocity is given as:

$$v_{emp} = \frac{\sigma_{xy}}{C_H} \tag{4.25}$$

The plasmon propagation is seen as an EM perturbation (current, density, voltage) propagating along the edge-channel. Now, we describe any interaction that happens in the sample as a plasmon scattering matrix **S**. This matrix can just consist of phases when capacitive interactions among edge states is weak, otherwise, it can describe full interactions when capacitance among edge states is present, with or

without Quantum Point Contact, with scattering parameters that are derived in (40). To that formalism, the modification that we do is to introduce the Detection impedance in series with our electron gas. Let's say that we have integer filling fraction $\nu = N$. We write constitutive hall relations at left and right contacts for ith edge channel.

$$\begin{aligned} I^i_{L,in} &= G_k V_L \\ I^i_{R,in} &= G_k V_R \\ I_{L,in} &= \sum_{i=1}^{N} I^i_{L,in} = N G_k V_L \\ I_{R,in} &= \sum_{i=1}^{N} I^i_{R,in} = N G_k V_R \end{aligned} \tag{4.26}$$

And also the current conservation equations at the contacts.

$$\begin{aligned} I_{pol} &= \sum_{i=1}^{N} (I^i_{L,in} - I^i_{L,out}) \\ I_t &= \sum_{i=1}^{N} (I^i_{R,out} - I^i_{R,in}) \\ I_t &= V_R G_{det} \end{aligned} \tag{4.27}$$

Here G_k is the quantum of conductance and G_{det} is detection admittance. Now, we use scattering matrix for each edge-channel to relate outgoing currents with input currents.

$$\begin{aligned} I_{L,out} &= \sum_{i=1}^{N} I^i_{L,out} = \sum_{i=1}^{N} (s^i_{11} I^i_{L,in} + s^i_{12} I^i_{R,in}) \\ I_{R,out} &= \sum_{i=1}^{N} I^i_{R,out} = \sum_{i=1}^{N} (s^i_{21} I^i_{L,in} + s^i_{22} I^i_{R,in}) \end{aligned} \tag{4.28}$$

Using 4.26 and 4.27 in 4.28, we obtain the relation between V_L and V_R:

$$V_R(\omega) = V_L(\omega)\frac{\sum_{i=1}^{N} s_{21}^i G_k}{\left(G_{det} + \sum_{i=1}^{N}(1 - s_{22}^i)G_k\right)} \tag{4.29}$$

Substituting this relation into 4.27 for I_{pol} we obtain two-probe impedance of the device as seen from the left contact.

$$\frac{V_L}{I_{pol}} = Z_{2pt}(\omega) = \frac{R_k}{\left(\sum_{i=1}^{N}(1 - s_{11}^i) - \frac{(\sum_{i=1}^{N} s_{12}^i)(\sum_{j=1}^{N} s_{21}^j)}{\left(\sum_{j=1}^{N}(1-s_{22}^j)\right)+\frac{R_k}{Z_{det}}}\right)} \tag{4.30}$$

Here Z_{det} is the impedance of the detection circuit (it is inverse of admittance G_{det}) from the rightmost node connected to sample in figure 4.17. The transconductance is obtained as :

$$G_T(\omega) = \frac{I_t}{V_L} = \frac{\sum_{i=1}^{N} s_{21}^i G_k}{\left(\left(\sum_{i=1}^{N}(1 - s_{22}^i)\right)\frac{G_k}{G_{det}} + 1\right)} \tag{4.31}$$

Relating the incoming voltage carried by the current I_{in} at the input of the coil at the left contact of the sample to that at the output of the sample coupled to detection line at the right contact as shown in figure 4.17, and knowing the two-probe impedance to ground from the left contact, we can build the full transfer function of our device at finite magnetic field. The transfer function 4.20,becomes:

$$T(\omega) = \frac{50(1 + \Gamma(\omega))(Z_c(\omega)Z_{2pt}(\omega))}{(i\omega L_{coil} + r_{coil} + 50)(Z_c(\omega) + Z_{2pt}(\omega))Z_{tot}(\omega)} G_T(\omega) \tag{4.32}$$

We now use this formalism to explain our RF-transmission measurements in Integer Quantum Hall regime. The data is related to figure 4.16 where no QPC is used. In this case, we assume that the scattering matrix for each edge channel is just a phase

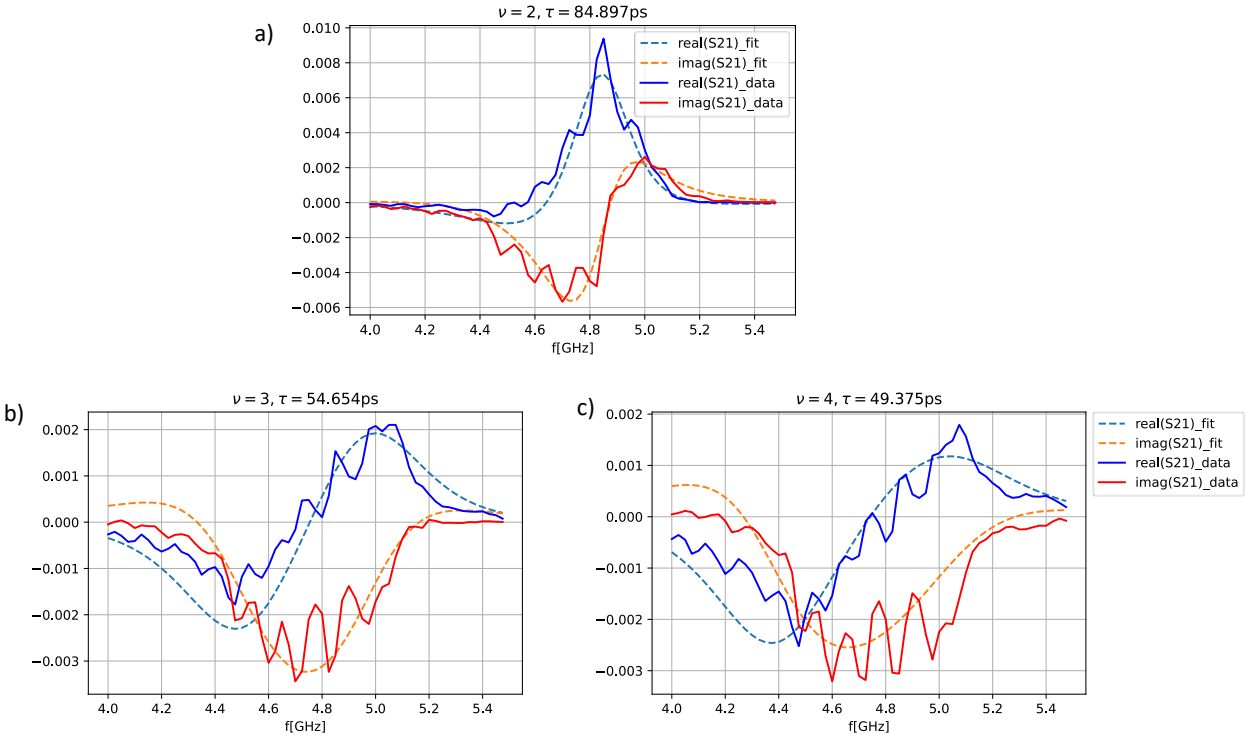

Figure 4.19: S21 curves for $\nu = 2, 3$ and 4 along with fits with transfer function given in 4.32 having scattering matrix as given in 4.33. The obtained τ are 84.9 ps, 54.65 ps and 49.375 ps respectively, The mesa capacitance obtained for three of the curves is 9.62fF, 9.67fF and 9.7fF respectively.

factor owing to the propagation in the sample.

$$\hat{S} = \begin{bmatrix} 0 & e^{-i\beta L} \\ e^{-i\beta L} & 0 \end{bmatrix} \tag{4.33}$$

$$\beta L = \omega\tau \tag{4.34}$$

Using this scattering matrix in the expressions for Z_{2pt}, V_R and I_t, we get relatively simple forms for input impedance and trans-conductance:

$$V_R = V_L \frac{e^{-i\beta L}}{\left(1 + \frac{R_H}{Z_{det}}\right)} \tag{4.35}$$

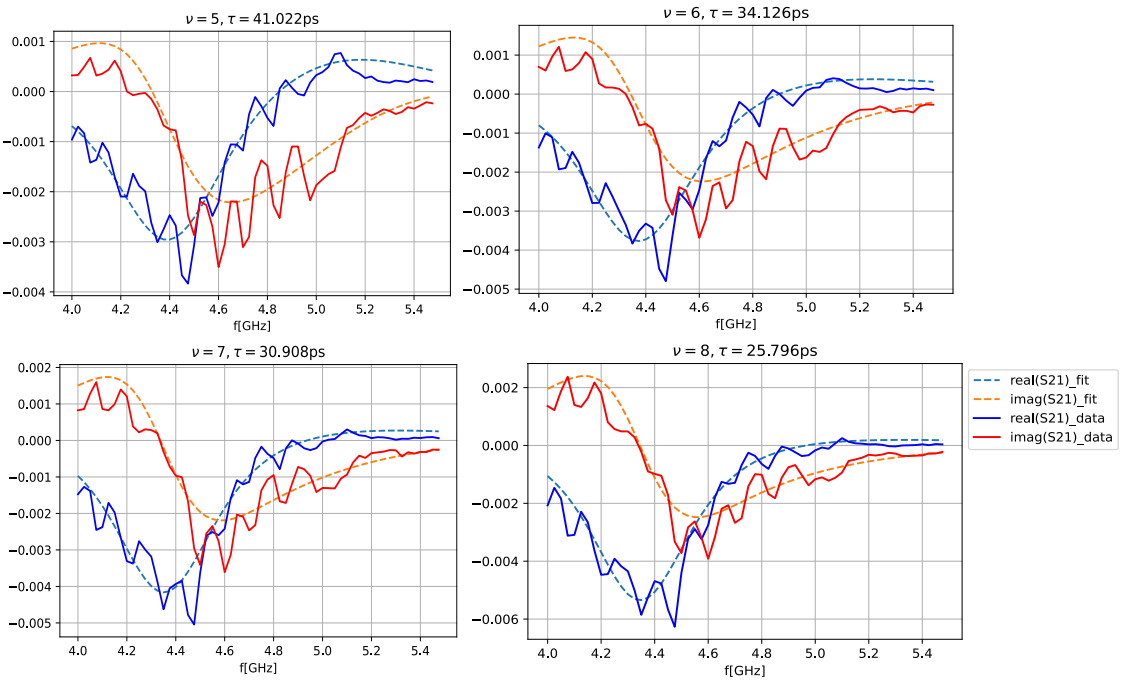

Figure 4.20: More data of S21 along with fits for filling factor of 5,6,7 and 8.

$$Z_{2pt} = \frac{R_H}{\left(1 - \frac{e^{-i2\beta L}}{1+\frac{R_H}{Z_{det}}}\right)} \tag{4.36}$$

$$\frac{I_t}{V_L} = \frac{e^{-i\beta L} G_H}{\left(1 + \frac{G_H}{G_{det}}\right)} \tag{4.37}$$

The phase factor βL in the scattering matrix can be converted into $\omega\tau$ by assuming linear dispersion relation of chiral plasmons propagating in edge-channel (40; 49). The τ is the traversal time of the plasmon in the sample. By making this time as a fit parameter along with some extra capacitance (to align the curve at right frequency) we obtain the fits at integer filling fraction from 2 to 8 (figure 4.19, 4.20). Plotting the fit parameters (dwell time and extra capacitance) with filling factor, we see their dependence (figure 4.21). From the fits we see that dwell time decreases while increasing filling factor, meaning:

$$v_{emp} \propto \sigma_{xy} \tag{4.38}$$

Taking the length of edge channel to be $30\mu m$, we can obtain the dependence of

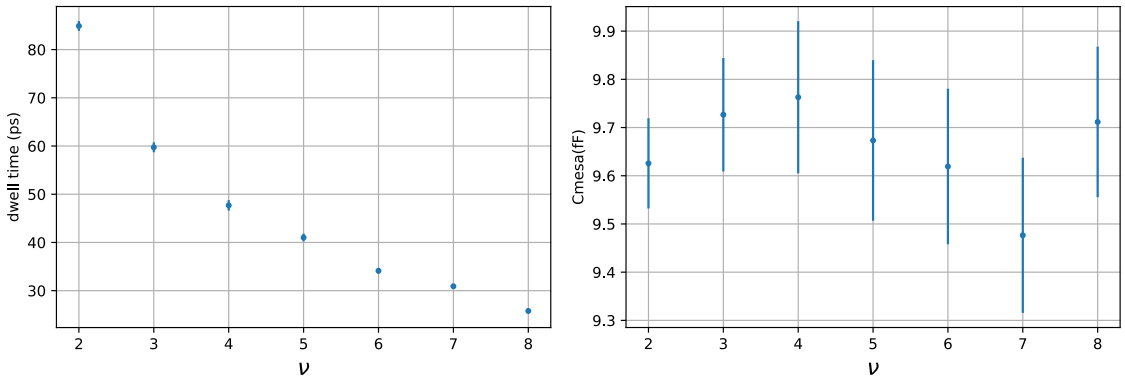

Figure 4.21: Dependence of Dwell time and extra capacitance with filling factor. Notice that extra capacitance is constant within error bars. It does not depends upon magnetic field.

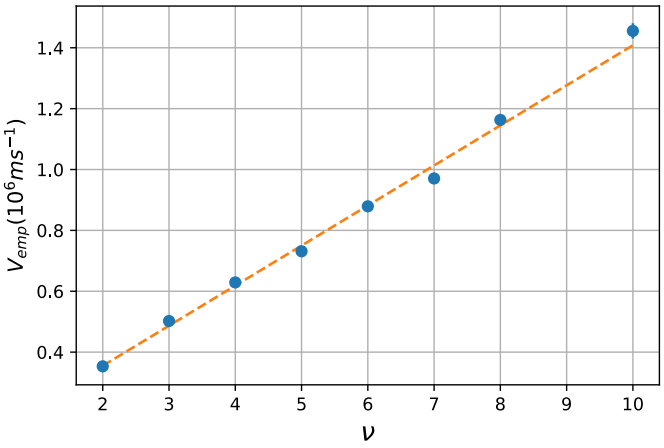

Figure 4.22: Velocity vs filling factor.

plasmon velocity with filling factor (see figure 4.22). These observations have been seen in (49). Also, the extra capacitance obtained is not different for these filling factors, which makes sense as the change in geometric capacitance is small for few edge channels. This capacitance is most likely the additional capacitance of each resonator that comes during their fabrication.

The simple propagation model for Edge-magnetoplasmons at integer Quantum Hall regime explains our data for RF transport at integer filling factor. In particular, the equation 4.36 conveys that the electron gas in the quantum hall regime behaves as an impedance transformer. This property is similar to transmission lines acting as quarter-wave transformers (66). This impedance transformation depends upon the

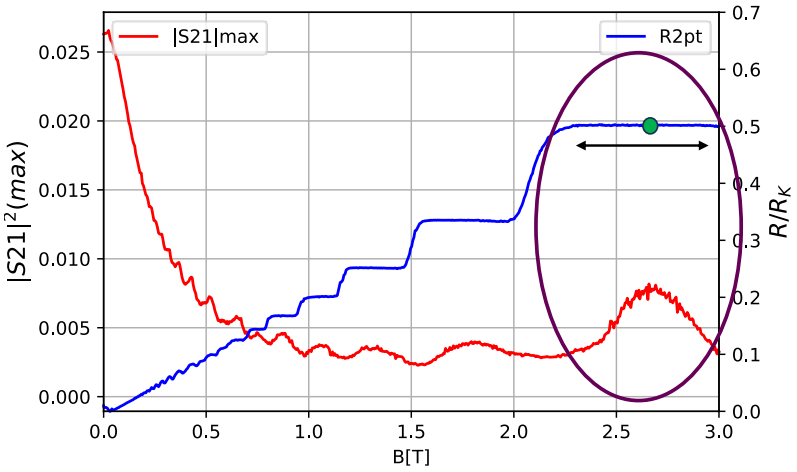

Figure 4.23: For magnetic field across any integer plateau (here $\nu = 2$ is highlighted in particular), $|S21|$ max. amplitude shows non-monotonous behavior.

load impedance (Z_{det}), hall resistance, length of sample and velocity of propagation. The behavior of S21 curves for different integer filling fraction typically depends upon load impedance and length of the sample. The results will be different had we had a sample of different length or a different profile of load impedance. What is most striking implication of the eq. 4.36 is that if the load is a short, then no matter what is the length of the device, the two-probe impedance of electron gas at these frequencies is hall resistance. It is assumed here that there is no longitudinal resistance. However, we are able to explain S21 curves at magnetic fields where longitudinal resistance does not fully vanish (for integer ν = 7,8 and 10). This means that edge excitations are not scattered, are localised strongly along the edges and go uninterrupted from one contact to other. This observation rhymes with theoretical findings of Volkov and Mikhailov (78).

4.3.2 Non-Monotonous S21 trend across $\nu = 2$ Plateau

In the previous section, we saw that at integer filling fraction, we can explain our S21 line shapes by a lossless transmission line model for edge-magnetoplasmons. From the figure 4.23, we observe that at quantum Hall plateau, the RF transmission is

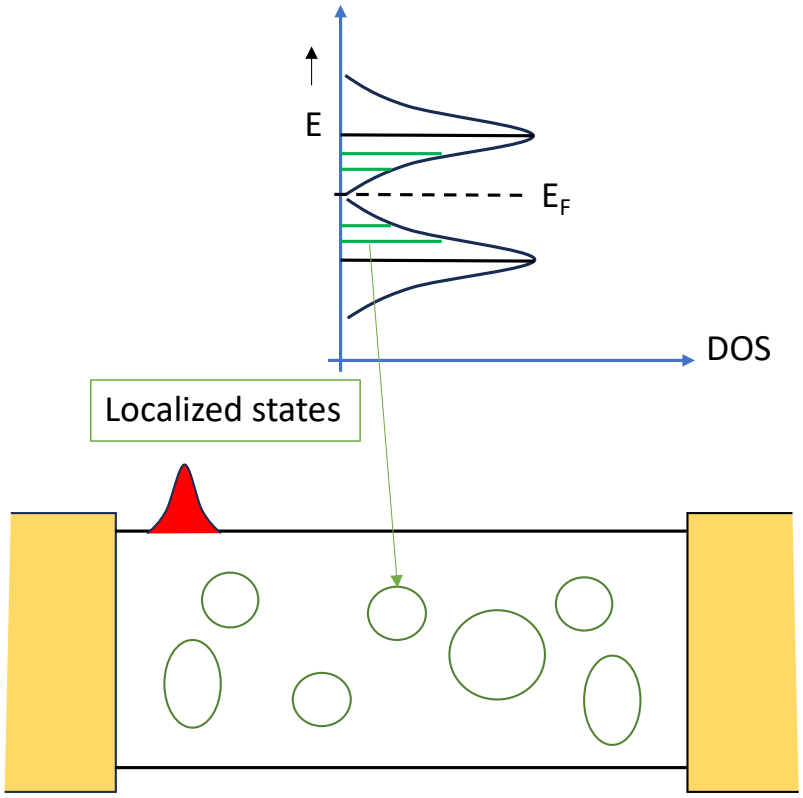

Figure 4.24: Schematic illustration of edge plasmons (shown as red pulse) with localised states. The coupling of plasmons with localised states leads to losses.

maximum at the centre of the plateau but decreases as one moves away from it on either sides. We think that this decrease in S21 amplitude is caused due to the coupling of edge plasmons with localised states in the bulk. Now, localised states exists in the bulk due to disorder (33),(67), (68), (52), (39). Due to them, the quantum hall plateau is stabilised (figure 4.24). As one is moving away from the centre the coupling to these localised states increases, thereby, increasing signal losses. We explain here our S21 line shapes across $\nu = 2$ plateau by considering in a phenomenological manner, the coupling to the bulk.

4.3.3 Resistive coupling to Bulk

In the figure 4.25, we have presented Edge channel as a transmission line with characteristic impedance as Hall resistance and capacitance to ground as electrochemical capactance C_H per unit length. In addition, there is a conductance per unit length

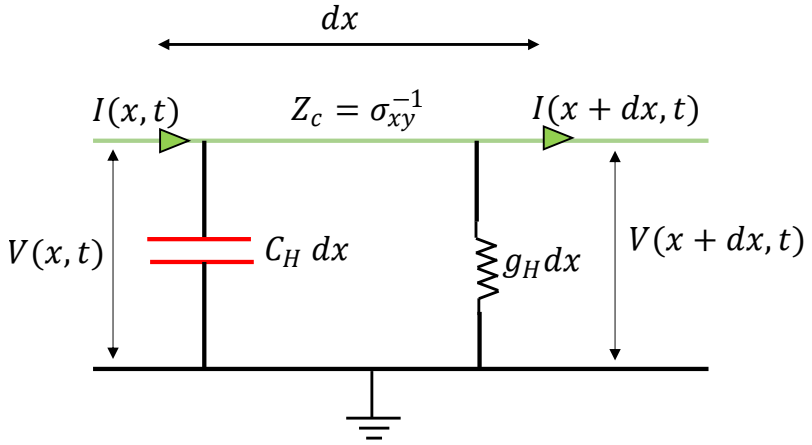

Figure 4.25: Edge magnetoplasmon model showing ohmic dissipation given by a conductance per unit length

g_H that accounts for the ohmic dissipation. This model leads to the following differential equation for the current wave $I(x,t)$:

$$\frac{\partial I(x,t)}{\partial t} = -\frac{\sigma_{xy}}{C_H}\frac{\partial I(x,t)}{\partial x} - \frac{g_H}{C_H}I(x,t) \tag{4.39}$$

With an ansatz of the form $I(\beta,\omega)e^{i(\beta x-\omega t)}$, we obtain the complex dispersion relation as:

$$\tilde{\omega} = \frac{\sigma_{xy}}{C_H}\beta - i\frac{g_H}{C_H} \tag{4.40}$$

This means that for an edge-magnetoplasmon excitation to go from one contact to another, it will not only have a propagation phase, but will also be attenuated exponentially. Incorporating these changes in equations 4.35 and 4.36, we obtain the following expression:

$$V_R(\tilde{\omega}) = V_L(\tilde{\omega})\frac{e^{-i\tilde{\omega}\tau}}{\left(1+\frac{R_H}{Z_{det}}\right)} \tag{4.41}$$

$$Z_{2pt}(\tilde{\omega}) = \frac{R_H}{\left(1-\frac{e^{-i2\tilde{\omega}\tau}}{1+\frac{R_H}{Z_{det}}}\right)} \tag{4.42}$$

Here τ is still the traversal time of the plasmons. In this model, the conductance per unit length g_H will be dependent on the magnetic field spanning the size of the

Hall plateau, becoming larger at values away from the centre of hall plateau. We

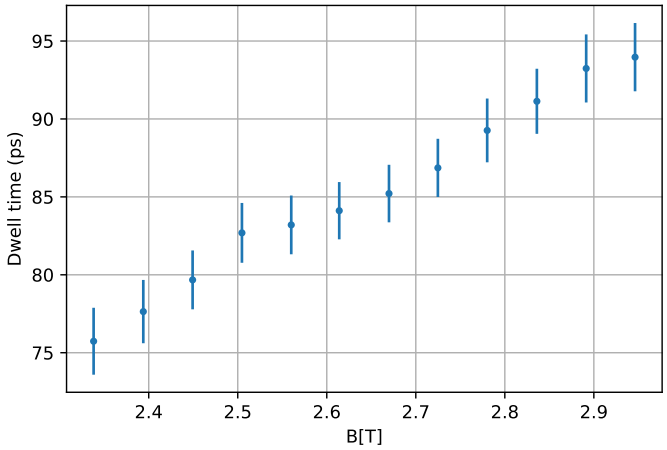

Figure 4.26: Dwell time dependence on the magnetic field spanning $\nu = 2$ Hall plateau.

now use the equations 4.41 and 4.42 in our Transfer function formula 4.32 and use it to fit our S21 data spanning $\nu = 2$ plateau. The fit parameters here are the dwell time τ, some extra capacitance to ground (C_{extra}) and the dissipation factor $\frac{g_H}{\sigma_{xy}}$. The figures 4.26, 4.27 and 4.28 are the results of the fit. The dwell time increases with the magnetic field. From this and also knowing that our 2DEG is $30\mu m$ long, we can extract the velocity of edge-plasmons. From the dissipation factor we obtain conductance per unit length. That's what is plotted in figure 4.27. The S21 line shapes along with fitted real and imaginary parts obtained from the above model are presented in figure 4.29

By assuming a frequency independent ohmic dissipation, we have been able to explain the S21 line shapes in a phenomenological manner across $\nu = 2$ plateau. The obtained conductance per unit length gives us the DC resistance to ground to be in 100's of kilo-ohms. We know that these values are false, since these must have been seen in our two-probe DC resistance measurements.

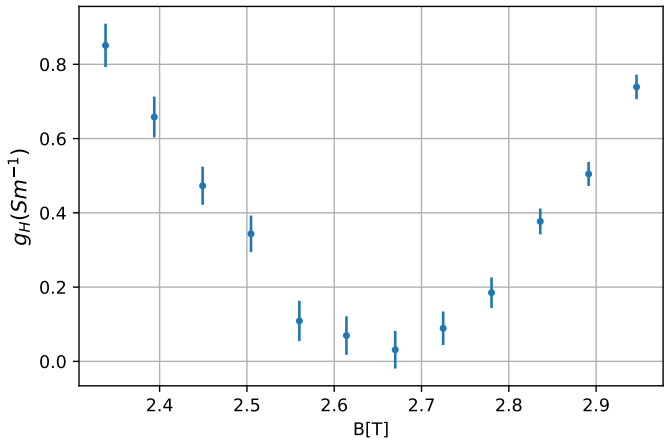

Figure 4.27: Conductance per unit length in Sm^{-1} as a function of magnetic field.

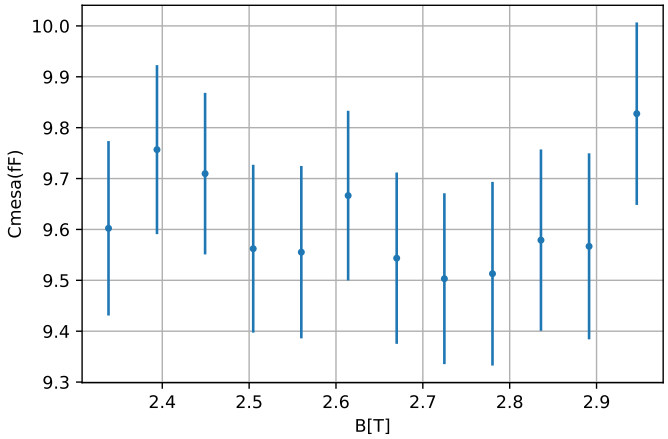

Figure 4.28: Mesa capacitance variation with changing magnetic field across the Hall plateau

4.3.4 RC coupling to the Bulk

We now use another coupling of edge plasmons with the bulk localised states. It is of the form of a RC circuit. Physically, this means that the edge plasmons are capacitively coupled with bulk localised states. Due to this, there is leakage of signal, which then gets dissipated in those states. This description of RF transport can again be given in terms of dissipative transmission line minimal model (figure 4.30), where C_l and R_l are the loss capacitance per unit length and resistor per unit length respectively. With this model, the equation 4.22 is replaced by,

$$\frac{\partial I}{\partial x} = -\frac{\partial(\rho_{C_H} + \rho_{C_l})}{\partial t} \tag{4.43}$$

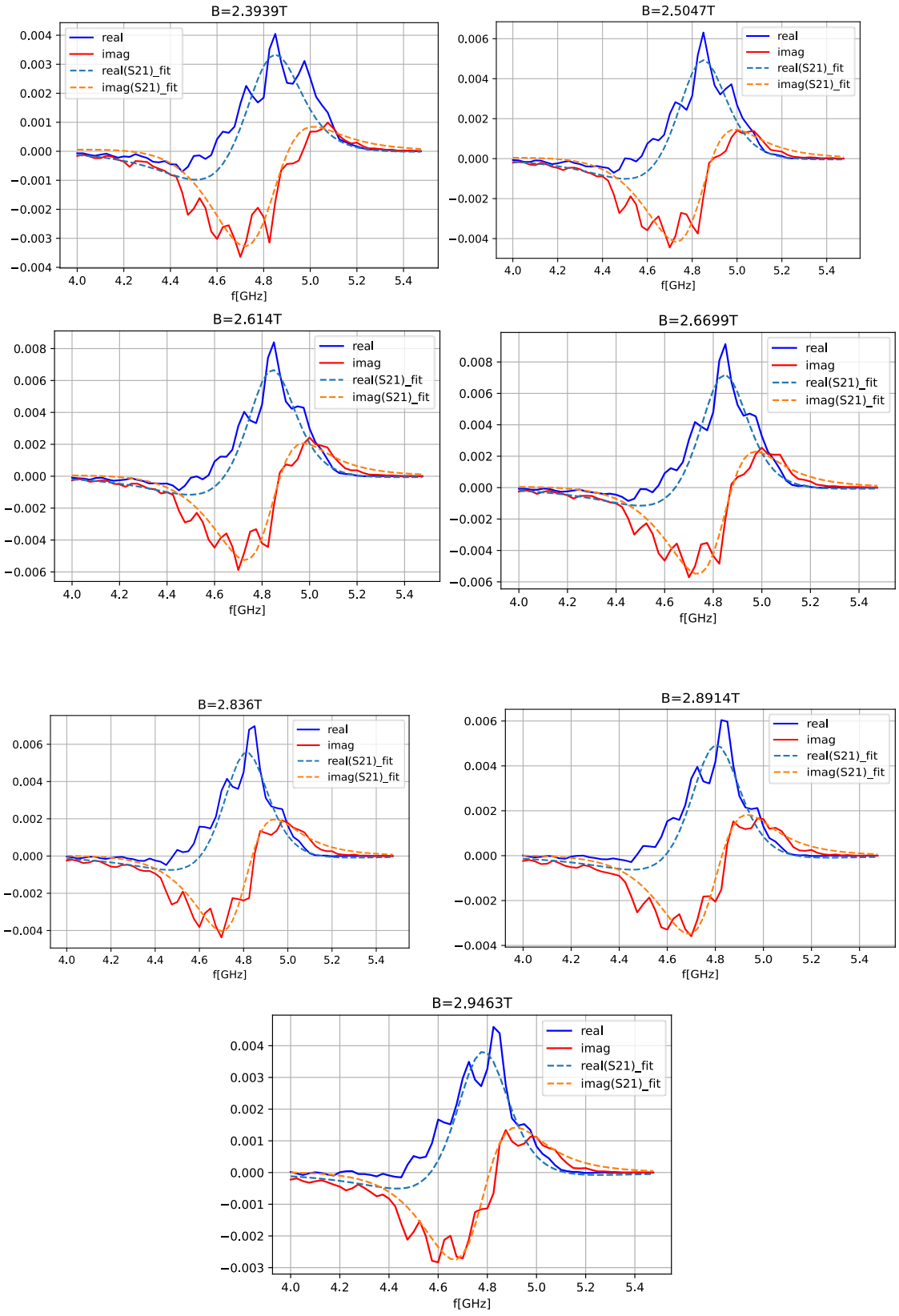

Figure 4.29: S21 data along with fits with model incorporating dissipation for different values of magnetic field across the Hall Plateau.

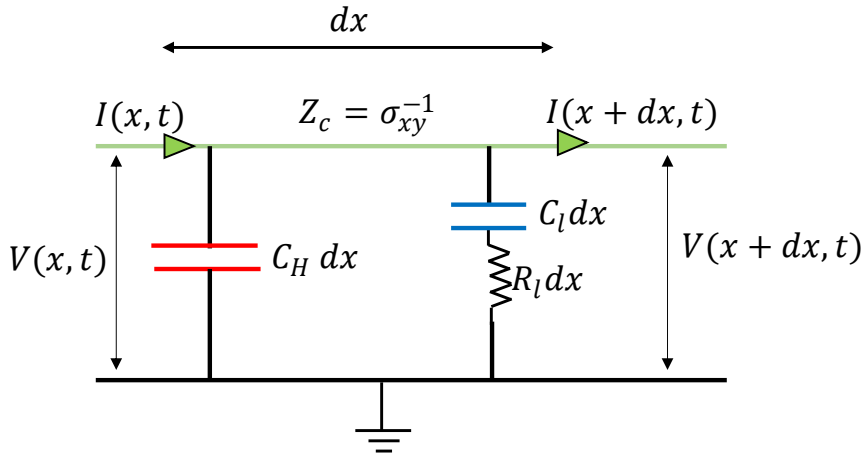

Figure 4.30: RC coupling of edge plasmons to localised states presented as dissipative transmission lines. The loss capacitance C_l and resistance R_l describe the loss of signal

Here, ρ_{C_l} is the charge on loss capacitance C_l and ρ_{C_H} is the charge on electrochemical capacitance C_H. Furthermore, in addition to equation 4.21,

$$V = \frac{\rho_{C_l}}{C_l} + \frac{\partial \rho_{C_l}}{\partial t} R_l = \frac{\rho_{C_H}}{C_H} \tag{4.44}$$

holds. Solving these equations leads to following dispersion relation:

$$\omega = \frac{\sigma_{xy} k}{C_H + C_l} - i \frac{C_l(\sigma_{xy} \omega k R_l - \omega^2 C_H R_l)}{C_H + C_l} \tag{4.45}$$

We assume that the dissipation is small. In that case, $Re(\omega) >> Im(\omega)$. The dispersion relation then becomes,

$$\omega = \frac{\sigma_{xy} k}{C_H + C_l} - i \frac{R_l C_l^2}{C_H + C_l} Re(\omega)^2 \tag{4.46}$$

This indicates that the dissipation increases with frequency. This form of dissipation has indeed been used to explain losses observed in frequency resolved transmission measurements (11) and time resolved measurements (50). From Eq. 4.46, we see that prefactor of $Re(\omega)^2$ has units of time. We make this time as our fit parameter for modelling dissipation. One can think of it as a RC time associated with this

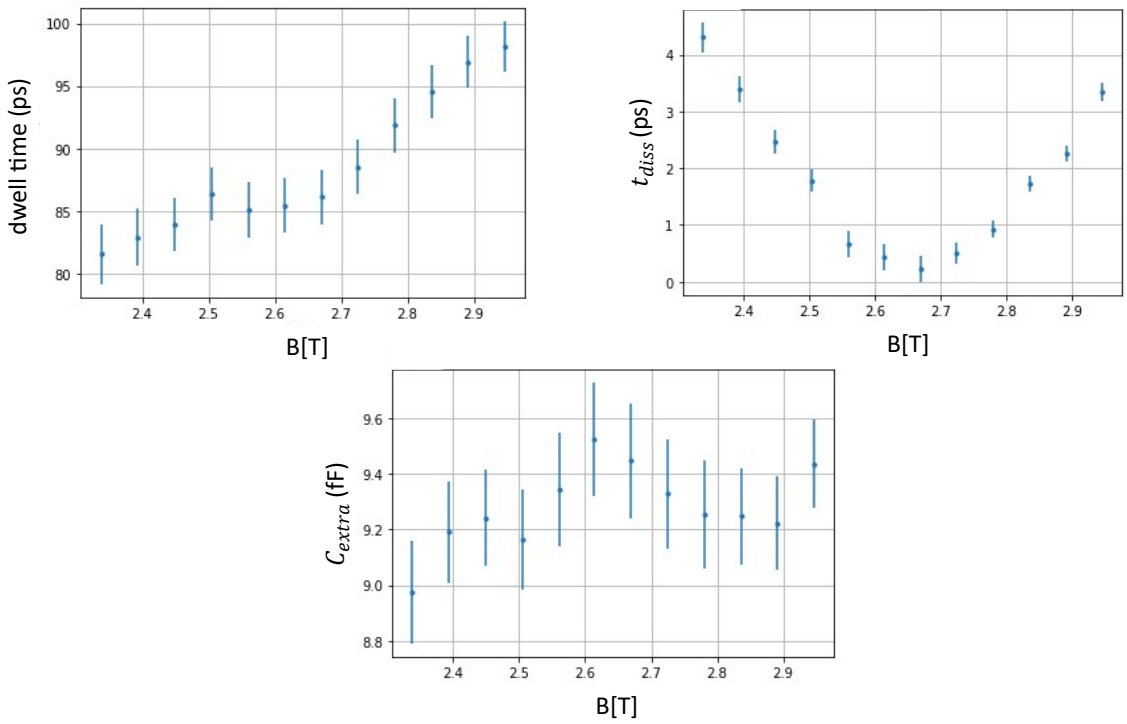

Figure 4.31: Trends of dwell time, dissipation (as a RC time) and and extra capacitance vs B

coupling that changes as we move across the hall plateau. Note that our frequency is not varied to great extent due to narrow band resonators. Again, the fit parameters are dwell time, extra capacitance (C_{extra}) and this dissipation term having units of time. Fitting the S21 curves for magnetic field across $\nu = 2$ plateau gives us the trends of these parameters with magnetic field (figure 4.31).

We observe that dwell time follows similar dependence as in resistive coupling model. The dissipation expressed in time units goes to close to zero at the centre of hall plateau. The RC time is in few pico seconds range. This order of magnitude has been observed in the literature (11) for electron gas with similar densities as ours. Extra capacitance is around 9.4 fF, not depending significantly on magnetic field. The curves with fits are in figure 4.32.

So, frequency dependent dissipation mechanism which describes capacitive coupling of edge plamons with bulk localised states seems to describe our S21 trend across $\nu = 2$ plateau. The values of the RC time obtained from the fits are reasonable.

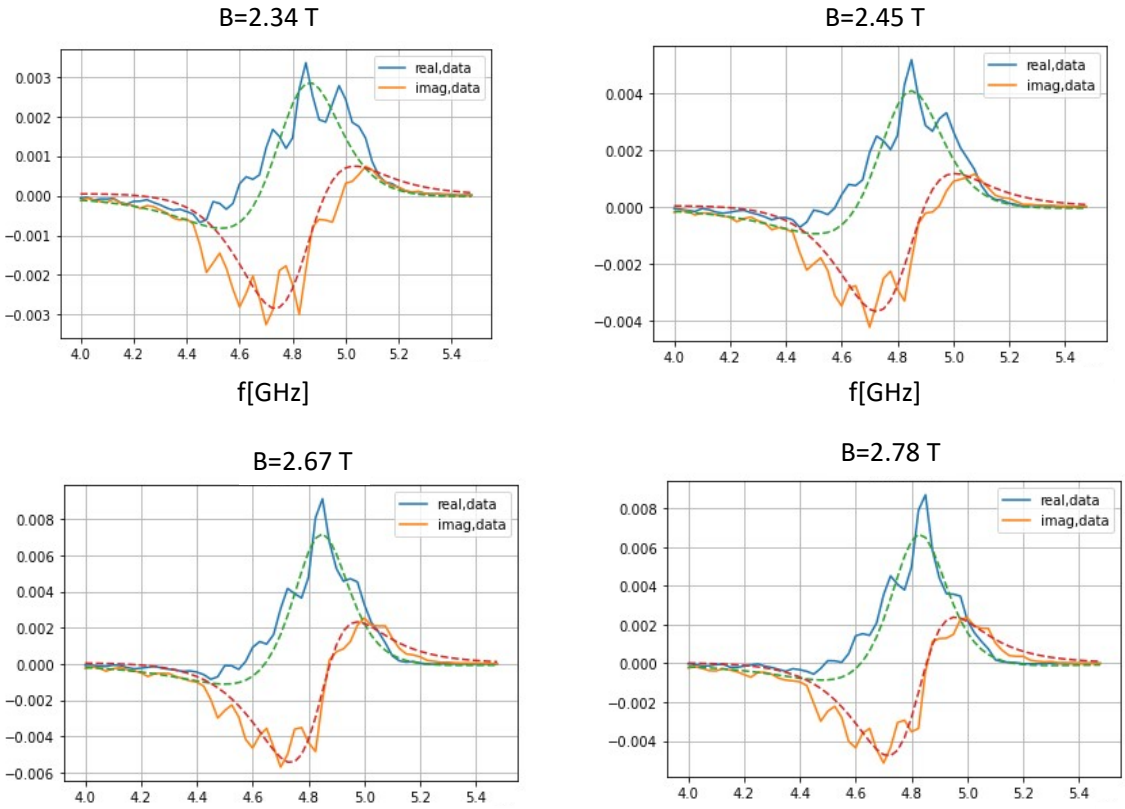

Figure 4.32: S21 fits with RC dissipation model. Here dashed lines are fits, green being real part of S21 and red being imaginary part.

The trend shows that the capacitive coupling does indeed increase as we move away from the centre of hall plateau.

Both dissipative models fit equally well our data, since we cannot efficiently discriminate between ω^2 dependence and ω independent loss mechanisms within our finite detection bandwidth. Nevertheless, the parameters extracted from ω independent loss model fit are incompatible with the DC characterisation of the sample. This strongly supports the modelling of dissipation with RC coupling circuits.

4.4 RF transport through QPC at $\nu = 2$

In the previous section we presented RF transport through the device as a function of magnetic field. A simple chiral model of uni-directional transmission line for the Sample at integer filling fraction was established which was then used to construct the transfer function to describe the measurements. Now we describe measurements at integer filling factor 2 having Quantum Point contact in action.

4.4.1 Formulation

A Quantum Point Contact partitions edge channels one by one. If there are N edge channels then the innermost channel gets partitioned first and outermost gets partitioned at the end. The current from one contact to the other in two-probe conductor through partitioned edge channel is dictated by the scattering matrix $\hat{S}_{QPC}$ of the Quantum Point contact. The transmitted and reflected currents are

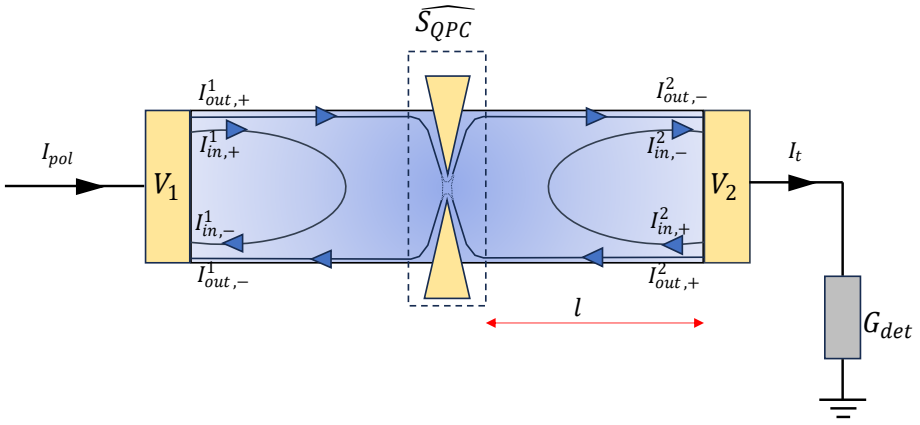

Figure 4.33: An Illustration of the RF transport at filling fraction 2 where inner-edge channel is fully pinched and outer-edge channel is partitioned by QPC. The current signal that enters the electron gas are labelled with '+' and those that leave are labelled as '-'. The total scattering matrix of the device will be composed of that of QPC and mesa where signal travels a distance 'l' towards QPC from the contact.

described by transmission and reflection probability. The channels which go through unpartitioned have transmission probability 1, each having conductance G_k. Now, from the knowledge gathered in previous section we know that for N edge channels going from one contact to other, the non-local conductance at GHz frequencies is

proportional to the product of Hall conductance $G_H = NG_k$ times the propagation phase factor $e^{-i\beta L}$ (see eq. 4.37). When one of these channel is partitioned by QPC, then the conductance will be transmission probability 't' times $G_k e^{-i\beta L}$ plus $(N-1)G_k e^{-i\beta L}$. We start with this basic model for explaining RF transport in Quantum Hall regime under the action of QPC. We can use the general expressions for Z_{2pt}, V_R obtained in equations 4.30, 4.29 and solve them for the active QPC case. For $\nu = 2$ case, N=2 and assuming that the inner-edge channel is fully pinched and outer-edge channel is being partitioned, the obtained expressions for Z_{2pt}, V_R are:

$$V_R = \frac{te^{-i2\beta l}}{\left(\frac{R_k}{Z_{det}} + (2 - e^{-i2\beta l} - (1-t)e^{-i2\beta l})\right)} \tag{4.47}$$

$$Z_{2pt} = \frac{R_k}{\left((2 - e^{-i2\beta l} - (1-t)e^{-i2\beta l}) - \frac{t^2 e^{-i2\beta l}}{(2-e^{-i2\beta l}-(1-t)e^{-i2\beta l})+\frac{R_k}{Z_{det}}}\right)} \tag{4.48}$$

As mentioned in the figure 4.33, the length 'l' is from the QPC to the contact. We assume here that sample has the same length from QPC to either of north or south contact. So, the traversed distance from one contact to other (in case of transmission) or getting back to the same contact (in case of full reflection) is '$2l$'. Using the above expression in equation 4.32, we describe S21 lineshapes for outer-edge channel. Assuming again $\beta l = \omega\tau$, here we make traversal time as fit parameter. From the figure 4.35, we see that for the transmission greater than 0.6, the fit to the data is more or less okay, but for transmission below it, fits are lousy. For very low transmission $[\tau = 0.157, 0]$, it seems like the model completely fails to describe amplitude. For one thing, we have not included the inter-edge coupling of the outer-edge channel across the QPC (see figure 4.37). In the references (41),(40), this capacitance was considered among the edge-channels across the QPC, owing to the fact that these edge channels were relatively close to each other (separation among them being the width of QPC gate electrode, which is 500 nm in our case). At the time of writing this thesis, we are trying to incorporate this capacitance in

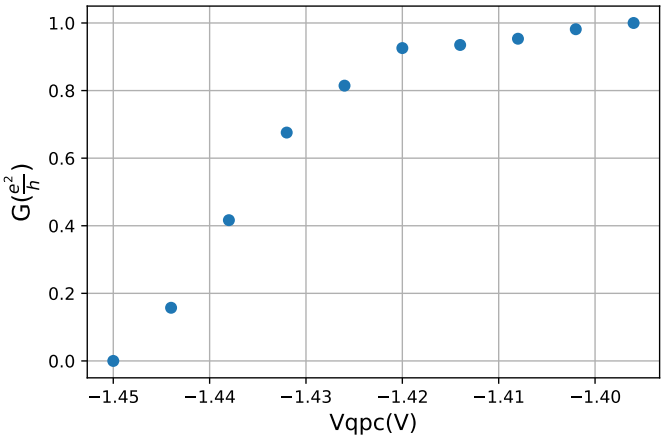

Figure 4.34: Outer-edge channel DC conductance in $\frac{e^2}{h}$ units.

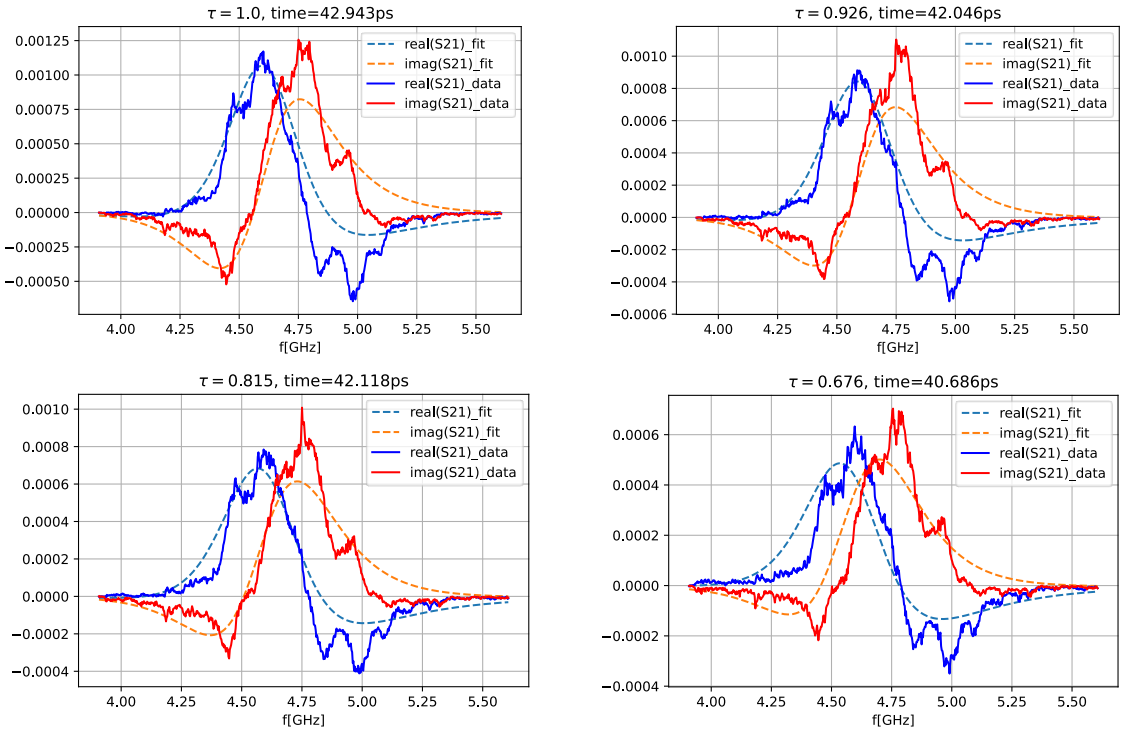

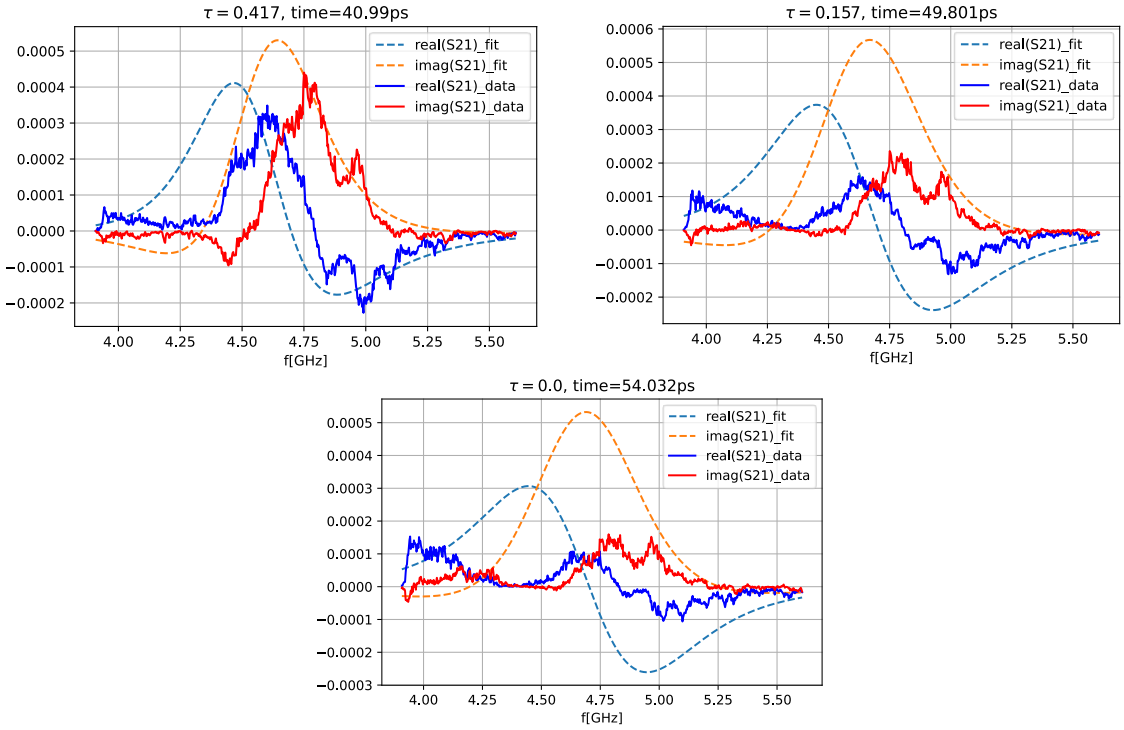

Figure 4.35: S21 data along with fits for outer-edge channel

our model and hope to explain the results for low transmission.

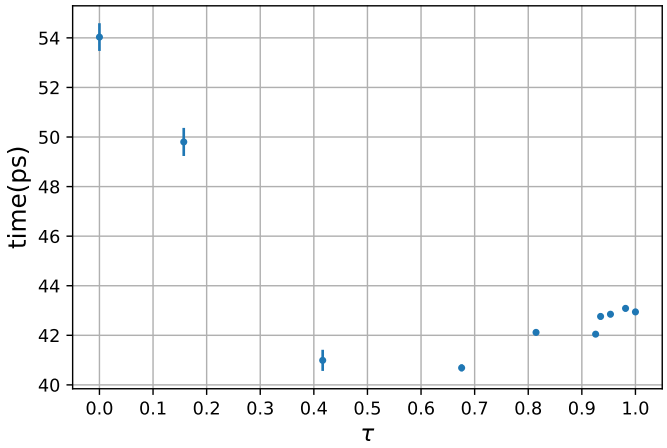

Figure 4.36: Obtained propagation time from the fits as a function of QPC gate voltage. The three values from the pinch-off are off due to lousy fits.

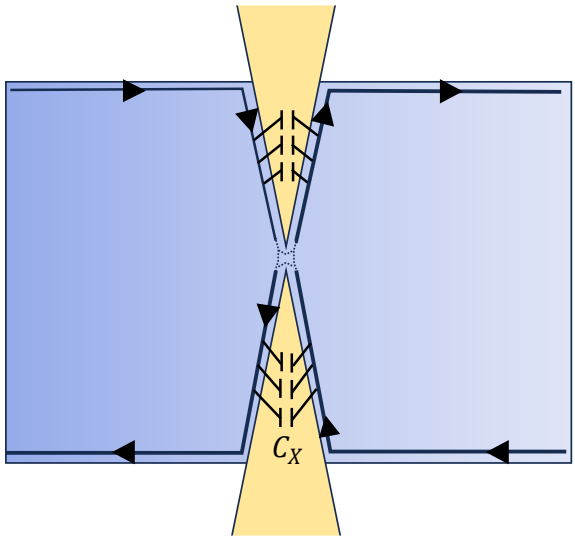

Figure 4.37: Display of Inter-edge capacitance C_X between outer-edge channel across the Quantum Point contact.

4.5 Conclusion

In the RF transmission measurements, we have explored the impedance of a 2D mesoscopic electron gas at zero and finite magnetic field.

At zero field, the lumped element description of electron gas as resistor with some capacitance to ground enabled us to characterize the RF circuit. We calibrated overall gain of chain, determined internal resistance of resonators and parasitic capacitance among these resonators. We also found out that there is a large residual capacitance to ground.

At finite magnetic field, especially for integer filling fractions, we explained the measured S21 curves by the chiral edge-plasmons propagation approach. The edge states were described as chiral transmission line with characteristic impedance given by the hall resistance, R_H. Due to this phenomena, the electron gas with some sizable impedance in series to ground acts as an impedance transformer. The impedance transformation properties depends upon hall resistance, load impedance and length of the sample. By using this information, we could explain S21 curves (both real and imaginary part) with our transfer function. We only needed the information of input impedance and trans-impedance of our electron gas in two-probe setup. With it we obtained linear dependence of velocity with filling fraction and found a residual capacitance of about 9.67fF, independent of magnetic field. This value tells us that maybe the capacitance of the resonator has this value more in it than what is provided by SONNET simulation (Jonas Mueller thesis work (60)).

Then we tried explaining the non-monotonous trend of S21 amplitude across $\nu = 2$ plateau with two phenomenological models. Both were described as dissipative transmission lines. In the first model, the dissipation was ohmic and gave resistance to ground values in 100's kilo ohm range, which is not physical as they could have been measured. In the second model, the dissipation was captured in RC circuit coupling of edge plasmons with localised states in the bulk. The dissipation term was quadratic in frequency and the RC time dependence on magnetic field gave val-

ues in pico second range. It vanished at the centre of plateau, implying no coupling to the bulk.

We also tried explaining the RF transport at the $\nu = 2$ plateau where the qpc is active. We proceeded with a simple changes to our plasmon propagation model by adding scattering centre to it. With that, for outer edge channel, we were able to explain S21 curves for transmission larger than 0.6. Perhaps, the model is too simplistic and one need to use distributed capacitance network as described in (40),(41). We would like to stress that in the RF transmission measurements, the signal fed through the ohmic contacts is injected in all edge channels along a given edge. So, the contacts feed the plasmon field on the full edge profile. Now, in the next chapter, we will discuss about noise measurements, where the injection of RF signal (shot noise to be more precise) will be done selectively in a given edge channel using the quantum point contact.

Chapter 5

Effect of Impedance composition Laws on High frequency Shot Noise In Integer Quantum Hall Regime

5.1 Introduction

We saw how the impedance of the Hall-bar behaves at high frequencies when a large impedance load (resonator in this case) is attached in series to it. The effect was observed experimentally through RF transmission measurements performed with a Vector Network Analyser. Now, in this chapter we will see how this impedance composition laws affects the Shot Noise power into to the detection circuit, delivered by our sample. We will study these effects in three different circuit configurations of the sample which will provide us more insight into the physics of it.

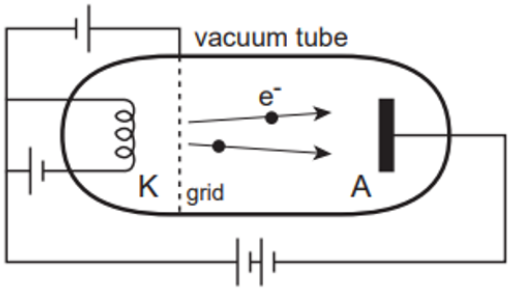

Figure 5.1: Vacuum Tube having thermionic emission of electrons from the Cathode (K). They then get transported to Anode (A). The resulting current exhibits fluctuations in time that are characterised by its average value and the charge of electrons(75).

5.2 Shot Noise

Shot noise was first discovered by Walter Schottky in 1918 (75),(76) while he was studying the current fluctuations in vacuum tubes. He found out that Spectral density of current fluctuations, where current is produced due to thermionic emission of electrons from cathode, is proportional to the charge transferred times the average current.

$$S_{II} = 2e\bar{I} \tag{5.1}$$

This noise produced is classical as the electrons that get transported are at high temperature, and hence, have Boltzmann distribution. In a Mesoscopic device, at low temperature, the charge transport through a scattering centre is probabilistic even though the bias applied across the device (figure 5.2) is constant in time. One can picture this as follows, the incoming electrons emitted through the contact at a constant rate are either transmitted or reflected from the scattering centre with some finite probability.

This does lead to an average current $\langle I \rangle$ which is constant in time, but will have statistical fluctuations about this average value. These fluctuations thus produced are of fundamental nature and are more informative than the average current itself. For instance, it tells us about the charge of carriers undertaking this transport, their statistics etc (79),(57). In the pioneering experiment (51), the shot noise

through Quantum Point Contact was measured to be below that of the classical value (equation 5.1), revealing the Fermi-statistics of electrons undertaking this transport. In the fractional Quantum Hall regime, it has revealed the fractional charge of quasi-particles tunneling through Quantum Point Contact (74; 22; 10).

Experimentally, the current fluctuations are probed at specific setup dependent

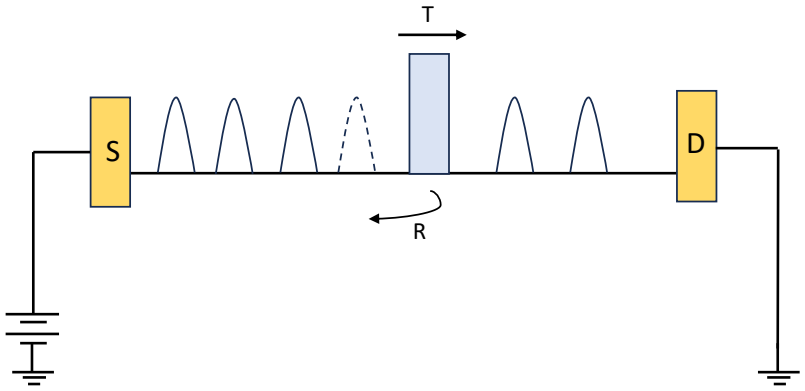

Figure 5.2: Illustration of Charge transport in a Mesoscopic device. Electrons are represented as pulses spaced equally in time. They are incident upon scattering centre from left. After the scattering, one pulse gets reflected (represented with dotted lines) while the two other are transmitted. Here the average current is constant, but the instantaneous current fluctuates in time.

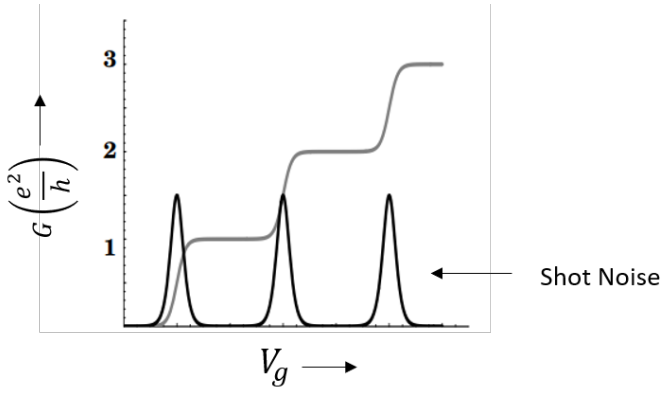

Figure 5.3: Shot Noise dependence on transmission: Curve in grey is conductance trace vs gate voltage applied on Quantum Point Contact. Curve in black displays schematically shot noise where $0 < \tau < 1$. It peaks at $\tau = 0.5$. Figure taken from (79)

time-scales that can be compared to two time scales: Temperature ($\frac{h}{k_B T}$) and bias ($\frac{h}{eV_{dc}}$). If the probed time scale is larger than both temperature and bias, we call this noise: low frequency noise. The expression for the Shot noise at low frequency

and at zero temperature for a single spin-polarized channel is as follows (79):

$$S_{II} = \frac{e^2}{h}\tau(1-\tau)eV_{dc} \tag{5.2}$$

The factor $(1-\tau)$ is the reduction factor with respect to Schottky noise that is due to fermi-statistics. Shot noise is maximum at $\tau = 0.5$ and goes to zero when either there is no partitioning ($\tau = 1$) or when there is no current ($\tau = 0$) (see figure 5.3). Also, this expression is only valid when transmission τ is energy independent. If the probed time is shorter than the temperature, then it is termed as finite-frequency noise. In this thesis, we have done studies in the finite frequency noise: $k_BT < hf_{det} \leq eV_{dc}$. The edge states due to Quantum Hall effect provide us with chiral transport channels for electrons and since we can partition edge channels selectively by Quantum Point Contact, it allows us to study noise of each single channel one by one.

5.2.1 Measurement of Finite-Frequency Noise

Our sample has on-chip resonators attached directly to the electron gas. When the noise is emitted by Quantum Point Contact, it gets detected by these resonators. We follow the detection scheme as first given by Lesovik and Loosen (54),(31),(19),(6). The current Operator $\hat{I}(t)$ defined in Landauer-Buttiker scattering theory (79) does not commute with itself at different times. This implies that it's time auto-correlation is a complex quantity. It means that power spectral density, which is the Fourier transform of this auto-correlation is not symmetric in frequency.

$$S(\omega) = \int \langle \hat{I}(t)\hat{I}(t+\tau)\rangle e^{-i\omega\tau} d\tau$$

$$S(\omega) \neq S(-\omega) \tag{5.3}$$

In Lesovik and Loosen approach, the current noise produced by the Quantum conductor acts as a small time-dependent perturbation for the detector, which in our case, is an LC resonator. The coupling is of the form:

$$\hat{V}(t) = \hat{\Phi}\hat{I}(t) \tag{5.4}$$

Here, $\hat{\Phi}$ is the electromagnetic flux across the resonator. It is analogous to the position variable in usual Harmonic oscillator description (25),(62). The Shot noise $\hat{I}(t)$ can be thought of as random force driving the oscillator. This driving produces energy exchanges between the oscillator and the conductor and following power exchange is measured:

$$P_{meas}(\omega_o) = Re(Z_{det})((1 + n_B)S(-\omega_o) - n_B S(\omega_o)) \tag{5.5}$$

Here factor Re(Z_{det}) is the real part of detection circuit impedance, with n_B as the bose-einstein occupation factor.

$$n_B(\omega_o) = \frac{1}{e^{\frac{\hbar\omega_o}{k_B T}} - 1} \tag{5.6}$$

$S(-\omega_o)$ triggers emission of energy from the conductor to the detector, whereas $S(\omega_o)$ triggers absorption from it. The equation 5.5 basically conveys that detector couples differently with positive and negative frequency noise, depending upon the resonator state. For example, if we are at zero temperature, then $n_B = 0$. It means that detector only measures the emission noise $S(-\omega_o)$ from the conductor. This is similar to spontaneous emission into vacuum. At finite temperature, we not only have stimulated emission term $n_B S(-\omega_o)$ in addition to spontaneous emission, but also the stimulated absorption term $-n_B S(\omega_o)$. We assume in our experiments that resonators are very cold (at mixing chamber temperature $\sim$ 15 mK). This essentially makes Bose-Einstein factor very small ($\sim e^{-15}$), thus making the measured

noise power spectral density predominantly as emission noise from the Quantum conductor. So, all the noise measurements shown in this chapter are emission noise measurements based on this assumption.

The above described method of noise detection, which is implemented in our device has an advantage that with this scheme we are able to couple the current fluctuations of the Quantum conductor to the transmission line, which can then be used to convey these signals to RF detection circuit at room temperature. We then use standard RF signal processing techniques to measure and analyse these fluctuations. This method, which first came out in (21) has been used to perform some amazing microwave Quantum Optics experiments (64),(70),(71), where correlations among the photons by the emitted noise have been measured. We do not explore this aspect of noise measurements in this thesis.

5.2.2 Experimental method of Noise Measurement

Having said about the principle of measurement of noise in the previous section, we will now talk about the experimental procedure with which noise is measured. The noise signal emitted from the sample has to be amplified for it to be detected well at room temperature. For this reason, we use amplifiers. First set of amplification is done at 4K stage by cryo-amplifiers known as **HEMTs**. These amplifiers provide a gain of about 40dB and add a parasitic noise equivalent to thermal noise of a resistor kept at a temperature of few kelvins. They need to be impedance matched to ensure all the incident noise signal is amplified and nothing is reflected. The power spectral density at the output of this amplifier reads : $S_P(\omega) = G \times (k_B T_N + Z_o S_{II}(\omega))$, where $S_{II}(\omega)$ is the current noise emitted by the Quantum conductor towards $Z_o = 50\Omega$ and T_N is the noise temperature of the amplifier.

The amplified signal can then be brought to the room temperature by further amplification with room temperature amplifier. So, the Radio-frequency amplification chain for noise signal consists of amplifier at 4K stage and at 300K stage. The

signal after the amplification from this cascaded amplifier chain is : $S_P^{(2)}(\omega) = G^{(2)} \times (k_B T_N^{(2)} + G^{(1)} \times (k_B T_N^{(1)} + Z_o S_{II}(\omega)))$. If $G^{(1)} T_N^{(1)} >> T_N^{(2)}$, then the signal to noise ratio is dominated by the noise level of the first cryogenic amplifier.

This parasitic noise signal, as mentioned before, is very large compared to the emitted noise. The cryo-amplifiers used in our setup are provided by Low Noise Factory and have noise temperature of 2-3 K. Compared to that, temperature equivalent of the emitted noise from Quantum Point contact is of the order of 7-9 mK. When the bias is applied to the system, we call it as an **ON** state of measurement. In this state the signal measured at the output of amplification chain is the already mentioned expression of $S_P^{(2)}(\omega)$, or just $S_P(\omega)$ if we neglect contribution of noise from room temperature amplifier and keep in mind that Gain $G = G^{(1)} \times G^{(2)}$. When no bias is applied, which is the **OFF** state, the measured signal is $G^{(1)} \times G^{(2)} \times k_B T_N^{(1)}$. So, we extract our signal by doing **ON -OFF** procedure. However, the Gain G has slow variations in time. To correct for these variations, we divide the difference of ON and OFF by the OFF measurement. Hence, the measured quantity is:

$$S_{meas} = \frac{S_{ON} - S_{OFF}}{S_{OFF}} \tag{5.7}$$

We make some crucial assumptions while following this procedure of measuring emitted noise from the sample at room temperature. First, the input noise from the cryogenic amplifiers is constant in time. Second, during time delay between the measurement of the ON signal and OFF signal, we assume that Gain of the chain does not changes. The typical time between them is 1 minute in our data acquisition routine. A small change of gain during this time delay can ruin the measurement. For the auto-correlation noise spectral density, the OFF signal is the parasitic noise signal $k_B T_N$ of the given detection line. Here ON and OFF signal are almost identical in magnitude since emitted noise is very small compared to OFF noise. For the cross-correlation, the OFF signal is the parasitic cross-talk between

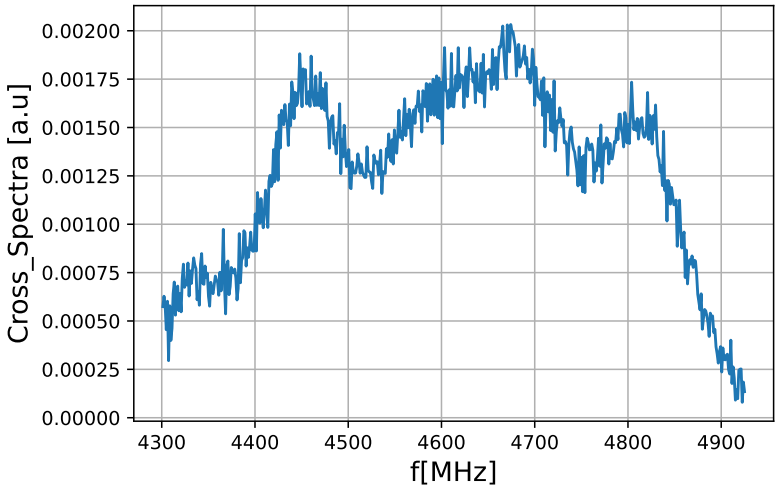

Figure 5.4: Typical plot of Power Spectral Density. Here the noise is given in terms of input noise of the Cryo amplifier ($k_B T_N$). The wiggles in spectra is due to standing waves form due to imperfect connection in the detection chain between sample and the cryo amplifier.

two different lines which is much smaller than **OFF** noise signal of each of given lines. In the light of this, we see that fast variation of the gain is more likely to make auto-correlation noise measurement lousy than cross-correlation by the experimental bias arising from the gain drift. So, in this thesis, as will be shown in the coming sections, we have measured noise in the setup where each detection line is divided into 2 lines so as to measure auto-correlation more accurately. It is done by using a -3dB Hybrid coupler (shown in blue in figure 5.7). This is one way we fight with variation of the gain that changes faster than averaging time. Figure 5.4 gives the measured noise spectra by following the ON/OFF procedure (see equation 5.7).

Also, we see in figure 5.7, there is another Radio-frequency device (2 of them per each line infact) just before the input of Cryo-amplifier. These 3-port devices are known as circulators and have chiral transport properties due to the presence of ferritic material in them. They protect the sample from the voltage noise coming from the cryo-amplifiers. Rather, that noise is sent to 50 ohm to ground which is thermalized at the 12mK mixing chamber plate.

The signal to be detected at room temperature is a microwave voltage generated by

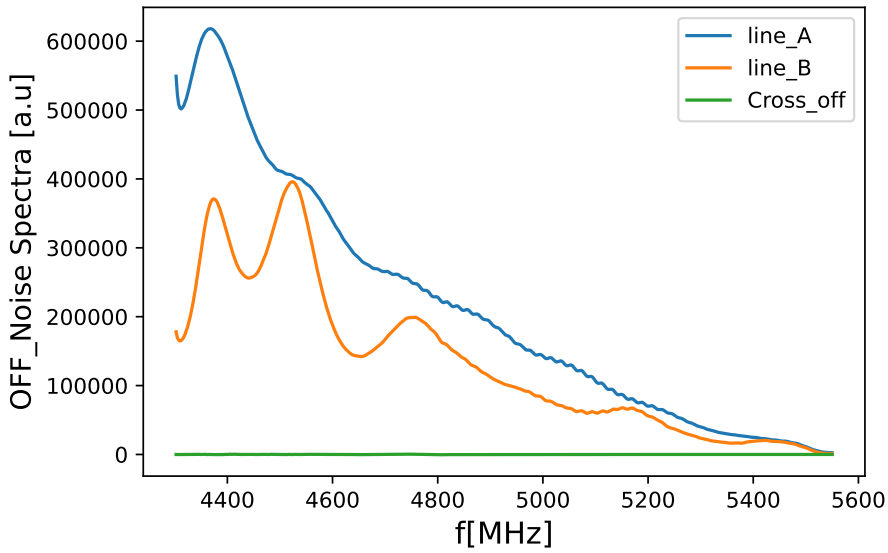

Figure 5.5: OFF Noise spectra. Blue and Orange is the OFF spectra of the two detection lines across QPC, green is the OFF spectra of cross-correlation of the two. As can be seen, Cross-OFF is negligible as compared to auto-correlation OFF signal.

the sample at the input of the transmission line, oscillating in the coupled 4-8 GHz band is:

$$V_{ac}(t) = V_o(\hat{a}e^{-i\omega t} + \hat{a}^{+}e^{i\omega t}) \tag{5.8}$$

with $V_o = \sqrt{Z_c\hbar}$ is the zero point fluctuations in the transmission line of impedance Z_c (82). Experimentally, it is not possible to digitize this high-frequency signal directly with our Analog to digital converter (ADC) card. Rather, we adopt the method of Heterodyne detection, where this signal is multiplied with another classical oscillating signal of frequency ω_{LO}. It is produced by local oscillator. As a result of this multiplication, we obtain signal containing two parts: one which is at frequency $\omega_{LO} - \omega$ and the other at $\omega_{LO} + \omega$. Only the low frequency part is chosen by passing it through a low-pass filter. As can be seen in the figure 5.4, spectrum starts in frequency space from 4.3 GHz, but has as centre frequency of about 4.7 GHz. The frequency ω_{LO} is chosen such that all the spectra can be brought down to low-frequency, making 4.3 GHz to be DC, where it can then be digitized with the ADC card. Since the spectra is not decaying sharply at 4 GHz (as resonance lies close to it), we put another band-pass filters that can cut the spectrum more

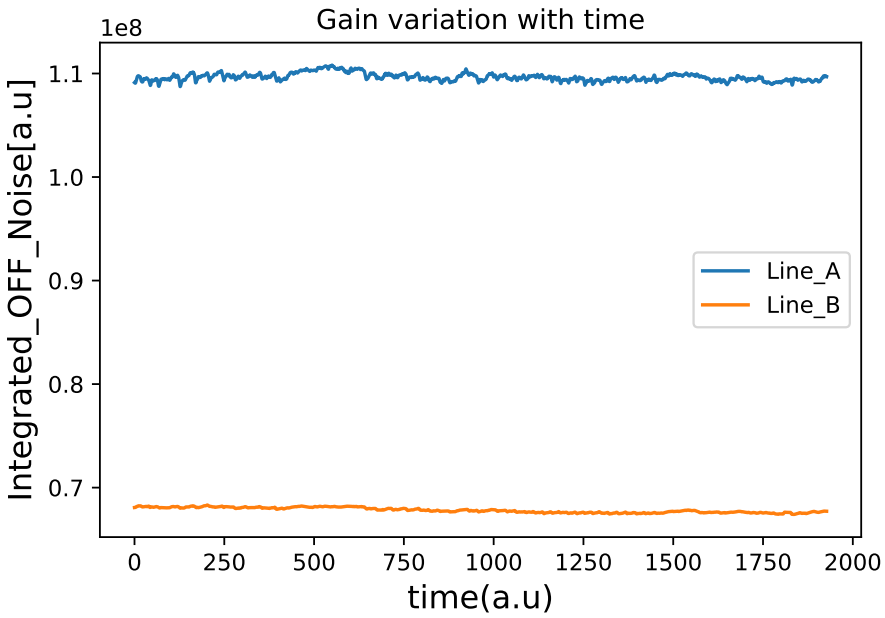

Figure 5.6: Variation of the integrated noise power in OFF configuration with time for two different detection lines. These Slow variations are taken care of by dividing the excess noise by OFF signal. Here each point is obtained by summing area under the curve for the OFF spectra in figure 5.5.

sharply. The purpose here being that when the heterodyning is done, it produces less aliasing of the down-converted signal. We use bandpass cavity filters centered around 5 GHz with different bandwidths to do the job.

After heterodyning is done, signal is then passed through a low-pass filter, after which it then goes to the ADC for signal processing. The ADC can operate at 5 Giga samples/ sec. When all the four channels are being used (as shown in figure 5.8),the sampling rate per channel is 1.25 Giga samples/sec. This gives a Nyquist bandwidth of 625 MHz. For the case where only two channels are used (as in the case of 3pt-setup shown in the next section), the sampling rate is 2.5 giga samples/sec, giving the bandwidth to be 1.25 GHz.

After having said about experimental measurement of noise, let's have a look at the RF Shot noise characterized by these techniques.

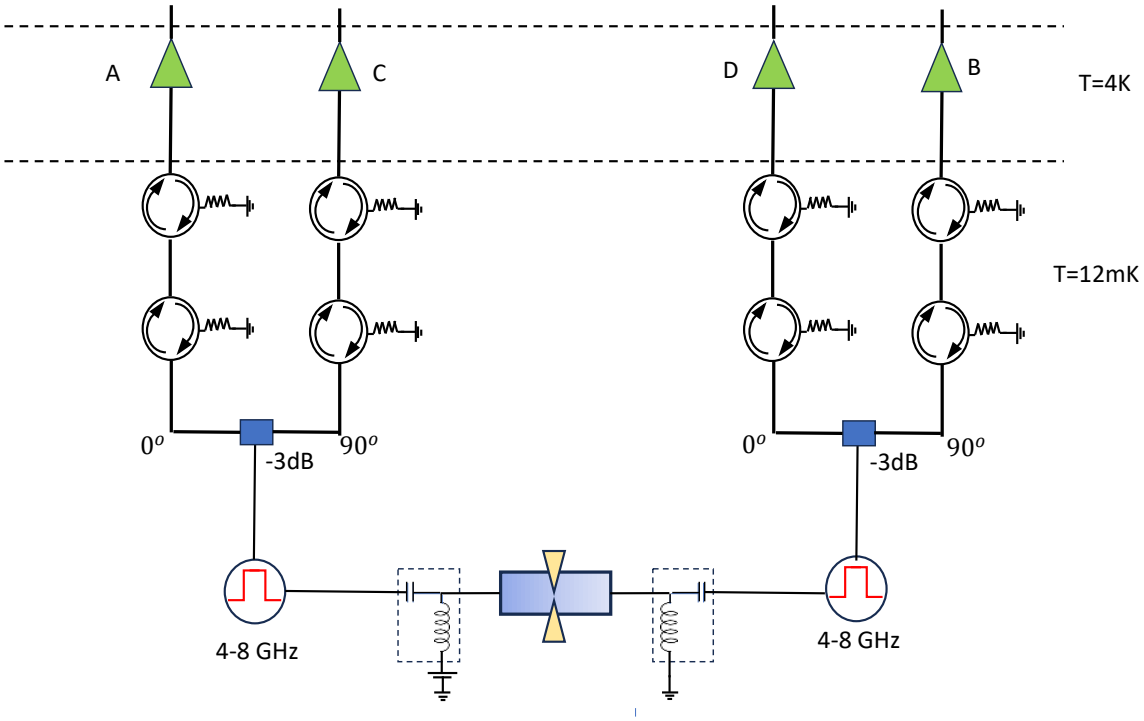

Figure 5.7: Noise setup for measuring auto as well as cross-correlations accurately from the sample. Here is the setup till 4K stage of the Dilution fridge. Each main detection line is split into two by -3dB coupler.

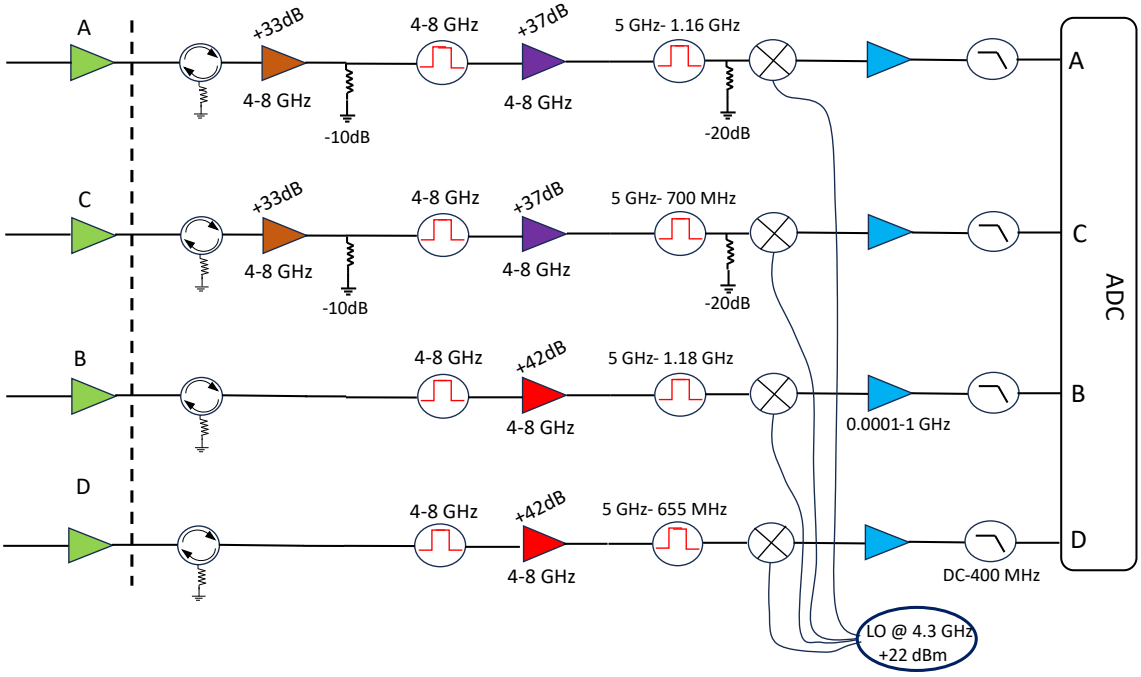

Figure 5.8: Room Temperature setup for the shot noise measurement. The noise signal after amplification from the Cryo-Amps (Shown in green) gets into the room-temperature chain. We have tried to maintain the overall gain of about 40dB in all the 4 lines. After the amplification and band-pass filtering of the noise signal, it is then fed into the mixer where it is mixed with a local oscillator tone set at 4.3 GHz with an amplitude of +22 dBm at its input. This local oscillator signal is divided into 4 lines equally, making the amplitude at the input at the mixer to be +16 dBm. After this mixing the down-converted signal is selected by low-pass filter, which then is finally fed to the ADC.

5.3 Noise in 3-point configuration

Here we report the measurement of RF noise in the integer quantum Hall regime. Here the chirality is counterclockwise as set by out of plane magnetic field. We set the side-gates to 0V. By applying current bias on the top (east) ohmic contact we send a current along the top edge of the mesa. It then gets partitioned at the Quantum Point Contact and the reflected (transmitted) current (and noise) reach the resonator situated at north (south) sides of the sample respectively following the edge channels. We study this measured noise as a function of bias, V_{dc} and QPC gate voltage, V_g.

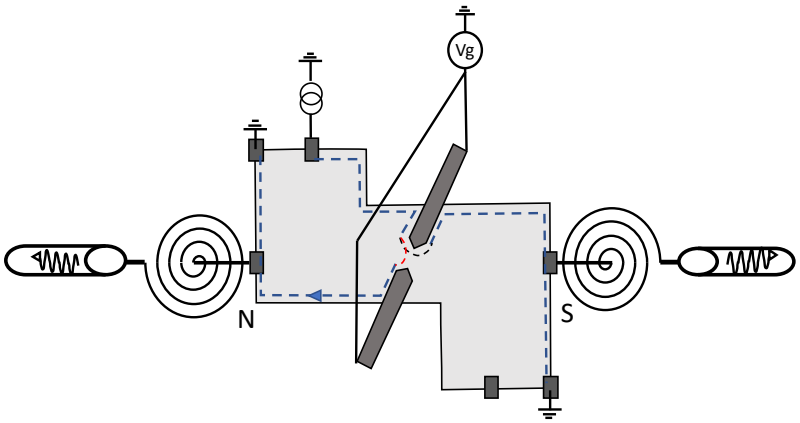

Figure 5.9: 3-point Configuration : Noise emitted by the Quantum Point Contact reach the resonators which acts as a receiver antenna

Let's first discuss qualitatively the shot noise power measured at $\nu = 2$. What we observe here is that the detected noise power follows a canonical dependence on the transmission : $S_{II} \propto \tau(1-\tau)$ for outer edge channel. For the inner edge channel (see figure 5.10), however, we right away observe two things: the dependence on the QPC transmission is not canonical (as in for outer edge channel) and its magnitude is almost three times less as compared to that for outer edge channel. The transmission for inner edge channel depends upon energy, as can be seen from the figure 5.11, whereas, it is energy independent for the outer edge channel.

In the following section we provide a more quantitative analysis of the measured noise. In order to do so, we need to understand how does the detected noise power

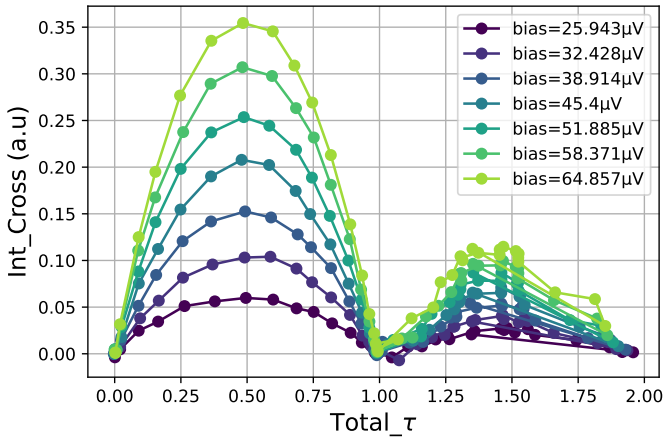

Figure 5.10: Shot noise at $\nu = 2$ for inner and outer edge channels as a function of transmission at different applied biases. The noise power measured while pinching inner-edge channel is 3 times lower as compared to that of the outer edge channel.

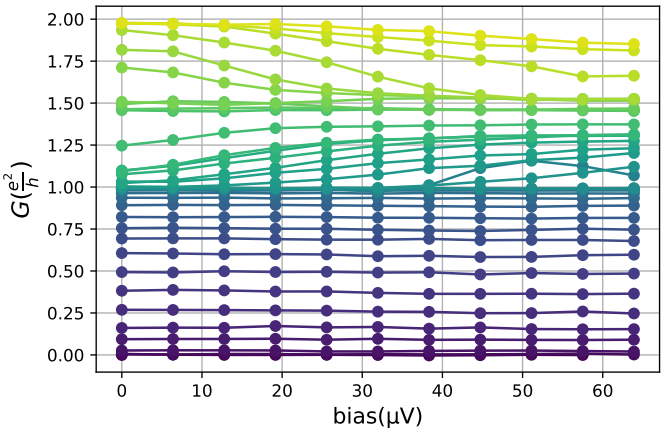

Figure 5.11: DC Transmission for both inner $(1 < \tau < 2)$ and outer$(0 < \tau < 1)$ edge channel in 3pt configuration. Energy dependence of inner channel is evident, while it is feeble for outer channel.

is related to shot noise emitted by the QPC.

5.3.1 Microwave coupling

For a single channel in general, the complete emission shot noise formula is given as (83):

$$S_{II}(f) = A\frac{e^2}{h}\tau(1-\tau)\left(\frac{hf+eV}{e^{\frac{hf+eV}{k_BT}}-1} + \frac{hf-eV}{e^{\frac{hf-eV}{k_BT}}-1} - \frac{2hf}{e^{\frac{hf}{k_BT}}-1}\right) \tag{5.9}$$

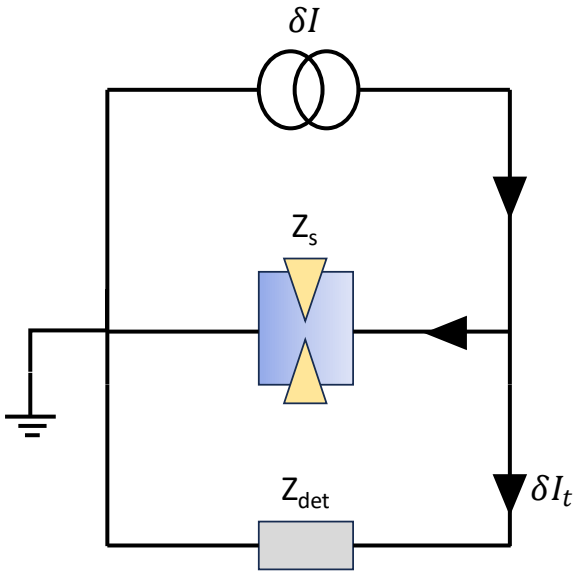

Figure 5.12: Current noise circuit: Quantum conductor of impedance Z_s acts as a source of current noise δI. The noise δI_t that gets transmitted to the detection impedance Z_{det} is simply given by current division between these two impedances.

Here **A** is the ratio of microwave coupling of the emitted current noise power in the detection circuit to the noise temperature of the Cryo-amplifier. In our experiments, the measurement of noise is done in the units of cryo amplifier noise ($k_B T_N$). In order to explain the power spectral densities for different bias and transmission, we need to know the origin of the factor **A**. For that we need to quantify microwave coupling of the noise emitted by Quantum point contact to the detection circuit. Let's discuss the circuit given in figure 5.12, where we have our noise source which injects some current fluctuations onto the detection circuit. Let the sample impedance be denoted as Z_s. Due to current division, the current fluctuations entering the detection impedance Z_{det} will be given as:

$$\delta I_t = \delta I \frac{Z_s}{Z_s + Z_{det}} \tag{5.10}$$

The noise power detected on the detection circuit will then be :

$$\delta P = \langle \delta I_t^2 \rangle Re(Z_{det}) = \langle \delta I^2 \rangle \left| \frac{Z_s}{Z_s + Z_{det}} \right|^2 Re(Z_{det}) \tag{5.11}$$

We would like to determine this microwave coupling in the 3-point setup when the outer edge channel is being partitioned. In order to do that we will make current balance at the contacts which couple the detection circuit (resonator) to the sample. These contacts are labelled as 'N' and 'S' in the figure 5.13. For the 3pt-setup, the impedance to ground is always the hall resistance R_H. This can be seen from equation 4.36 where $Z_{det} = 0$. The shot noise emitted by Quantum Point contact towards south contact is negative to that emitted towards north contact due to conservation of current fluctuations. However, when this noise signal reaches the contacts, it acquires the propagation phase ϕ. Assuming that the sample length from the QPC to either detection setup contacts is same, this phase acquired is the same as well. The fluctuations injected by the QPC to the north contact is:

$$\delta I_{inj} = \delta I e^{-i\phi} \tag{5.12}$$

This fluctuating signal then undergoes current division at that contact. Some of it goes to the detection setup circuit δI_t, while the rest of it, δI_{ref} goes to cold ground on chip via Hall resistance as the voltage at that contact injects signal in both edge channel. These current fluctuations are related to the voltage on that contact as:

$$\begin{aligned} \delta I_t &= \delta V_n G_{det} \\ \delta I_{ref} &= \delta V_n 2G_K \end{aligned} \tag{5.13}$$

The current balancing at that contact gives us:

$$\begin{aligned} \delta I_t &= \delta I e^{-i\phi} - \delta I_{ref} \\ \delta V_n G_{det} &= \delta I e^{-i\phi} - \delta V_n 2G_K \end{aligned} \tag{5.14}$$

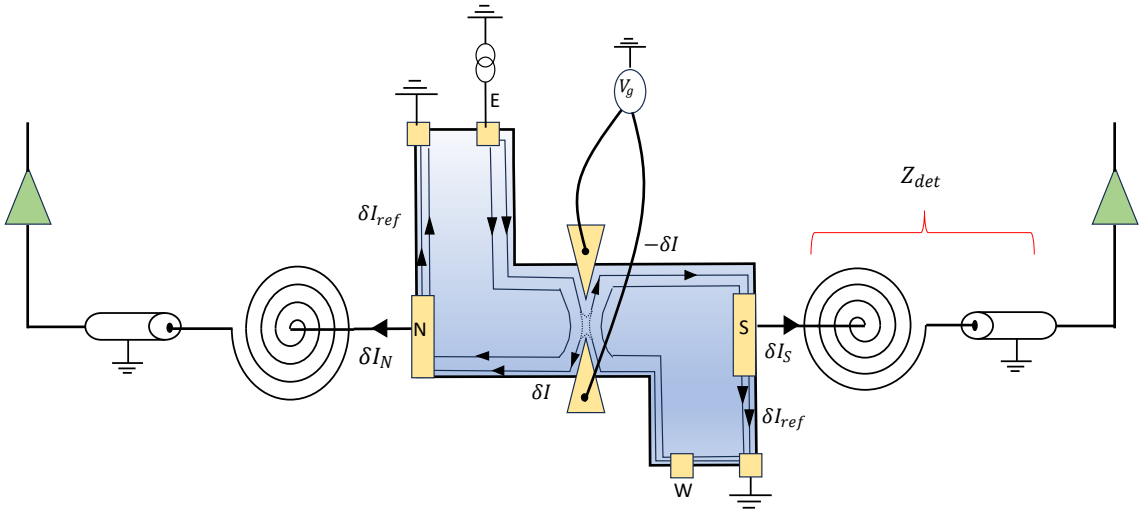

Figure 5.13: Circuit schematic for 3-pt configuration. Inner-edge channel is fully pinched while outer-edge is transmitted with probability τ. The noise from QPC gets injected into outer edge on both sides of it which then reach resonator after having current division. The power received into the detection lines is δI_n and δI_s which are some fraction of δI, the bare noise emitted from QPC, owing to the current division.

Similarly, for the south contact, we get:

$$\delta V_s G_{det} = -\delta I e^{-i\phi} - \delta V_s 2G_K \tag{5.15}$$

From equations 5.14 and 5.15, we see that fluctuating voltage at north and south contact are negative of each other. Using 5.13 and 5.14, we obtain the transmitted current fluctuations as:

$$\delta I_t = \frac{\delta I e^{-i\phi}}{1 + 2G_K Z_{det}} \tag{5.16}$$

The detected power spectral density in terms of noise temperature of cryo-amplifier is thus,

$$\frac{\delta P}{P_{off}} = \frac{1}{k_B T_N} \frac{\langle \delta I^2 \rangle Re(Z_{det})}{|1 + 2G_K Z_{det}|^2} \tag{5.17}$$

We observe that equation 5.17 is similar to equation 5.11 apart from the factor $\frac{1}{k_B T_N}$, so as to have quantity which is what we measure experimentally. The microwave coupling for the 3 point setup is completely independent of the transmission probability. This is due to the chirality of edge magnetoplasmons. The current fluctuations that

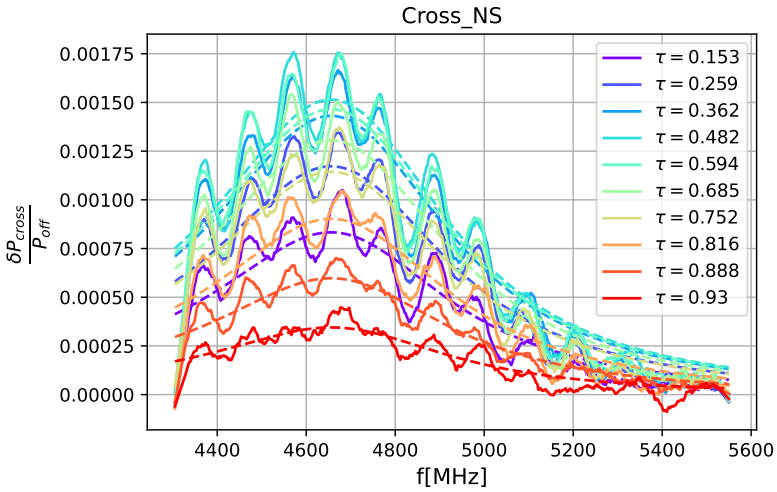

Figure 5.14: Cross-spectra at $58\mu V$ for different transmissions along with the fits (dashed lines) with equation 5.18. The data is presented here after savgol-filtering it for clarity.

are reflected back to the sample from the contact (let's say at the north contact 'N') go to the ground and do not feedback to the quantum point contact (see figure 5.13). The resonators just act as antenna for the noise signals produced by the Quantum point Contact.

5.3.2 Noise Spectra

Now that we know how the emitted noise couples to the detection circuit, we use this information to explain our measured spectral density and integrated noise power. From the fit we extract the effective noise temperature (T_N). For this particular set of experiment, the measured bandwidth of power spectral density is about 1.25 GHz around 4.7 GHz, the resonance frequency. We go to large bias value (at about $60\mu V$) and assume that bare noise produced by QPC is linear function of bias. This leads to the following formula for detected power spectral density:

$$\frac{\delta P}{P_{off}} = \frac{1}{k_B T_N} \frac{(eV - hf)\tau(1-\tau)}{R_K} \frac{Re(Z_{det})}{|1 + 2G_K Z_{det}|^2} \tag{5.18}$$

Using this we obtain fits of measured power spectral density and get noise tem-

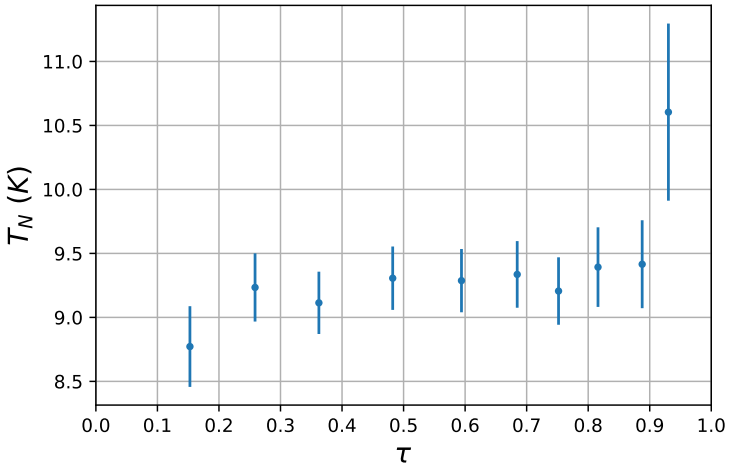

Figure 5.15: Obtained noise temperature from the above spectra fit. Note that for very low and very high transmission the noise power spectral density is low, thereby making fits a bit lousy. Thus values of T_N is lousy for low and large transmission

perature to be about 9.3K as referred to the output of QPC (figure 5.15. The data for power spectral density is a cross-correlation signal (figure 5.14). From the previous discussion on measuring our noise spectrum, we noted that difference of ON and OFF noise is normalised by OFF noise which is the cryo-amplifier noise $k_B T_N$. Now, this is true for noise measured in one line (for auto-correlation). For the cross-correlation, we normalise it by the product of OFF signal of north and south detection lines. The noise temperature is thus, square-root of product of noise temperature of two-lines: $\sqrt{T_{N1} T_{N2}}$. The cryo-amplifier's used in north and south lines have noise temperature of 2-3 K at their input. We measure large noise temperature as referred to the output of QPC. This is due to the losses that happen when the noise signal that travels from the sample to these amplifiers. Some of the power is burnt in the resonators coils (they have internal resistance of 12.5Ω), while rest is lost due to propagation. The microwave chain attenuates the RF noise power by roughly 6 dB.

Knowing the effective noise temperature, we can determine the electronic temperature by fitting the noise power with 5.9. It comes out to be about 65mK (figure 5.16). Now that we know both noise temperature of the amplifier and electronic

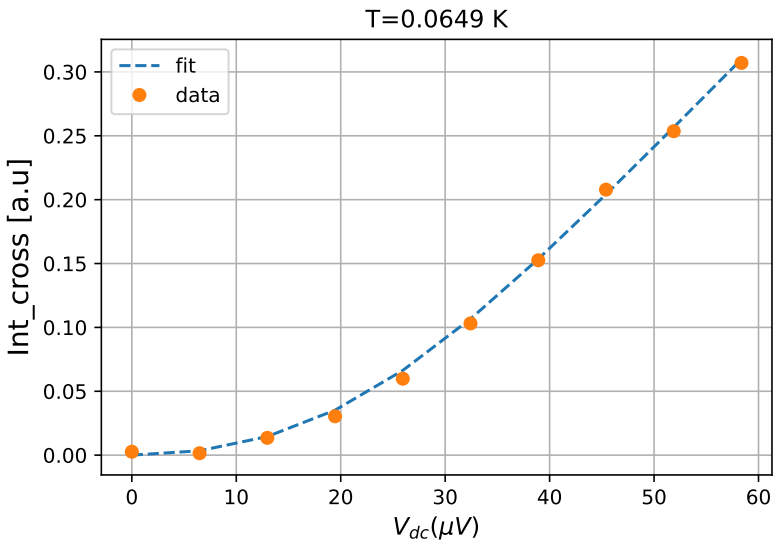

Figure 5.16: Integrated noise power vs DC-bias. The transmission for the outer-edge channel is 0.48. The obtained temperature is 64.9 mK. Here each point of data is obtained by summing the noise spectral density over the frequency bandwidth.

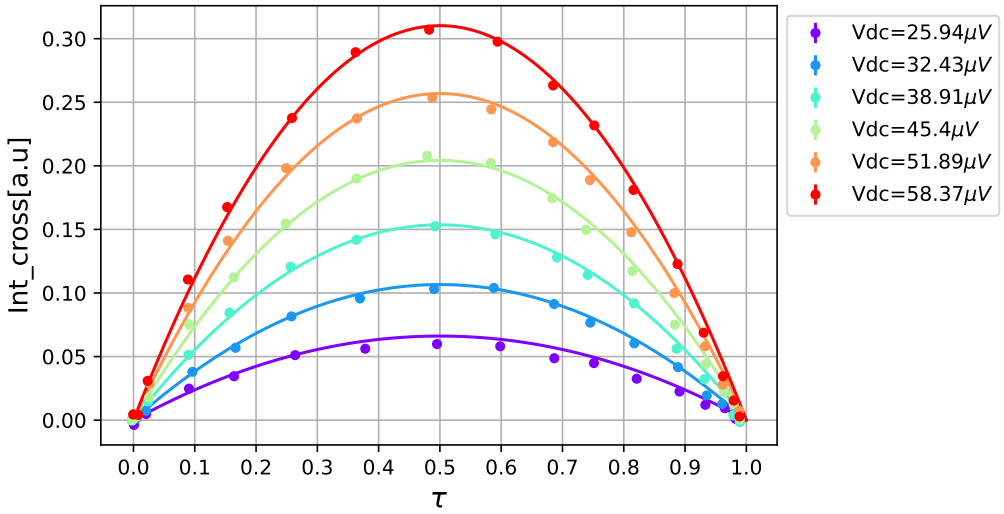

Figure 5.17: Transmission dependence of the Integrated noise power for outer -edge channel. It follows canonical $\tau(1-\tau)$ dependence. The continuous lines is obtained by summing the formula 5.17 over frequency, where T_N is input as 9.3K and $\langle \delta I^2 \rangle$ is given by equation 5.9 having temperature as 64.9 mK.

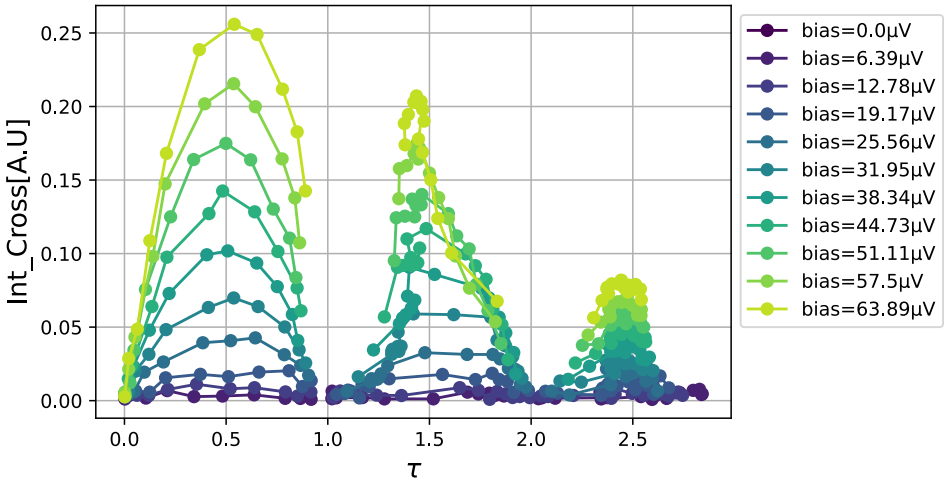

Figure 5.18: Integrated noise power as a function of transmission for different bias values at $\nu = 3$ Hall plateau. The detected noise power decreases as one injects noise signal from outer edge channel to innermost edge channel with quantum point contact.

temperature and we know expression for the detected power spectral density, we can use this info test our prediction with data of integrated power vs transmission curve (see figure 5.17).

5.3.3 Dissipation

We saw in figure 5.10 that the detected noise power from inner-edge channel was highly attenuated with respect to the outer edge channel. The attenuation was close to 70 percent of that in outer edge channel. Note that this measurement is done at centre of hall plateau. At the centre of hall plateau, in the precedent chapter, we described RF transmission through the edge channel as lossless. Losses as coupling to the bulk localised states were invoked when magnetic field is changed across the $\nu = 2$ plateau. To explore it further, we have done the same noise measurements at $\nu = 3$ filling fraction (centre of plateau). In the figure 5.18, we see that for a given DC bias applied, the detected noise power is maximum for outer-edge channel followed by middle and inner channels. And moreover, the relative reduction of noise power from inner edge channel is again 70 percent compared to that in outer edge

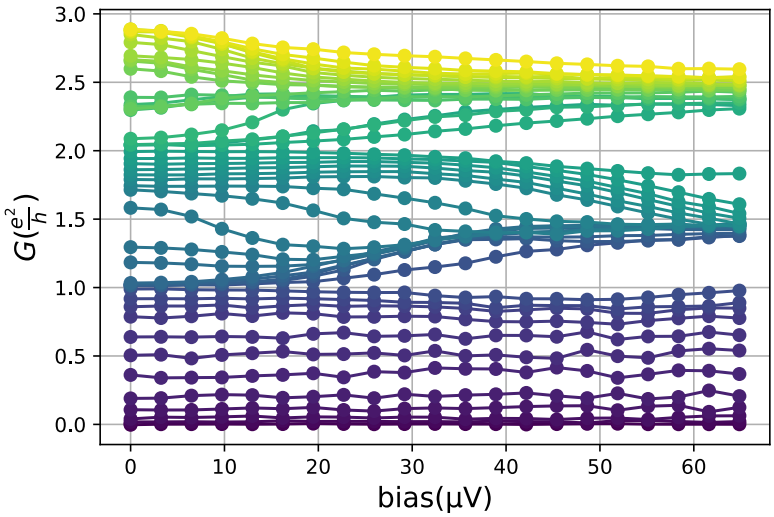

Figure 5.19: Differential conductance for different edge channels. The energy dependence of transmission for middle and inner edge channel affects the detected noise power.

channel. The losses seen in noise measurements at the centre of plateau seem to contradict the understanding we obtained from the measurements of the precedent chapter.

We note one thing. In RF transmission measurements, the signal is injected from the ohmic contact which is galvanically coupled to all charge carriers at the edge. On the other side, in noise measurements, quantum point contact can selectively inject noise (RF signal) either in inner or outer edge channel. This relation between dissipation and the way RF signal is injected into the edge channel lead us to consider the different edge-magnetoplasmon modes that carry the signal. These modes were first theorized in a hydro-dynamical model by Aleiner and Glazmann (1). They studied low-energy spectrum of collective excitations of electron gas placed under high magnetic field having smooth edge profile. They found out that along with usual charge edge-mode, there are other modes as well having different spatial variation of charge density. In the charge edge mode, the density variation is along the edge, whereas for the other modes, the variation of density happens as well in the transverse direction to the edge (see figure 5.20). All these modes live all across the edge channels. In the RF transmission measurement, the signal injected via ohmic

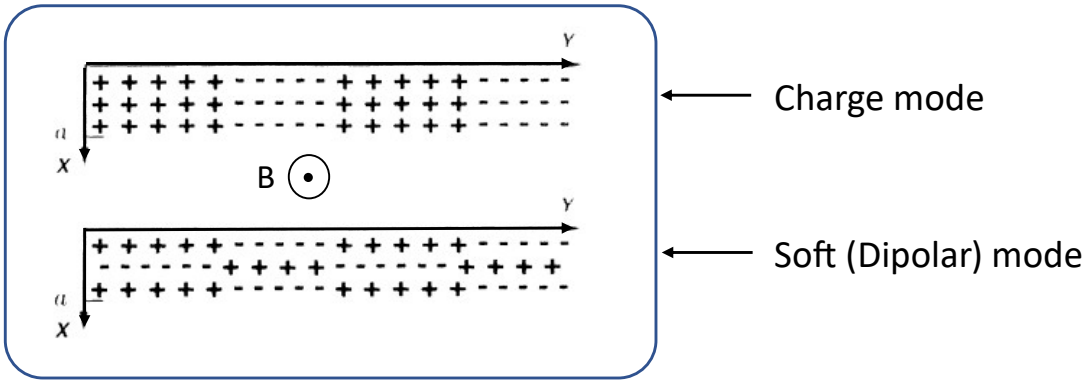

Figure 5.20: Taken from (1). Charge modes (faster, long lived) oscillate along the edge of the electron gas, whereas dipolar modes (slower and short lived) oscillate transverse to it. 'a' represent the width of boundary strip over which these modes live. It is the total width of compressible strips for a given integer filling fraction in CSG picture (16)

contact imposes a fluctuating potential across the full width of the edge, implying a coupling to charge mode. However, shot noise couples to both charge and soft modes. The decay rate of these edge-modes is dependent on the mode itself. Soft modes have faster decay rates than charge mode. Hence, due to this reason, our description of RF transmission through the edge channels by charge modes was sufficient. We did not have to invoke the other edge modes carrying our signal. Even though there are time-dependent transport measurements through 2D electron gas in quantum hall regime (27), where the soft modes have been observed by pulsating a voltage on a contact. The magnitude of the pulse used is of the order of 10 meV, which potentially provides a non-linear drive to the system.

For the case where one selectively excites single edge channel, coulomb interactions among these channels play an important role. There have been many studies, both in DC and RF transport that reveal the effect of these interactions. In DC transport regime, energy redistribution among edge channels (53; 69), dephasing of interferences in electronic mach-zehnder interferometer (73),(42) are few examples of interplay of interactions among co-propagating edge channels. They are described in the circuit model by a capacitor between these channels. There are some theoretical works (55),(23),(24; 56) and much more that have attempted to explain

dissipation, decoherence and energy relaxation seen in the above mentioned transport measurements. In RF transport regime, there is a seminal frequency resolved experimental work by Erwann Bocquillon et al. (11), where, by giving a RF signal to the outer channel through QPC, the signal from the inner channel was measured. They measured inter channel plasmon scattering matrix from this experiment. This results showed that due to coulomb interactions, the collective excitation at one of edge channel is decomposed into charge and neutral modes amongst the two co-propagating edge channels. These modes move with different velocities. They also observed the dissipation in the measured signal from inner channel, when frequency of excitation was increased. This dissipation was taken to be quadratic in frequency. Our noise measurements at both $\nu = 2$ and $\nu = 3$ provide new results regarding dissipation at high frequencies in edge channels. To our knowledge, such asymmetric dissipation with respect to the driven edge channel has never observed. Although we have seen a significant loss of noise power in inner-edge channel, it is true that we cannot say how much power, if any, is lost from outer edge channel. It is because we do not have an independent way to calibrate our noise RF chain. The noise temperature $T_N \simeq 9K$ as referred to the QPC output, obtained from outer channel noise is a bit higher than what has been previously measured in the experiments done in our dilution fridge with similar cryogenic RF circuitry. In the work (59), the noise temperature of 6-8K has been reported. Maybe the difference between this noise temperature and our noise temperature is the losses in outer edge channel. At this point, we do not have a better understanding. We believe that the description of RF transport by capacitively coupled edge channels is a good starting model. A modification would be to include coupling of edge channels to the bulk. We are currently trying a toy circuit model (see figure 5.21) of capacitively coupled edge channels which might qualitatively capture the observed loss of noise power. Here for $\nu = 2$, both edge channels are modelled as chiral transmission lines of $Z_C = R_K$. They are coupled to each other via a distributed capacitance per unit length C_x.

The coupling to the bulk is given by series RC circuit. Hopefully, it might explain our results. Let's see!

5.3.4 Summary

So, for the 3 probe setup, we found that noise power detected when driving the outer edge channel follows $\tau(1-\tau)$ dependence. We showed that the microwave coupling of the emitted noise to the detection circuit is independent of DC QPC transmission. This is due to the chirality. The reflected current fluctuations from either of the north or south contact are sent to on-chip ground due to chiral direction of transport. So there is no feedback of fluctuations of any sort on the quantum point contact. We calibrated the noise temperature of the cryogenic amplifier (assuming no losses in outer edge channel). With that we obtained the electron temperature from shot noise. We also observed losses in the measured noise power from partitioning of inner edge channel, both at $\nu = 2$ and $\nu = 3$ filling fractions. This lost of high frequency noise power challenge our understanding of dissipation that happens in edge channels.

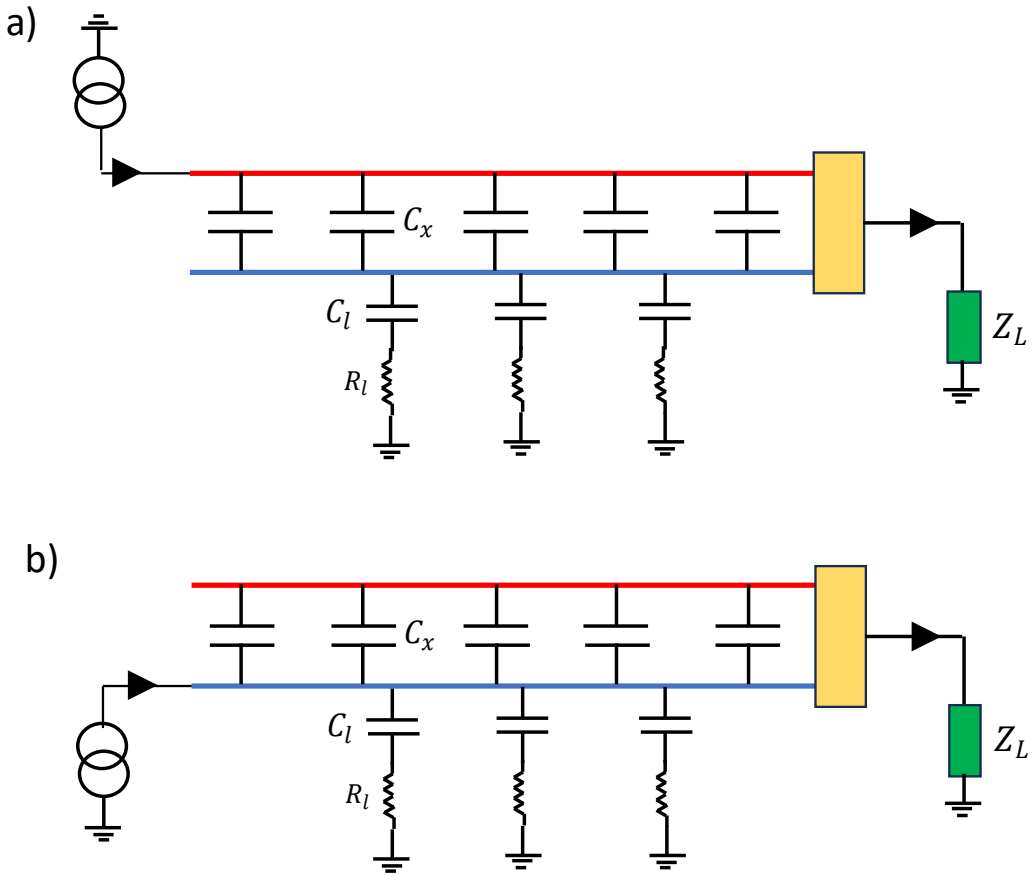

Figure 5.21: Toy circuit model for shot noise propagation through outer (shown in red) and inner (shown in blue) edge channel. Both channels are modelled as transmission lines with $Z_c = R_K$. They are coupled to each other by capacitance per unit length C_x. The inner edge channel is coupled with bulk via lossy capacitance and resistance per unit length. After traversing either of the channel, the noise signal then goes to load impedance Z_L (detection circuit) where noise power is measured. a) When noise signal is injected from QPC (shown as current source) to the outer edge channel. b) noise signal injection in inner edge channel

5.4 Noise in 2-Point configuration

When we set the side gates voltages to -0.4V, the connection of electron gas is cut from the on-chip grounds. In this configuration, the bias is applied through the inductive port of bias-tee, both from north and south sides,in differential mode, respectively (see figure 5.22). We again change both V_g and V_{dc} and measure 2-point differential resistance R_{2pt} and the noise through the resonators. For measuring noise, we have placed 2 cryo-amplifier on both detection lines, totaling 4 of them. The purpose here being to measure auto-correlation more accurately. Since, in this configuration, the resonators (electromagnetic environment) are in series with our coherent conductor (Quantum Point Contact), we expect noise feeding back to Quantum Point Contact. The power detected will, hence, depend on the QPC transmission and will also have a phase dependence due to propagation. Let's first derive these relations, as was done for three point configuration. Here as well, inner-edge

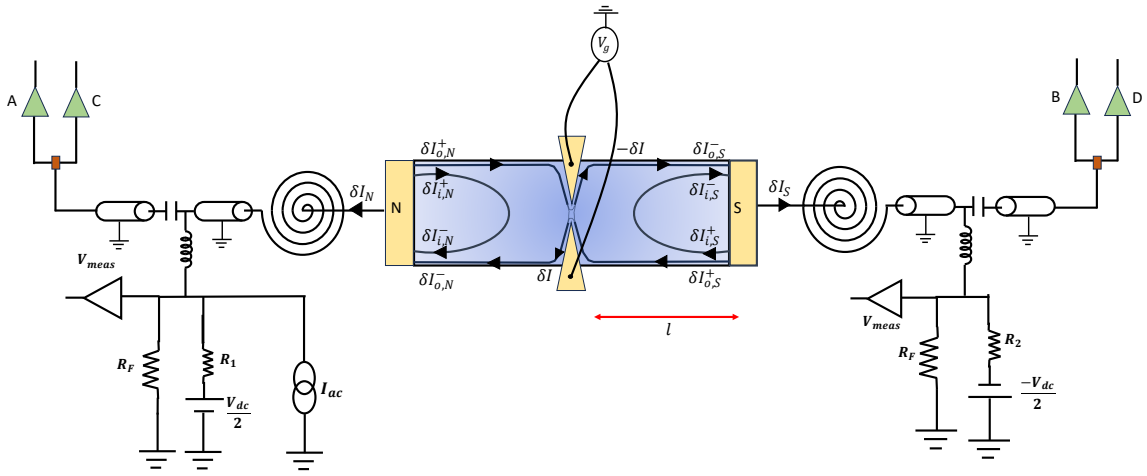

Figure 5.22: 2-point noise circuit: We do differential biasing across Quantum Point Contact. On the north side of the sample, a small current bias I_{ac} is applied via lock-in amplifier and voltage is measured. The bias resistor for lock-in is 99.1 MΩ (not shown here). The bias resistors R1 and R2 are 953M Ω and 960M Ω respectively. The resistors R_F to ground on each side are 12 kΩ. They help us to have a voltage bias. On RF side, we have two cryo-amps on each detection lines allowing us to measure the auto-correlation accurately. The splitting of emitted signal from sample into two lines is done by -3dB hybrid coupler (shown as brown square). Unfortunately, line C was disconnected during the run.

channel is fully pinched. Noise is generated by partitioning of outer-edge channel.

We use constitutive relations and current conservation rule at north and south contacts.

$$\begin{aligned}
\delta I^{+}_{o,N} &= G_K \delta V_N \\
\delta I^{+}_{i,N} &= G_K \delta V_N \\
\delta I^{+}_{o,S} &= G_K \delta V_S \\
\delta I^{+}_{i,S} &= G_K \delta V_S
\end{aligned} \tag{5.19}$$

$$\begin{aligned}
\delta I^{-}_{i,N} &= G_K e^{-i2\phi_i} \delta V_N \\
\delta I^{-}_{i,S} &= G_K e^{-i2\phi_i} \delta V_S
\end{aligned} \tag{5.20}$$

$$\begin{aligned}
\delta I^{-}_{o,N} &= (1-\tau) e^{-i2\phi_o} G_K \delta V_N + \tau e^{-i2\phi_o} G_K \delta V_S + \delta I_{bare} e^{-i\phi_o} \\
\delta I^{-}_{o,S} &= (1-\tau) e^{-i2\phi_o} G_K \delta V_S + \tau e^{-i2\phi_o} G_K \delta V_N - \delta I_{bare} e^{-i\phi_o}
\end{aligned} \tag{5.21}$$

$$\begin{aligned}
\delta I_N &= \delta I^{-}_{o,N} + \delta I^{-}_{i,N} - \delta I^{+}_{o,N} - \delta I^{+}_{i,N} \\
\delta I_S &= \delta I^{-}_{o,S} + \delta I^{-}_{i,S} - \delta I^{+}_{o,S} - \delta I^{+}_{i,S}
\end{aligned} \tag{5.22}$$

The set of equations presented in 5.20 and 5.21 convey the outgoing current fluctuations from the quantum point contact to the detection circuit at north and south locations (see figure 5.22). The term $G_K e^{-i2\phi_i} \delta V_N$ is the current fluctuation that after entering into the sample through inner channel from the contact at north, gets out of it with a phase accumulation $2\phi_i$. Here we see in this naive relations that at the contacts, the fluctuations feeding in are not only due to QPC, but also due to feedback. The noise signal travels roughly the same path '**l**' when traversing from QPC to ohmic contact or vice-versa through the edge channel on either side of the sample. Thus, the total phase accumulated from contact to contact is twice of that

accumulated in contact to QPC.

Substituting equations 5.20 and 5.21 in 5.22, we find that voltage fluctuations at north and south contact are opposite of each other, similar to what was obtained in 3-point configuration. Finally, we obtain the fluctuating current δI_N going to the north detection circuit as :

$$\delta I_N = \frac{\delta I_{bare} e^{-i\phi_o}}{1 + (2 - (1-2\tau)e^{-i2\phi_o} - e^{i2\phi_i})\,\frac{Z_{det}}{R_K}} \tag{5.23}$$

The power detected is thus given as:

$$\frac{\delta P}{P_{off}} = \frac{1}{k_B T_N} \frac{\langle \delta I^2_{bare} \rangle Re(Z_{det})}{|1 + (2 - (1-2\tau)e^{-i2\phi_o} - e^{i2\phi_i})\,\frac{Z_{det}}{R_K}|^2} \tag{5.24}$$

Both equations 5.23 and 5.24 contain in their denominator phase-factor due to propagation in inner-edge channel. Now, from the data of noise in 3pt-configuration of inner channel (see figure 5.10), we saw that there was attenuation in the emitted noise. In 3-point setup, the phase accumulated was only due to the distance traversed from quantum point contact to ohmic contact. Herein 2-point setup, due to the feedback the noise injected in inner-edge channel gets back to the contact by traversing twice the distance (that is why the term $2\phi_i$). In that case, the attenuation of the noise would be twice to that seen in 3pt-configuration. So, in the simple model, we neglect altogether the contribution of the noise signal via inner-edge channel which lead us to drop the term $e^{-i2\phi_i}$ from the equation 5.24. Hence, the equation becomes:

$$\frac{\delta P}{P_{off}} = \frac{1}{k_B T_N} \frac{\langle \delta I^2_{bare} \rangle Re(Z_{det})}{|1 + (2 - (1-2\tau)e^{-i2\phi_o})\,\frac{Z_{det}}{R_K}|^2} \tag{5.25}$$

Again, for large bias, the emitted noise is simply proportional to this bias which simplifies the expression for $\langle \delta I^2_{bare} \rangle$ as $\langle \delta I^2_{bare} \rangle = \frac{(eV_{dc} - hf)}{R_K}\tau(1-\tau)$. Summing equation 5.25 over frequency bandwidth will give us integrated noise power. We use it

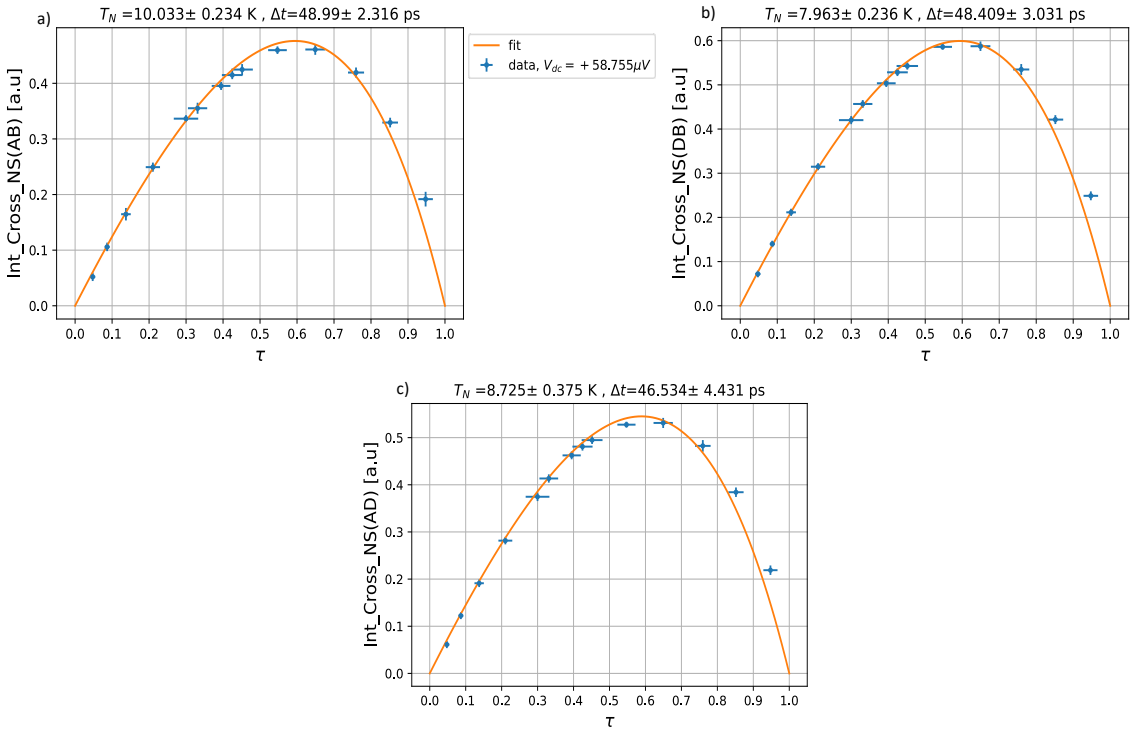

Figure 5.23: Integrated Noise power along with fits with $V_{dc} = 58.755\mu V$ for three cross-correlations which are named here as 'AB', 'AD' and 'DB' respectively.

to fit our measured data and obtain from there the values of noise temperature T_N and propagating time $\Delta t = \frac{\phi_o}{\omega}$.

Out of the 4 cryo-amplifiers used, the one named as 'C' was faulty. So, here we could only have three different cross-correlations instead of six. They are named as 'AB', 'AD' and 'DB', respectively. Among them 'DB' represents the auto-correlation of the south detection line (see figure 5.22). We present the data of these cross-correlations.

For the two bias values, the obtained noise temperature and the propagation time are same within error-bars for the given cross-correlation. The temperature values obtained is as referred to the sample. Now, we know that when the signal comes out of the sample and enters the detection chain, there will be some losses. Moreover, since we have hybrid coupler, it divides each detection line into two parts and splits the signal into half in amplitude [1].The amplifiers used have stated noise temperature of about 2-3 K. Due to this hybrid coupler the noise temperature cannot be

[1]In addition to that, it adds a constant phase of 90 degrees to the signal entering one of the branch with respect to other.

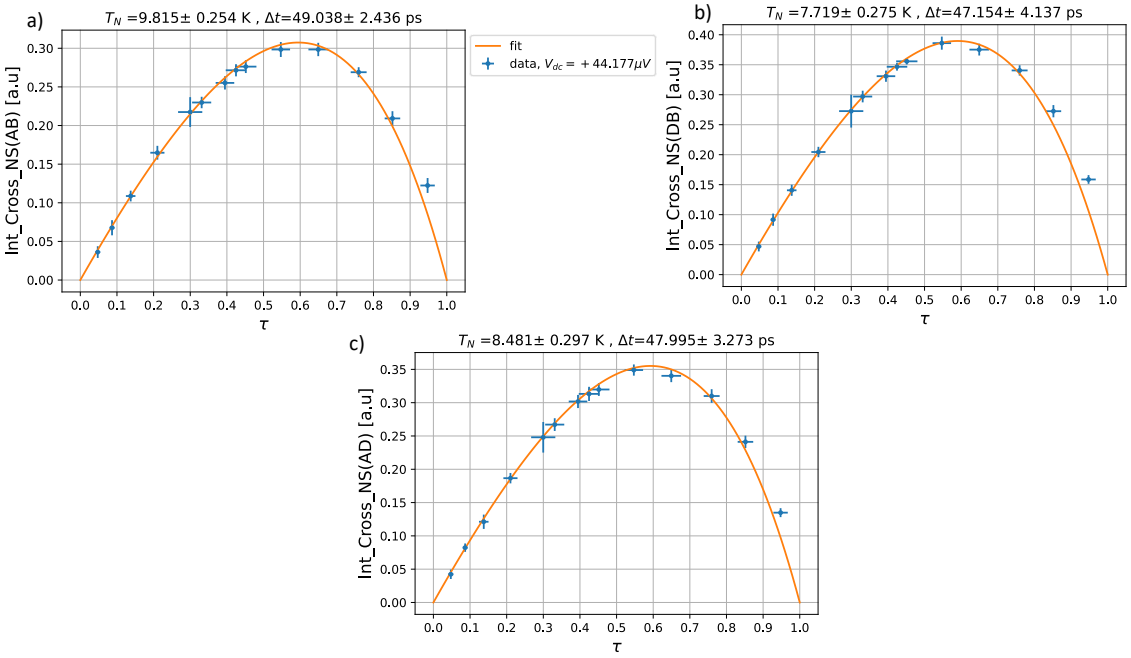

Figure 5.24: Integrated Noise power along with fits with $V_{dc} = 44.177\mu V$.

less than 4K. Our obtained value is between 8-10 K in close agreement with noise temperatures obtained in 3-point setup, implying that we loose half of the signal before it reaches hybrid coupler.

The obtained value of propagating time is in 48-46 picosecond range. The length traversed from the Quantum Point contact to the ohmic contact is $20\mu m$. This gives us the velocity of the travelling noise signal. it comes out to be $4.1 \times 10^5 ms^{-1}$. This is a bit faster than the one obtained from RF transmission studies done in the sample without using QPC (there it was $3.52 \times 10^5 ms^{-1}$ at $\nu = 2$, B=2.66T). We understand it as follows: the signal generated at the centre of QPC travels along the boundary of about $5\mu m$ in length which is gate defined (gate of the QPC). The capacitance to ground for a gate defined edge is smaller and hence its velocity is larger.

5.4.1 Discussion

In 2 point-configuration, we saw that due to classical feedback of current fluctuations onto the Quantum point contact, the fluctuations that enter the detection setup

depend on the DC transmission probability τ and also to the propagation phase. We used the information of dissipation of noise signal when it is injected into inner-edge channel and got a simple expression 5.25, where its phase contribution is neglected. If we were to compare equation 5.11 to equation 5.24, we can obtain the output impedance of the QPC. It is given as:

$$Z_{QPC} = \frac{R_K}{\left(1 - \frac{(1-2\tau)e^{-i2\phi_o}}{2}\right)} \tag{5.26}$$

This is so because the detection impedance is now $2Z_{det}$, since both resonators are in series with QPC and current noise injected to north contact is negative to that injected in south contact. Now one can imagine a similar sample but whose mesa size is very small, such that propagation phases, both for inner and outer edge channel are negligible. In that case, we might use the full expression of 5.23 and obtain output impedance as:

$$Z_{QPC} = \frac{R_K}{\left(1 - \frac{(1-2\tau)e^{-i2\phi_o} - e^{-i2\phi_i}}{2}\right)} \tag{5.27}$$

What our findings show that output impedance can change depending upon length of the device. This is more in the sense that one needs to consider the feedback contribution to outgoing current fluctuations by the inner-edge channel. A detailed study of dissipation seen in noise through inner edge channel is needed. Perhaps testing samples of various length is a way to go. In this way, formula 5.27 can be thoroughly checked.

Also, the observed deviation of detected noise in this configuration resembles very closely to the theoretical prediction of third cumulant correction of Shot noise (30). This is due to the Quantum back-action effects of resonator (electromagnetic environment) onto the QPC (coherent quantum conductor). Under this effect the

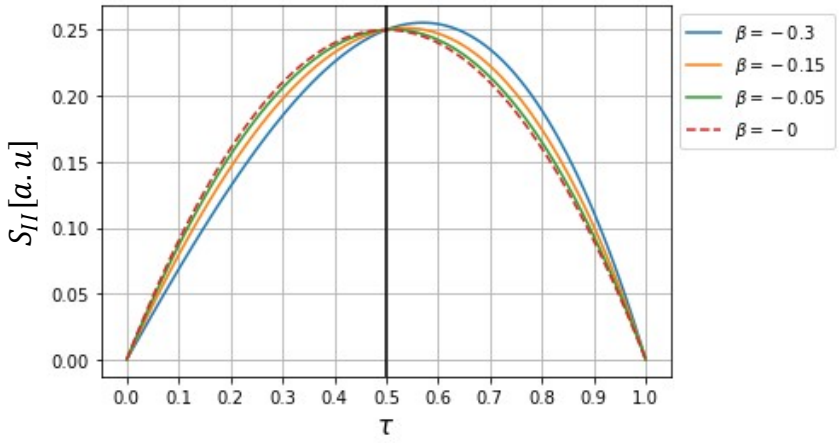

Figure 5.25: Modified emitted shot noise (5.28) as a function of transmission for various β values. We see that for negative values of β the noise is larger for transmissions larger than 0.5. It is similar to our measured noise power. However, in this plot the microwave coupling α is assumed to be constant.

modified bare shot noise emitted from the QPC is written as (30):

$$S_{II}(\tau) = \alpha[\tau(1-\tau) + \beta\tau(1-\tau)(1-2\tau)] \tag{5.28}$$

where β indicates the strength of the back-action effect due to quantum fluctuations of external impedance. This correction increases emitted noise for transmission larger than 0.5 and decreases it for transmission values less than 0.5. This implies that $\beta < 0$. α is the microwave coupling term. If we plot the above formula with constant α, we obtain curves for different values of β (figure 5.25). From our microwave coupling analysis we found that α is not constant but depends upon propagation phase and transmission. By assuming standard expression for emitted noise along with this coupling, we were able to produce our measured results with values of phase consistent with RF transmission measurements. These propagation effects itself produce deviation of noise which resembles to modified emitted noise. At this point we cannot conclude that these effects are absent in our measurements. In order to observe such fine effect, a short mesa size is needed which can get rid of propagation effects. For short mesa, the output impedance of QPC would lead to

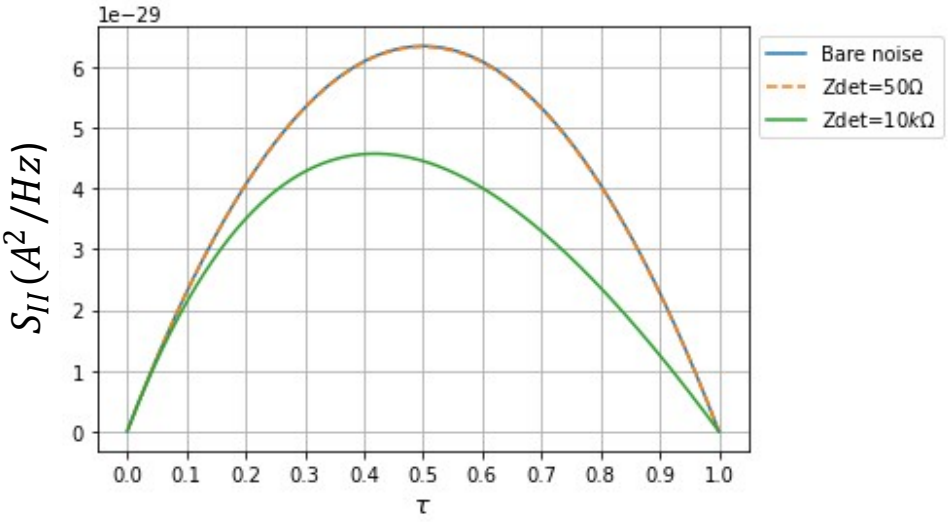

Figure 5.26: Noise power as function of transmission for short mesa sample. Here the output impedance of QPC is $\frac{R_K}{\tau}$. With detection impedance of 50 Ω we see that detected noise is same as emitted bare noise. However, for large detection impedance($\sim 10k\Omega$), detected noise tilts towards transmission values lower than 0.5.

following transmitted fluctuations into detection circuit:

$$S_{II}^t = S_{II} \left| \frac{\frac{R_K}{\tau}}{Z_{det} + \frac{R_K}{\tau}} \right|^2 \tag{5.29}$$

Plotting the noise power using above expression for detection impedance of 50 Ω and 10 $k\Omega$ (figure 5.26), we see that for large detection impedance, noise power is tilted to transmission values smaller than 0.5. If we were to observe these back-action effects on short mesa sample, we need to see the deviation from the green curve in figure 5.26. That being said, we do observe quantum back-action effects in our current sample on the differential conductance in 2 probe configuration (see next chapter for details).

Chapter 6

Quantum Back-Action

In the previous chapter, we studied the impedance composition laws that taught us about how RF-transmission is coupled through the sample and how much Shot noise is detected by resonators. It was all thanks to the high impedance nature of these resonators that made us resolve these measurements with decent signal to noise ratio and thus allowing us to perform them in linear response regime. This high impedance nature of these resonators also means that they have large quantum zero-point motion of the voltage at the contact that connects them to the electron gas. In the quantum Hall regime, since there are edge-states having resistance of $25.8k\Omega$, this mesoscopic circuit arrangement thus, provide us a way of coupling a high-impedance environment to a single quantum channel. The single quantum channel is obtained by partitioning the edge-channel via Quantum Point contact. For this we work at $\nu = 2$ and study this effect by partitioning outer edge channel. This quantum effect of the external environment on the transport properties of conductor (tunnel junction, Quantum point contacts, Quantum dots etc.) is called as Dynamical Coulomb Blockade.

6.1 Introduction

When a Quantum conductor, like a tunnel junction is placed in an electrical circuit (referred in literature as an Environment), one observes the reduction of the low-bias conductance of conductor. This effect is known as Environmental or Dynamical Coulomb Blockade and arises in conductors with very small capacitance such that they have large charging energy:

$$E_C = \frac{e^2}{2C} \tag{6.1}$$

In order to observe single electron charging effects the thermal energy of the electrons must be smaller than the charging energy $E_C << k_B T$, otherwise thermal fluctuations blur-out the blockade effect. For example: the charging energy $\frac{e^2}{2C}$ is about $1\text{K}\cdot k_B$ for a capacitance of $C \sim 1fF$. Thus these effects can be observed in dilution refrigerators for circuits having capacitances in the few 10s of fF. Depending upon whether the charge on the conductor is completely localised or it is discharging through the capacitance depends upon the impedance of the external circuit, these effects are termed as Static coulomb blockade or Dynamical coulomb Blockade respectively.

For the static coulomb effect, we can assume a quantum dot formed by two tunnel junctions. It is essentially an electrostatic island made by two series capacitances defined by the insulating layer of the tunnel junctions, yet electrons can tunnel in and out via the tunneling effect. As the electronic charge of the island is discrete, one can regard a tunneling current as a series of single electronic tunneling events assumed to be a weak perturbation to the island states. When an electron is transferred to the island, it increases its charge by an elementary charge and the biasing source thus needs to provide the electrochemical work of the single electron charging energy of the island $E_C = \frac{e^2}{2C}$, with C the sum of capacitances from the island to ground. Otherwise, for low biases $eV_{bias} < \frac{e^2}{2C}$, the electron transfer is blocked. The

observed conductance is zero.

It turns out that it is not even necessary to have an electrostatic island to block or reduce charge transport, indeed the dynamical Coulomb blockade (DCB) occurs when any mesoscopic conductor of finite transmission, for this example a NIN-junction, is placed in series with an electrical circuit having a finite dissipative admittance (26; 32)(see figure 6.1). If the conductor, that we represent as a normal tunneling

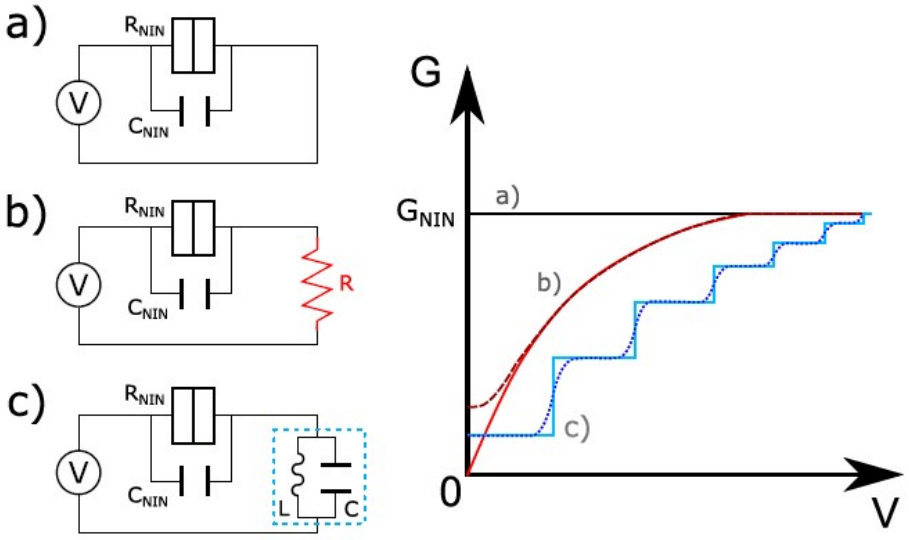

Figure 6.1: Illustration of the DCB effect for a tunnel junction in different electrical circuits: a) tunnel junction in a zero impedance biasing circuit; b) in series with a resistor; c) in series with a single LC resonator (1 EM-mode). The corresponding conductance curves are shown schematically for a) in black, for b) in red, for c) in blue. Solid lines illustrate the zero temperature limit, while dashed lines represent the finite, yet low, temperature behaviour where k_{BT} is much smaller than the characteristic energies of the environment: $E_{env} = \hbar/RC$ for (b) and $E_{env} = \hbar/\sqrt{LC}$ for (c).

element in parallel to its charging capacitance C, was in a perfect voltage biasing circuit (zero series impedance), the charge accumulated at the capacitor's plates after a tunneling event would immediately relax and not perturb the tunneling dynamics. If we now add a resistor with impedance $Z(f) \simeq R$ into the circuit environment, we introduce a finite life time $\tau_{RC} = RC$ for the electric influence field trapped within the plates of the capacitor. Whether the single electron charging energy is well defined with respect to this relaxation dynamics, depends on its corresponding

energy uncertainty $\delta E_{RC} = \frac{h}{\tau_{RC}}$.Thus single electron charging effects become relevant when $E_{RC} < E_C$, which is the case when $R > \frac{h}{e^2}$. It results in a suppression of the electronic transport similar to the static Coulomb blockade in the ideal case of zero temperature and small biases. This qualitative picture given above yields the right order of magnitude of the resistance necessary to observe sizeable reduction of the conductance at small but finite temperature: the conductance is not fully suppressed and also increases with the applied bias until the charging energy is reached and the blockade is lifted (36; 45).However, at zero temperature and bias voltage, the conductance is expected to vanish for any non-zero value of the series resistance In order to obtain a better microscopic picture, it is useful to exploit the Caldeira and Legget (15) representation of linear dissipative circuits as an ensemble of electromagnetic modes which is equivalent to a series of LC-resonators. Thus a macroscopic resistor is an infinite chain of resonators with different frequencies so that the resistor is able to absorb photons at any energy. Within this picture, the DCB corresponds to inelastic tunneling, i.e. tunneling electrons may spontaneously emit a number of photons into their environment. We illustrate this in figure 6.1: In situation a), for a perfectly shunted tunnel junction, all electrons tunnel elastically. However in situation b), when a resistor is added in series, electrons may tunnel inelastically with their energy being dissipated into the environment as a photon. Case b) in return implies that electrons can not pass the junction unless they carry the necessary energy to emit the photon, so that the conductance diminishes at low biases (dark red dashed line in figure 6.1) and vanishes at low temperature (red solid line in figure 6.1). When the circuit attached to the junction consists of a single resonator of frequency f, as shown in c), one can observe a similar suppression of the conductance that is also lifted for increasing bias voltages. Having only one resonator mode in the environment, inelastic processes are only possible if the electrons have energies that are multiples of the resonator's energy and thus the blockade release occurs step by step at bias values eV = n $\cdot$ hf. Hence one can observe plateaus for electronic

tunneling events with multiple photon emissions (see figure 6.1 (blue)). Yet again, as is the case for the resistor, the sharp step-profile is only obtainable close to zero temperature $k_BT << hf$. At finite temperature the steps will be smoothed by the thermal fluctuations.

6.2 DCB Effect for arbitrary transmission

The dynamic Coulomb blockade is well understood for the tunnel junction or any conductor where all electronic channels have a very small probability to be transmitted through the conductor ($\tau << 1$) (36), the reason for this is that in this limit the junction can be treated as a Hamiltonian perturbation to the circuit. At finite transmission however, there is no general theory that enables a prediction of the dynamics of an arbitrary quantum conductor embedded in an arbitrary linear circuit. Some models for finite transmission values τ were made for a weak impedance environment by Golubev (35) and Yeyati (80) in 2001 and Kindermann (47) in 2003, predicting a conductance suppression proportional to the shot noise reduction $F = (1-\tau)$. By now, their theories are experimentally tested by Cron et al. (20) and Altimiras et al. (2) for the weak blockade regime of a single channel of a QPC coupled to a different weak impedance environments. Later on, the experimental work was also extended to high impedance environments, the strong blockade regime, by Parmentier et al. (63) and Jezouin et al. (44). In (63), the conductance of QPC was studied both with bias and temperature for two different resistive environment having resistance of $13k\Omega$ and $26k\Omega$. The conductance in the presence of environment at any bias and temperature for any arbitrary transmission was found as:

$$G_{QPC}(V,T) = \frac{\tau_\infty}{R_K}\left(\frac{1+E_B(Z,V,T)}{1+\tau_\infty E_B(Z,V,T)}\right) \tag{6.2}$$

Here $E_B(Z,V,T) = \lim_{G_\infty\to\infty}\frac{\delta G}{G_\infty}$ is the relative change in the conductance for the tunnel junction embedded in the same environment as the Quantum Point contact.

τ_∞ is the bare transmission of the QPC when high impedance environment is not present or it is the value of the transmission measured at large biases or temperature ($eV, k_BT >> E_C$) where DCB effects gets washed out. This means, in particular, that the ratio of the relative change of conductance at zero bias to the bare conductance, which is the back-action correction to the conductance $\frac{\delta G}{G_\infty}$ is proportional to $(1 - R_K G_{QPC}(V,T))$ and not to $(1 - \tau_\infty)$, which is the case for low impedance environment. We here will study this effect on Quantum Point Contact having a high impedance LC circuit as an environment.

6.3 Experimental Conditions

We present here our experimental results of differential conductance of a Quantum Point Contact at $\nu = 2$, when the outer-edge channel is being pinched and setup is in two-point configuration. In this setup, both LC resonators are in series with Quantum Point Contact. So, the characteristic impedance of the total external circuit as seen from quantum point contact will be twice that of a single resonator. From the RF transmission lineshapes and noise spectra at $\nu = 2$, we have seen that resonance of the microwave resonators is close to 4.7 GHz. Using this and knowing that self resonance of the coil was at 5.5 GHz, we can deduce the modified characteristic impedance of the coil.

$$Z_c^{'} = Z_c \frac{f_0^{'}}{f_0} \tag{6.3}$$

Since $Z_c = 1k\Omega$, the modified characteristic impedance is 854.54Ω. So, the characteristic impedance of the environment is twice of that, which is $1.7k\Omega$. Resonant frequency of 4.7 GHz translates to the bias of $19.46\mu V$ via $eV = hf$ relation. The bias applied in the experiment ranges from $+60\mu V$ to $-60\mu V$ respectively. Thus, we have probed dynamical coulomb blockade effects up to 3 times this value in energy ($eV_{max} \simeq 3hf$). We do only a differential biasing scheme across QPC (see figure 6.2)

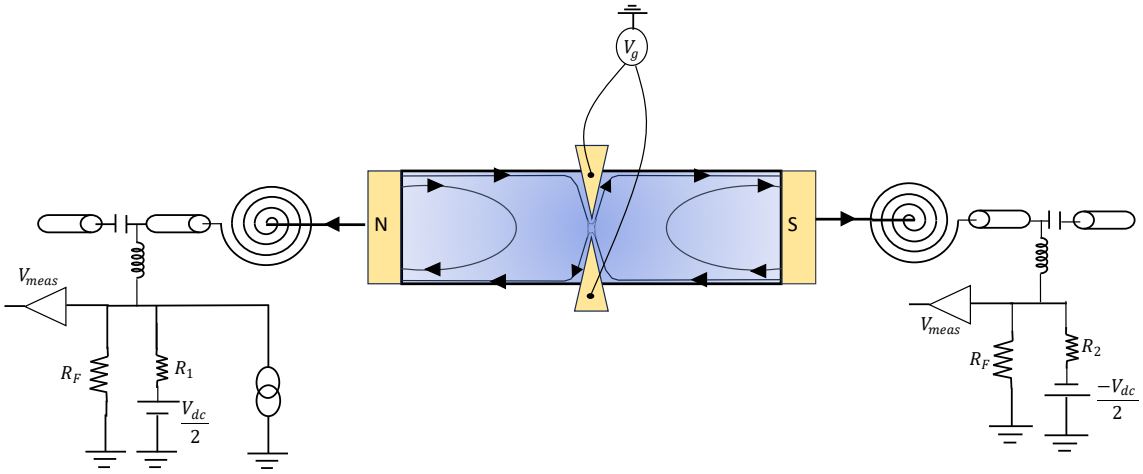

Figure 6.2: Circuit Illustration of the differential conductance measurement having two resonators in series with the Quantum Point contact. In this scheme we bias across QPC in differential mode via the inductive path of bias-tee. The resistors R1 and R2 are large bias resistors . Resistors R_F are of the order $6.2k\Omega$.

to minimize the effects due to the electrostatic dependence of the QPC transmission on the DC bias.

6.4 Observations and Results

We now present the experimental results. We show the dependence of the DC conductance on the applied bias for different QPC conditions (different gate voltage V_g values). From figure 6.3, we make following observations:

- there are dips in the value of conductance trace around zero bias value. Close to $\pm 20\mu V$, the conductance peaks for each QPC value.

- even though we are doing this measurement under differential bias, there still seems to be a slope as one goes from negative to positive bias, and that these slopes are somewhat dependent on the value of QPC at which bias trace is taken.

- There is nothing like a step shape profile of differential conductance for any given QPC value which one would expect from DCB effect due to a LC resonator. One would expect not a step-shape but rather something of that

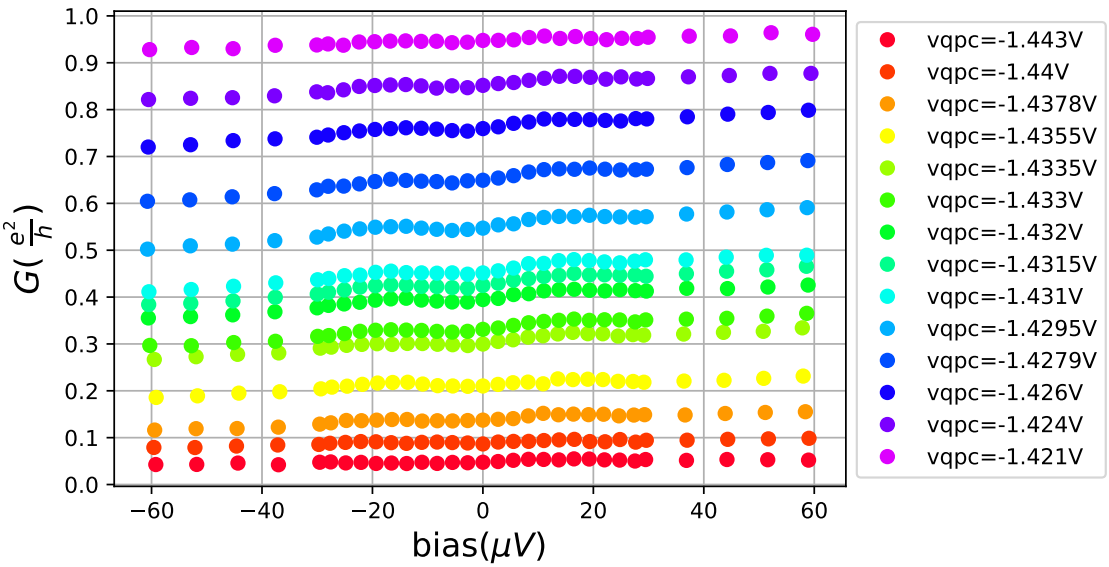

Figure 6.3: Dependence of the DC transmission of the outer edge channel on the applied bias for various values of QPC.

form that is smoothed by the effective temperature which consists of electron temperature and lock-in voltage used to measure the differential conductance.

Subtracting the slopes from the curve in the figure 6.3, we obtain the figure 6.4. One can see that there are dips in the conductance at zero bias, but also some bulges at around the value of bias close to $\pm 20\mu V$. To gain more insight, we take an interpolation of the data in figure 6.4 and plot the ratio of relative change of conductance to bare conductance G_∞ as a function of applied bias for all the QPC values. This bare conductance is what is measured for any QPC value at large bias (here at $\pm 60\mu V$, see figure 6.4). From figure 6.5, we see that at bias values $\pm 20\mu V$ the DCB correction to the conductance increases with decrease of the transmission measured at that value. But the increase is quite small; about 5 percent for the tunnel regime. If we were to estimate the reduction when the environment is a pure LC resonator having Z_c as mentioned above, then it is $1 - e^{\frac{-2\pi Z_c}{R_K}} \sim 0.2$, about 20 percent (65). This is clearly not the case.

Also, we note one curious observation of the dependence of the slope of dI/dV curves on zero bias transmission for each value of QPC. The result is plotted in the figure

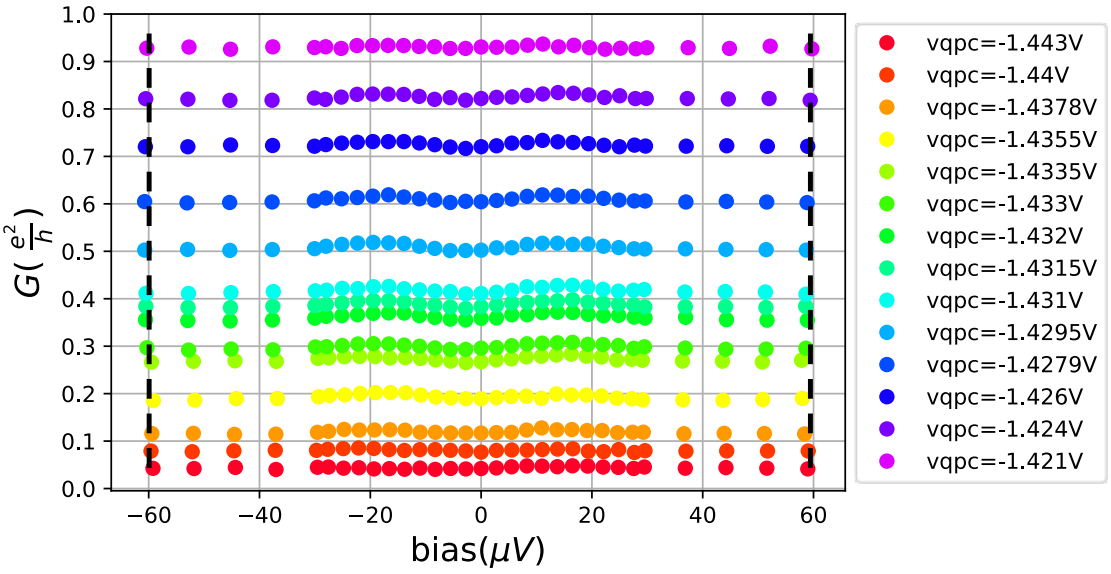

Figure 6.4: Plot after slope correction for each trace of transmission with bias. The dotted blacklines on either sides convey the bare transmission of QPC τ_∞.

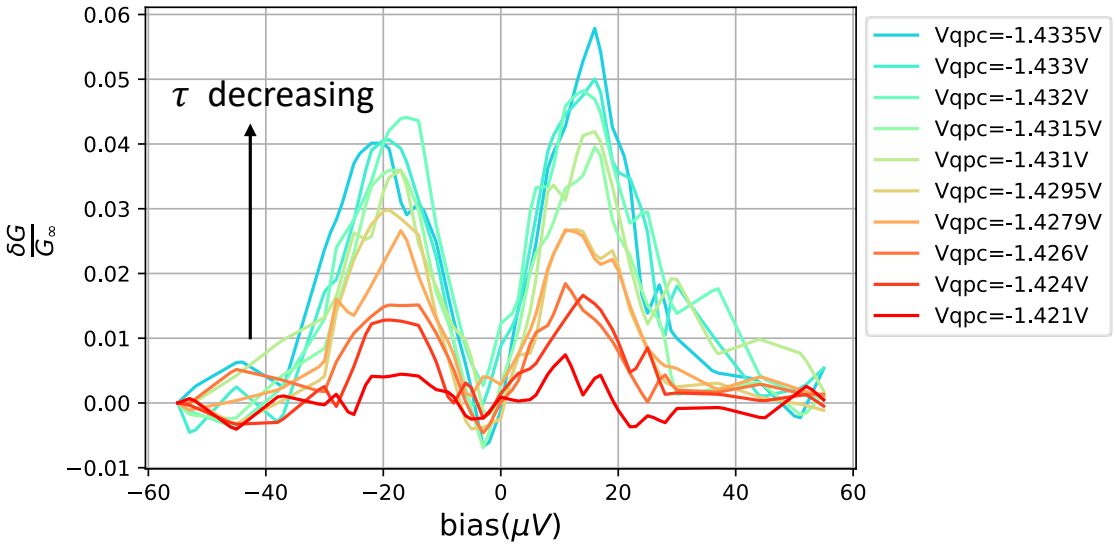

Figure 6.5: $\delta G/G_\infty$ plot as a function of bias applied. We see reduction of conductance at two bias values ($\pm 20\mu V$), symmetric about zero bias. The reduction increases more with decreasing transmission.

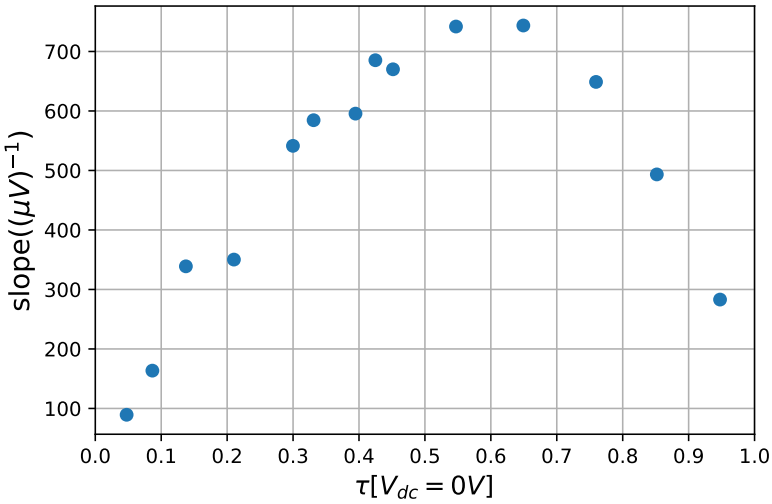

Figure 6.6: Dependence of the slope of differential conductance in fig 6.3 on transmission at zero bias. The curve looks like shot noise measured in 2 point setup.

6.6. The slope follows the trend which is much like the shot noise curves that we have measured in 2point-configuration. At this point, we are trying to understand it as well. Maybe, there is somehow a quantum back-action of noise on the I-V curve of QPC which produces this slope.

6.5 Discussion

We have tried to measure the DCB correction to the conductance of the QPC having two resonators in series with it. Naively, it would have gotten us about 20 percent reduction in the conduction. But it gave about 5-6 percent. Also, the relative reduction curves are not like we would expect for a LC resonator in a thermal state. The reductions are seen at bias values close to energy quantum of the LC resonator. Currently, we do not have any theory to explain our experimental results. However, one thing can be said about the nature of the environment as seen from the QPC. Since the electron gas in between QPC and resonator has a sizeable length, it means that there is an impedance transformation of the LC resonators done by the electron gas. We have seen from the RF transmission measurements how the phase propagation effects build up in electron gas and make it a impedance transformer.

It is not surprising that it is happening here as well. At this point we are working on it.

Chapter 7

Conclusions and Perspectives

In conclusion, this thesis highlights the study of RF transport through mesoscopic sample in Quantum Hall Regime. With the help of on-chip microwave resonators, we performed two main experiments: RF transmission through the device and RF Shot noise.

In RF transmission measurements done at zero magnetic field, we characterized our device (internal resistance of the coil, parasitic capacitance) and calibrated the gain of RF chain. Using this information we studied this transmission at finite magnetic fields. In the integer quantum hall regime the RF signal in the electron gas is carried along the edge states by low-energy collective excitation known as edge-magnetoplasmons. The transport through Edge-states at these frequencies was modelled as that in transmission lines, but uni-directional in nature. For integer filling fractions, edge channels were described as non-dissipative chiral transmission lines having characteristic impedance as Hall resistance. The edge-plasmons traversing along the edge acquire a propagation phase. Due to this, the electron gas in the quantum hall regime acts as an impedance transformer, with impedance transformation laws markedly different from the ones arising from the usual reciprocal transmission lines. Thanks to the formalism that we derived to understand these impedance transformations, we could model the transmission through the device

consisting of 2DEG in series with two large impedance RF resonators. By changing the magnetic field applied to the sample we found a linear dependence of velocity of Edge magnetoplasmons as a function of filling fraction at integer values. We then described RF transmission line shapes across the $\nu = 2$ plateau by modelling the transport as a dissipative transmission line where the dissipation is ohmic in nature. A possible physical picture here is that of leakage of the RF signal carried by edge excitation to the bulk of the sample (to the localised states) where it is dissipated. This leakage depends upon the magnetic field as one moves across the hall plateau. Our ohmic model of dissipation resulted in leakage conductance values in the range of 100 kΩ when we are away from the centre of the plateau. These values are not physical as it would have been seen in two-probe DC measurements. We have then used another phenomenological dissipation term which is quadratic in frequency. It physically describes a RC leakage coupling of the RF signal in the edge channel to the localised states in the bulk. The RC leakage time obtained is in few picoseconds in agreement with results obtained in (11). In all these measurements of RF transmission, the signal was injected into the full edge profile (their number depending upon filling fraction) from a galvanically connected contact. So, we expect to couple predominantly to the charge mode(1) whose density oscillations are strictly along the edge. This charge mode's leakage across various hall plateaus gives us the non-monotonous trend of S21 amplitudes.

Next, we investigated the RF Shot noise emitted by a DC biased QPC predominately at the centre of the $\nu = 2$ plateau, primarily in two different circuit configurations. In the first one, known as the three-probe scheme, we found out current division rules, giving the fraction of the emitted noise which couples to the detection circuit. The current division factor depends on the hall resistance and on the impedance of the detection circuit. It is, therefore, independent of QPC transmission. For the noise emitted by partitioning outer edge channel, we calibrated the RF noise chain by determining the noise temperature of cryo amplifiers. However, the noise emitted

from the partitioning of inner edge channel had surprises. The corresponding detected noise power was found to be 70 percent lower with respect to the one emitted from the outer edge channel. This, to our knowledge is the first measurement of its kind where such a loss of RF noise power is seen. Similar measurements were also performed at $\nu = 3$ and it was found that noise detected when driving the inner-most channel was again 70 percent lower than when driving the outermost edge channel. Since with the help of QPC we can selectively drive a RF noise signal into different edge channels, we could observe that even at the centre of the quantum hall plateau dissipation of the RF signal can occur. While our data shows unambiguously that driving the innermost edge channel give rise to large losses as compared to when driving the outer edge channel, we could not make a quantitative analysis of the signal coupled when driving the outer channel. Comparison of the noise temperature as referred to the output of QPC with that measured in a similar setup with tunnel junctions makes us, nevertheless, confident that losses in outer edge channel are smaller than 20 percent. For RF transmission measurements, the plasmon propagation at the centre of Hall plateau was found to propagate without losses, opposite to what is seen in noise measurements. When QPC selectively drive a RF signal into either outer or inner edge channel, the excited chiral plasmons are, nevertheles, coupled to each other by Coulomb interactions. In this way, perhaps a basic description of losses in the measured noise power can be provided by assuming coupled transmission line circuit, where the inner channel has a RC coupling to the bulk. In the second setup, the two-probe configuration, the QPC was set in series with resonators. In this case, the detected noise showed strong deviations from 3-point configuration, where it scaled canonically as $\tau(1-\tau)$. This deviation has been predicted to be the quantum back-action correction of noise due to environment (30), but the observed effect was way larger than expected. We found that due to the phase accumulated by plasmon propagation, the output impedance of the QPC is a complicated function of propagation phase and DC QPC transmission.

If one assumes the standard shot noise dependence on transmission ($\tau(1-\tau)$), the detected noise power resulting from τ current division factor leads to a different τ dependence as compared to the emitted noise. This formulation reproduces our data with propagation phase values agreeing closely to those that we obtained from the RF transmission measurements through the hall bar. However, it doesn't rule out any quantum back-action correction to the noise. The coupled noise signal is predominately affected by impedance transformation effect which we could not characterize on 10 percent level needed to disentangle classical and quantum back-action effects. The propagation effects due to moderate length ($l \sim 30\mu m$) of the mesa turn out to be more prominent.

Lastly, we have measured the back-action on differential conductance in the two-probe setup. We do observe an intriguing QPC dependence of differential conductance in two-point setup, not seen in 3-point setup. The deviation of the conductance from its asymptotic value at large bias is larger for lower transmission values, as expected from predictions. Qualitatively, this results are in line with the predictions in (47), but a detailed theory has yet to be established. Here, we suspect the impedance as observed from QPC to ground is not that of LC oscillator but rather transformed by the intervening mesa structure. On top of it, since the classical back-action is strong (as seen from noise measurements in two-point configuration), it means that state of the resonators cannot be assumed as a simple gaussian bath.

Therefore, this experimental work has paved a new way of understanding dynamical transport in Quantum Hall regime and brought exciting new questions that we hope will lead to more detailed understanding of the underlying physics at play.

7.1 Perspectives

With the experiments done, we learned new things. First, high frequency shot noise came out to be a new tool to probe dissipation in Quantum Hall regime. To the

best of our knowledge, the loss of noise power in inner edge channel as compared to outer edge channel is not observed in low-frequency noise measurements (typically measured around 2-3 MHz), neither when integrating the full energy flux carried by the edge channel (53). The high frequency plasmons that carry the noise signal when driving the inner-most edge channel show unambiguously more dissipation than when driving the outer edge channel. To understand these dissipation effects, further work is needed. This will also help to understand more the way different edge channel are coupled with each other and with the bulk. Heat transport measurements can be employed to check whether these losses are dissipated as heat in the bulk or simply redistributed within the edge channels at lower frequencies.

Second, in order to observe quantum back-action effects on shot noise, we need a shorter mesa size. This will help get rid of phase propagation effects. But, one needs to think on the parasitic capacitance between resonators that can shunt the QPC (it is about 1 fF in the present sample), since now they will be more closer to each other. So, a careful thought on designing the device is needed.

Lastly, the three-probe circuit scheme in our device can already be used to probe the statistics of the photons emitted in the detection circuit by the electronic shot noise. Here the resonators only acts as a receiving antenna for the emitted noise and no fluctuations feedback to quantum point contact. With all these properties, one can finally perform experiments to see whether the emitted photons show anti-bunching effects or not, as predicted in (9),(8).

Appendix A

Appendix

A.1 Gain of the RF-Chain

Knowing the DC two-point resistance to ground and substituting it as the Impedance in between the resonators, one can get the fit from the model. This gives us the Gain of the chain **G**.

The gain **G** tells us about the net amplification RF-signal gets when it traverses through the full microwave chain of elements, starting from port 1 of V.N.A, going through the sample and coming back to port 2. This Gain is frequency dependent and is different when one moves slightly in frequency space. This is because transfer functions (S21 specs) of microwave components are not fully flat in frequency space, there are standing waves formed due to the impedance mismatch that happens when connecting two-cables as connections are never perfect and there are insertion losses due to the finite length traversed by the signal plus some deliberate insertion of dissipation elements into the microwave chain.

A.2 Phase of the cavity filter

Here we present the phase of the cavity filter and the delay time, which is computed as $\frac{d\phi}{df}$. As can be seen from the figure A.1 at the band edge of the filter response

(close to 4 GHz and 8 GHz), the delay time is not linear with frequency. It therefore, adds significant distortion to the net phase measured by V.N.A then any other microwave component given the fact that for RF transmission measurement setup, three of these filters are used. So, we remove three times the phase of this filter from the measured phase.

The measurement presented in A.1 are taken at room temperature and it is assumed that all the three filters are more or less identical in specifications. And that features at cryogenic temperatures are not that different for the phase than at room temperature even though it is known that filter's length contracts when cooled.

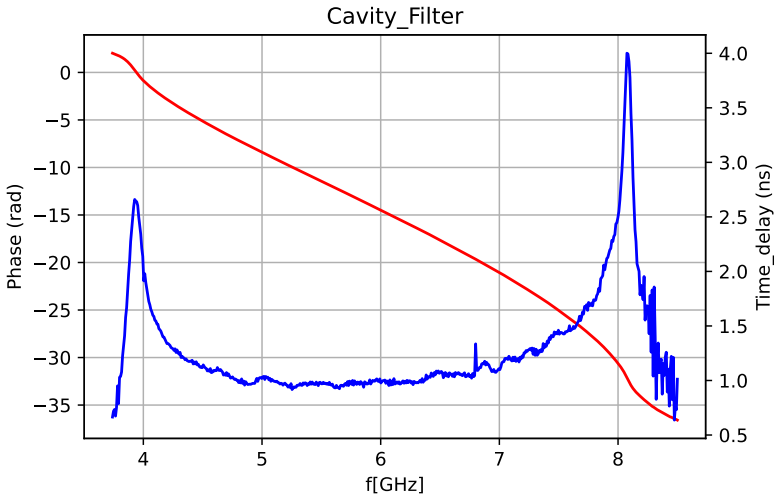

Figure A.1: Phase (shown in red and the delay time (shown in blue) of 4-8 GHz cavity filter. In our setup we use three of them (two in the mixing chamber of the fridge and one on room temperature RF chain)

Bibliography

[1] I. L. Aleiner and L. I. Glazman. Novel edge excitations of two-dimensional electron liquid in a magnetic field. *Phys. Rev. Lett.*, 72:2935–2938, May 1994.

[2] C. Altimiras, U. Gennser, A. Cavanna, D. Mailly, and F. Pierre. Experimental test of the dynamical coulomb blockade theory for short coherent conductors. *Phys. Rev. Lett.*, 99:256805, Dec 2007.

[3] C. Altimiras, H. le Sueur, U. Gennser, A. Cavanna, D. Mailly, and F. Pierre. Non-equilibrium edge-channel spectroscopy in the integer quantum hall regime. *Nature Physics*, 2010.

[4] P. Armagnat and X. Waintal. Reconciling edge states with compressible stripes in a ballistic mesoscopic conductor. *J. Phys. Mater. 3 02LT01*, 2020.

[5] R. C. Ashoori, H. L. Stormer, L. N. Pfeiffer, K. W. Baldwin, and K. West. Edge magnetoplasmons in the time domain. *Phys. Rev. B*, 45:3894–3897, Feb 1992.

[6] J. Basset. *High Frequency Quantum Noise of mesoscopic systems and current-phase relation of hybrid junctions.* PhD thesis, Laboratoire de Physique des Solides, Orsay, 2011.

[7] C. Beenakker and H. V. Houten. Quantum transport in semiconductor nanostructures. *arXiv:cond-mat/0412664*, 1991.

[8] C. W. J. Beenakker and H. Schomerus. Counting statistics of photons produced by electronic shot noise. *Phys. Rev. Lett.*, 86:700–703, Jan 2001.

[9] C. W. J. Beenakker and H. Schomerus. Antibunched photons emitted by a quantum point contact out of equilibrium. *Phys. Rev. Lett.*, 93:096801, Aug 2004.

[10] R. Bisognin, H. Bartolomei, and M. e. a. Kumar. Microwave photons emitted by fractionally charged quasiparticles. *Nat Commun 10, 1708*, 2019.

[11] E. Bocquillon and et al. Separation of neutral and charge modes in one-dimensional chiral edge channels. *Nat Commun 4, 1839 (2013). https://doi.org/10.1038/ncomms2788.*

[12] P. J. Burke, I. B. Spielman, J. P. Eisenstein, L. N. Pfeiffer, and K. W. West. High frequency conductivity of the high-mobility two-dimensional electron gas. *Applied Physics Letters*, 2000.

[13] M. Büttiker. Absence of backscattering in the quantum hall effect in multiprobe conductors. *Phys. Rev. B*, 38:9375–9389, Nov 1988.

[14] M. Büttiker. Quantized transmission of a saddle-point constriction. *Phys. Rev. B*, 41:7906–7909, Apr 1990.

[15] A. Caldeira and A. Leggett. Quantum tunnelling in a dissipative system. *Annals of Physics*, 149(2):374–456, 1983.

[16] D. B. Chklovskii, B. I. Shklovskii, and L. I. Glazman. Electrostatics of edge channels. *Phys. Rev. B*, 46:4026–4034, Aug 1992.

[17] T. Christen and M. Büttiker. Low frequency admittance of a quantum point contact. *Phys. Rev. Lett.*, 77:143–146, Jul 1996.

[18] T. Christen and M. Büttiker. Low-frequency admittance of quantized hall conductors. *Phys. Rev. B*, 53:2064–2072, Jan 1996.

[19] A. A. Clerk, M. H. Devoret, S. M. Girvin, F. Marquardt, and R. J. Schoelkopf. Introduction to quantum noise, measurement, and amplification. *Rev. Mod. Phys.*, 82:1155–1208, Apr 2010.

[20] R. Cron, M. F. Goffman, D. Esteve, and C. Urbina. Multiple-charge-quanta shot noise in superconducting atomic contacts. *Phys. Rev. Lett.*, 86:4104–4107, Apr 2001.

[21] M. P. da Silva, D. Bozyigit, A. Wallraff, and A. Blais. Schemes for the observation of photon correlation functions in circuit qed with linear detectors. *Phys. Rev. A*, 82:043804, Oct 2010.

[22] R. de Picciotto, M. Reznikov, M. Heiblum, V. Umansky, G. Bunin, and D. Mahalu. Direct observation of a fractional charge. *Nature*, 1997.

[23] P. Degiovanni, C. Grenier, and G. Fève. Decoherence and relaxation of single-electron excitations in quantum hall edge channels. *Phys. Rev. B*, 80:241307, Dec 2009.

[24] P. Degiovanni, C. Grenier, G. Fève, C. Altimiras, H. le Sueur, and F. Pierre. Plasmon scattering approach to energy exchange and high-frequency noise in $\nu = 2$ quantum hall edge channels. *Phys. Rev. B*, 81:121302, Mar 2010.

[25] M. Devoret. Quantum fluctuations in electrical circuits. *Fluctuations Quantiques / Quantum Fluctuations: Les Houches Session LXIII, June 27 - July 28, 1995. A UJFG / a NATO Advanced Study Institute conference. Edited by S. Reynaud, E. Giacobino and J. Zinn-Justin. ISBN 0444-82593- 2. Published by Elsevier, Amsterdam, The Netherlands, 1997, p.351*, 1997.

[26] M. H. Devoret, D. Esteve, H. Grabert, G.-L. Ingold, H. Pothier, and C. Urbina. Effect of the electromagnetic environment on the coulomb blockade in ultrasmall tunnel junctions. *Phys. Rev. Lett.*, 64:1824–1827, Apr 1990.

[27] G. Ernst, R. J. Haug, J. Kuhl, K. von Klitzing, and K. Eberl. Acoustic edge modes of the degenerate two-dimensional electron gas studied by time-resolved magnetotransport measurements. *Phys. Rev. Lett.*, 77:4245–4248, Nov 1996.

[28] J. Gabelli, G. Fève, T. Kontos, J.-M. Berroir, B. Placais, D. C. Glattli, B. Etienne, Y. Jin, and M. Büttiker. Relaxation time of a chiral quantum $r-l$ circuit. *Phys. Rev. Lett.*, 98:166806, Apr 2007.

[29] J. Gabelli, G. Fève, J.-M. Berroir, B. Plaçais, A. Cavanna, B. Etienne, Y. Jin, and D. C. Glattli. Violation of kirchhoff's laws for a coherent rc circuit. *Science*, 313(5786):499–502, 2006.

[30] A. V. Galaktionov, D. S. Golubev, and A. D. Zaikin. Current fluctuations and electron-electron interactions in coherent conductors. *Phys. Rev. B*, 68:085317, Aug 2003.

[31] U. Gavish, Y. Levinson, and Y. Imry. Detection of quantum noise. *Phys. Rev. B*, 62:R10637–R10640, Oct 2000.

[32] S. M. Girvin, L. I. Glazman, M. Jonson, D. R. Penn, and M. D. Stiles. Quantum fluctuations and the single-junction coulomb blockade. *Phys. Rev. Lett.*, 64:3183–3186, Jun 1990.

[33] S. M. Girvin and R. E. Prange. *The Quantum Hall Effect*. Springer New York, NY, 1987.

[34] D. C. Glattli, E. Y. Andrei, G. Deville, J. Poitrenaud, and F. I. B. Williams. Dynamical hall effect in a two-dimensional classical plasma. *Phys. Rev. Lett.*, 54:1710–1713, Apr 1985.

[35] D. S. Golubev and A. D. Zaikin. Coulomb interaction and quantum transport through a coherent scatterer. *Phys. Rev. Lett.*, 86:4887–4890, May 2001.

[36] H. Grabert and M. Devoret. *Single Charge Tunneling: Coulomb Blockade Phenomenon in Nanostructures*. Springer, 1991.

[37] I. Grodnensky, D. Heitmann, and K. von Klitzing. Nonlocal dispersion of edge magnetoplasma excitations in a two-dimensional electron system. *Phys. Rev. Lett.*, 67:1019–1022, Aug 1991.

[38] E. H. Hall. On a new action of the magnet on electric currents. *American Journal of Mathematics, vol. 2, no. 3, 1879, pp. 287–292.*

[39] B. I. Halperin. Quantized hall conductance, current-carrying edge states, and the existence of extended states in a two-dimensional disordered potential. *Phys. Rev. B*, 25:2185–2190, Feb 1982.

[40] M. Hashisaka, H. Kamata, N. Kumada, K. Washio, R. Murata, K. Muraki, and T. Fujisawa. Distributed-element circuit model of edge magnetoplasmon transport. *Phys. Rev. B*, 88:235409, Dec 2013.

[41] M. Hashisaka, K. Washio, H. Kamata, K. Muraki, and T. Fujisawa. Distributed electrochemical capacitance evidenced in high-frequency admittance measurements on a quantum hall device. *Phys. Rev. B*, 85:155424, Apr 2012.

[42] P.-A. Huynh, F. Portier, H. le Sueur, G. Faini, U. Gennser, D. Mailly, F. Pierre, W. Wegscheider, and P. Roche. Quantum coherence engineering in the integer quantum hall regime. *Phys. Rev. Lett.*, 108:256802, Jun 2012.

[43] T. Ihn. *Semiconductor Nanostructures*. Oxford University Press, 2010.

[44] S. Jezouin, M. Albert, F. D. Parmentier, A. Anthore, U. Gennser, A. Cavanna, I. Safi, and F. Pierre. Tomonaga-luttinger physics in electronic quantum circuits. *Nature Communcations*, 2013.

[45] P. Joyez and D. Esteve. Single-electron tunneling at high temperature. *Phys. Rev. B*, 56:1848–1853, Jul 1997.

[46] H. Kamata, T. Ota, K. Muraki, and T. Fujisawa. Voltage-controlled group velocity of edge magnetoplasmon in the quantum hall regime. *Phys. Rev. B*, 81:085329, Feb 2010.

[47] M. Kindermann and Y. V. Nazarov. Interaction effects on counting statistics and the transmission distribution. *Phys. Rev. Lett.*, 91:136802, Sep 2003.

[48] K. v. Klitzing, G. Dorda, and M. Pepper. New method for high-accuracy determination of the fine-structure constant based on quantized hall resistance. *Phys. Rev. Lett.*, 45:494–497, Aug 1980.

[49] N. Kumada, H. Kamata, and T. Fujisawa. Edge magnetoplasmon transport in gated and ungated quantum hall systems. *Phys. Rev. B*, 84:045314, Jul 2011.

[50] N. Kumada, P. Roulleau, B. Roche, M. Hashisaka, H. Hibino, P. I., and D. C. Glattli. Resonant edge magnetoplasmons and their decay in graphene. *Phys. Rev. Lett.*, 113:266601, Dec 2014.

[51] A. Kumar, L. Saminadayar, D. C. Glattli, Y. Jin, and B. Etienne. Experimental test of the quantum shot noise reduction theory. *Phys. Rev. Lett.*, 76:2778–2781, Apr 1996.

[52] R. B. Laughlin. Quantized hall conductivity in two dimensions. *Phys. Rev. B*, 23:5632–5633, May 1981.

[53] H. le Sueur, C. Altimiras, U. Gennser, A. Cavanna, D. Mailly, and F. Pierre. Energy relaxation in the integer quantum hall regime. *Phys. Rev. Lett.*, 105:056803, Jul 2010.

[54] G. Lesovik and R. Loosen. On the detection of finite frequency current fluctuations. *JETP*, 1997.

[55] I. P. Levkivskyi and E. V. Sukhorukov. Dephasing in the electronic mach-zehnder interferometer at filling factor $\nu = 2$. *Phys. Rev. B*, 78:045322, Jul 2008.

[56] I. P. Levkivskyi and E. V. Sukhorukov. Energy relaxation at quantum hall edge. *Phys. Rev. B*, 85:075309, Feb 2012.

[57] T. Martin and R. Landauer. Wave-packet approach to noise in multichannel mesoscopic systems. *Phys. Rev. B*, 45:1742–1755, Jan 1992.

[58] D. B. Mast, A. J. Dahm, and A. L. Fetter. Observation of bulk and edge magnetoplasmons in a two-dimensional electron fluid. *Phys. Rev. Lett.*, 54:1706–1709, Apr 1985.

[59] G. C. Ménard, A. Peugeot, C. Padurariu, C. Rolland, B. Kubala, Y. Mukharsky, Z. Iftikhar, C. Altimiras, P. Roche, H. le Sueur, P. Joyez, D. Vion, D. Esteve, J. Ankerhold, and F. Portier. Emission of photon multiplets by a dc-biased superconducting circuit. *Phys. Rev. X*, 12:021006, Apr 2022.

[60] J. Mueller. *Finite Frequency dynamics in correlated Quantum Conductors*. PhD thesis, Universite Paris-Saclay, 2020.

[61] N.Ashcroft and N.Mermin. *Solid State Physics*. Saunders College Publishing, Fort Worth, 1976.

[62] Y. Nazarov and Y. Blanter. *Quantum Transport*. Cambridge University press, 2009.

[63] F. D. Parmentier, A. Anthore, S. Jezouin, H. le Sueur, U. Gennser, A. Cavanna, D. Mailly, and F. Pierre. Strong back-action of a linear circuit on a single electronic quantum channel. *Nature Physics*, 2011.

[64] A. Peugeot. *Quantum microwave sources from inelastic Cooper pair tunneling*. PhD thesis, Universite Paris Saclay, 2020.

[65] H. Pothier. *Coulomb Blockade and transfer of electrons one by one*. PhD thesis, Quantronics group, CEA-Saclay, 1990.

[66] D. Pozar. *Microwave Engineering*. Wiley, 2002.

[67] R. E. Prange. Quantized hall resistance and the measurement of the fine-structure constant. *Phys. Rev. B*, 23:4802–4805, May 1981.

[68] R. E. Prange and R. Joynt. Conduction in a strong field in two dimensions: The quantum hall effect. *Phys. Rev. B*, 25:2943–2946, Feb 1982.

[69] R. Rodriguez, F. Parmentier, and D. e. a. Ferraro. Relaxation and revival of quasiparticles injected in an interacting quantum hall liquid. *Nat Commun*, 2020.

[70] C. Rolland. *Strong coupling quantum electrodynamics of a voltage biased Joseph- son junction*. PhD thesis, Universite Lille, 2016.

[71] C. Rolland, A. Peugeot, S. Dambach, M. Westig, B. Kubala, Y. Mukharsky, C. Altimiras, H. le Sueur, P. Joyez, D. Vion, P. Roche, D. Esteve, J. Ankerhold, and F. Portier. Antibunched photons emitted by a dc-biased josephson junction. *Phys. Rev. Lett.*, 122:186804, May 2019.

[72] P. Roulleau, F. Portier, P. Roche, A. Cavanna, G. Faini, U. Gennser, and D. Mailly. Direct measurement of the coherence length of edge states in the integer quantum hall regime. *Phys. Rev. Lett.*, 100:126802, Mar 2008.

[73] P. Roulleau, F. Portier, P. Roche, A. Cavanna, G. Faini, U. Gennser, and D. Mailly. Noise dephasing in edge states of the integer quantum hall regime. *Phys. Rev. Lett.*, 101:186803, Oct 2008.

[74] L. Saminadayar, D. C. Glattli, Y. Jin, and B. Etienne. Observation of the $e/3$ fractionally charged laughlin quasiparticle. *Phys. Rev. Lett.*, 79:2526–2529, Sep 1997.

[75] W. Schottky. *Ann. Phys. (Leipzig) 57, 541 (1918).*

[76] C. Schönenberger, S. Oberholzer, E. V. Sukhorukov, and H. Grabert. Shot noise in schottky's vacuum tube, 2001.

[77] B. J. van Wees, H. van Houten, C. W. J. Beenakker, J. G. Williamson, L. P. Kouwenhoven, D. van der Marel, and C. T. Foxon. Quantized conductance of point contacts in a two-dimensional electron gas. *Phys. Rev. Lett.*, 60:848–850, Feb 1988.

[78] V. Volkov and S. Mikhailov. Edge magnetoplasmons: low-frequency weakly damped excitations in inhomogeneous twodimensional electron systems. *Sov. Phys.-JETP 67, 1639-1653*, 1988.

[79] M. B. Ya.M. Blanter. Shot noise in mesoscopic conductors. *Physics Reports*, 336:1–166, 2000.

[80] A. L. Yeyati, A. Martin-Rodero, D. Esteve, and C. Urbina. Direct link between coulomb blockade and shot noise in a quantum-coherent structure. *Phys. Rev. Lett.*, 87:046802, Jul 2001.

[81] D. Yoshioka. *The Quantum Hall Effect.* Springer, 2002.

[82] B. Yurke and J. S. Denker. Quantum network theory. *Phys. Rev. A*, 29:1419–1437, Mar 1984.

[83] E. Zakka-Bajjani, J. Segala, F. Portier, P. Roche, D. C. Glattli, A. Cavanna, and Y. Jin. Experimental test of the high-frequency quantum shot noise theory in a quantum point contact. *Phys. Rev. Lett.*, 99:236803, Dec 2007.

[84] N. B. Zhitenev, R. J. Haug, K. v. Klitzing, and K. Eberl. Experimental determination of the dispersion of edge magnetoplasmons confined in edge channels. *Phys. Rev. B*, 49:7809–7812, Mar 1994.